Uranium Hexafluoride Assay Measurement Using Femtosecond Laser-Induced Breakdown Spectroscopy

A Dissertation Presented for the
Doctor of Philosophy
Degree
The University of Tennessee, Knoxville

Benjamin S Jordan
May 2022

Copyright © 2022 by Benjamin Samuel Jordan.
All rights reserved.

ACKNOWLEDGEMENTS

I first wish to thank those who serve on my committee for contributing their time, energy, expertise, and funding toward this project: Dr. Howard Hall (Chairman), Dr. Jason Hayward, Dr. Matthew Cook, Dr. Jeff Cooper, and Dr. Jason Readle. I am very grateful to Dr. Hall and Dr. Hayward for the equipment and research facilities they made available to me through their involvement with the Nuclear Science and Security Consortium. Dr. Cook deserves thanks and recognition for his tireless assistance obtaining permission to bring UF_6 to the University of Tennessee and marshalling the resources necessary to commission the fs-LIBS equipment. Dr. Cooper and Dr. Readle also deserve special thanks for the specialized instruction and wisdom they shared with me throughout this process.

In addition, my sincere gratitude and appreciation are owed to Larry Cutlip, Mike Whitehurst, and Centrus Energy for allowing and supporting this continuing education endeavor. This research would not have been possible without their support of me or access to the resources that Centrus made available to build, leak check, and fluorinate the sample chambers key to this research. Thank you to my network of friends and co-workers who offered numerous insights and wisdom that have enhanced this product. My heartfelt appreciation goes to Garry Clark who assisted me greatly by specifying and assembling the purpose-built MATLAB work station that executed essentially all of the data analysis for this research. Mat Stanke's knowledge and credentials in assuring the leak tightness of the sample chambers I constructed was vital to the success of this research. Steve Poirier's experience and knowledge of nuclear systems was vital to safely and effectively conducting the passivation of the sample chambers to ready them for containing the UF_6 sample material.

Special thanks are owed to both Dr. Leigh Martin and Dr. Glenn Fugate of Oak Ridge National Laboratory for their assistance in sourcing the UF_6 sample material used in this research. Acknowledgement of my peers from Dr. Hall's research group is also warranted. Daniel Hartman and Dean Forrest both generously contributed their time to satisfy the two-man-rule requirements associated with UF_6 handling at the University of Tennessee. Daniel Hartman is also to be credited with the high resolution tightly zoomed photography included in this dissertation. Dean Forrest contributed extensive MATLAB knowledge and computing resources which helped me characterize the performance of the spectrometer and ICCD prior to delivery of the UF_6 samples.

Special thanks to my combined tutors, editors, critics, and cheerleaders: Dr. Sam Jordan, Dr. Michael Thomason, and Dr. Sara Jordan. Last, and far from least, thank you to Dr. Jennifer Jordan, Henry Jordan, and Scout Jordan for encouraging me, carrying the loads that I dropped during this process, and putting up with me as I focused on completing this research.

ABSTRACT

Most modern uranium enrichers use centrifuges to separate ^{235}U [Uranium 235] and ^{238}U [Uranium 238] in the gaseous form, UF_6 [uranium hexafluoride]. Monitoring the enrichment level of the material being produced in a Gaseous Centrifuge Enrichment Plant (GCEP) or in a single centrifuge is important to the enricher as well as those tasked with monitoring the enrichment activities of declared facilities, such as the International Atomic Energy Agency (IAEA). Many enrichers currently select mass spectrometry as the only alternative that can reliably provide the accuracy necessary for optimizing the performance of their centrifuges during research and development or certifying the resulting products of their commercial enrichment plants to their customers. Unfortunately, this method is costly in terms of personnel requirements, equipment investment, and difficulty obtaining a continuous measurement of the enrichment. Continuously conducting measurements of UF_6 enrichment in a foreign facility essentially precludes mass spectrometry due to the costs noted above and the strong desire of the foreign enricher not to be subjected to destructive sampling of their enriched material. The commercial enrichment industry has been able to work around the shortcomings of the measurement techniques currently available. However, nuclear security interests have been sufficiently underserved that significant research and development is being invested to provide cheaper, more accurate, robust systems which can be installed in declared enrichment facilities to provide a continuous monitor of the enrichment activities conducted within those facilities.

The research developed methods for determining UF_6 assay using a femtosecond laser-induced plasma. The resulting methods yielded assay measurements within 0.28% of the actual ^{235}U content with a standard deviation of 0.90%. The research also includes results of investigation of High Order Generalized Singular Value Decomposition (HOGSVD) as a means of analyzing spectral data for assay measurement. HOGSVD achieved 95.15% accuracy in spectral classification testing. Additionally, *ARESLab* models were built using the spectral data collected during this research and *ARESLab* models built with HOGSVD-based numerical features. The HOGSVD-based model's ability to predict assay is compared with the spectra-based model. HOGSVD was also demonstrated to be of value identifying additional isotopic shifts for inclusion in multivariate fitting algorithms for determining UF_6 assay. The contribution of this research is an accounting of the effectiveness and applicability of the femtosecond laser and HOGSVD to the measurement of UF_6 assay through Laser-Induced Plasma Emission Spectroscopy.

TABLE OF CONTENTS

Chapter One Introduction and Background Information 1
Introduction 1
Background 1
Existing Methods of Measuring UF_6 Assay 2
Mass Spectrometry 3
COMbined Procedure for Uranium Concentration and Enrichment Assay 3
Techniques for Monitoring GCEP Process Piping 4
Rationale for this Research 6
Motivation 6
Differentiators 7
Chapter Two Literature Survey 8
Scope of the Survey 8
Methodological Approach to the Survey 8
Laser-Induced Emission-Based Assay Measurement 8
Processes Similarities 9
Inclusion of Solid Ablation 9
Themes 10
Isotopic Shifts 10
Mass Shift 11
Field Shift 11
Hyperfine Structure 12
LIBS Applicability for Uranium Isotopic Analysis 12
Ablation of Solids 14
Nanosecond LIBS 14
Femtosecond LIBS 17
Gaseous Femtosecond LIBS 19
Parameters that Impact Laser-Based Spectroscopy 20
Emission Spectrum and Line Selection 20
Line Accuracy and Isotopic Shifts 21
Effects of Pressure and Vacuum 22
Extracting Isotopic Information from Spectra 22
Principal Component Analysis and Partial Least Squares Regression 23
Singular Value Decomposition 23
Generalized Singular Value Decomposition 25
Higher Order Generalized Singular Value Decomposition 26
Advanced SVD of LIBS Spectra 27
Dynamic Time Warp 27
Current Approaches and How this Research Fits 28
Technical Challenges 28
Micro-Destructive Sampling Ramifications 29
Methods in Development (Emission only) 30
Chapter Three Materials and Methods 32

fs-LIBS System....32
Laser....32
Spectrometer....32
Intensified Charge Coupled Devices....36
Software....37
System Performance....38
UF_6 Sample Material....38
Uranium Hexafluoride Sample Chambers....38
Spectral Line Database Generation....44
Candidate Spectral Window....45
Overview of Experimental Procedure....45
Laser, ICCD, and Plasma Emission Timing Coordination....48
Parameters Investigated....49
Laser power and energy density....49
Delay and Gate Width Research Method....51
Exposure....53
Partial pressure of gas being analyzed....56
Precision calibration of collected spectra for assay measurement....56
Description of the Fitting Algorithm Used for Establishing Baseline of fs-LIBS with MVNLSF....58
Fitting window data range (*dr*)....59
Chapter Four Results....62
Spectral Fitting Figures....62
Testing Configurations....64
Optimization of Collection Parameters....67
Gate Delay and Gate Width....67
Low-Power Low-Pressure (LPLP) Surveys....67
High Power Low Pressure (HPLP) Surveys....72
High-Power High-Pressure (HPHP) Survey....75
LPLP Investigations....78
HPLP Investigation....81
HPHP Investigation....84
Steps Taken to Enhance Spectral Information....87
Signal to Noise Ratio Enhancement....87
Confirmation of ICCD Detector Offset Approach....89
Effect of Averaging Spectra as Opposed to Averaging R values....91
Fitting Entire Wavelength Window Instead of *dr* Approach....93
Comparing Survey, Investigation, and Kinetic Series Results....95
Plasma Emission Valuation....99
Potential Cause of Plasma Emission Valuation Difference by Assay....102
Precipitate Buildup in 38.103% Sample Chamber....103
HOGSVD and DTW....109
HOGSVD for Initial Assessment of Assay....109
Explanation of the HOGSVD-DTW Dataset....116

Assay Classification through Pattern Recognition with HOGSVD and DTW 118
Numerical Features of Spectra Based on HOGSVD and DTW 120
Applying HOGSVD-DTW Numerical Values in Estimating Assay for Unknown Samples 124
HOGSVD for Identification of Candidate Isotopic Pairs 126
Additional Isotopic Pairs for fs-LIBS 130
Reexamination of Spectra with Emphasis on SD 134
Potential Contributors to SD Results 138
Chapter Five Conclusions 147
Application of fs-LIBS to UF_6 Assay Measurement 147
Optimum Laser Power and UF_6 Sample Pressure 147
Impact of Precipitate Buildup 148
Additional Assay Measurement Contributions 149
Advanced Numerical Analysis Techniques Demonstrated 149
Future Work 150
fs-LIBS Conclusion 152
List of References 153
Vita 165

LIST OF TABLES

Table 2.1. 12 Isotopic Shifts (IS) Identified by Song et al. [51] 24
Table 3.1. UF_6 Samples Provided by ORNL 39
Table 3.2. Delays and Gate Width Settings Used for Survey Data Collection 52
Table 3.3. Delays and Gate Width Settings Used for Investigation Data Collection 54
Table 3.4. Delays and Gate Widths Settings Used for Kinetic Series Data Collection 55
Table 4.1. Laser Power at the Focusing Lens in Watts for the Sampling Conditions 65
Table 4.2. Average Pressure in Torr for the Sampling Conditions 66
Table 4.3. Distance Between Isotopic Pairs and the Next Higher Isotopic Pair and *dr* Needed to Span Distance to the Next Higher Isotopic Pair 68
Table 4.4. LPLP Survey Results 71
Table 4.5. HPLP Survey Results 74
Table 4.6. HPHP Survey Results 77
Table 4.7. LPLP Investigation Results 80
Table 4.8. HPLP Investigation Results 83
Table 4.9. HPHP Investigation Results 86
Table 4.10. Improved SNR Results 90
Table 4.11. Comparison of Performance Statistics in Survey Configurations 96
Table 4.12. Comparison of Performance Statistics in Investigation Configurations 97
Table 4.13. Performance Statistics for Improved SNR Kinetic Series 98
Table 4.14. 38.103% Sample Results 111
Table 4.15. HOGSVD-DTW Classification Experiment Results 123
Table 4.16. HPHP Survey data with delay and gate width based on (SD) 135
Table 4.17. HPHP Survey Summary Results for (SD), (Combo), and the original HPHP 136
Table 4.18. HPHP Survey data with delay and gate width based on (Combo) Factor 137
Table 4.19. HPHP Investigation Summary Results for (SD), (Combo), and the original HPHP Investigation results 139
Table 4.20. HPHP Investigation data with delay and gate width based on (SD) 140
Table 4.21. HPHP Investigation data with delay and gate width based on (Combo) Factor 141
Table 4.22. HPHP Kinetic Series Improved SNR data with delay and gate width based on (SD) 142
Table 4.23. HPHP Kinetic Series Improved SNR Summary Results for (SD), (Combo), and the original HPHP Kinetic Series Improved SNR results 143

Table 4.24. HPHP Kinetic Series Improved SNR data with delay and gate width based on (Combo) factor 144

LIST OF FIGURES

Figure 1.1. Depiction of OLEM with CEMO shown for reference [21]. 5
Figure 2.1. Russo et al. concept diagram representing direct ejection of particles. The particle sizes and size distribution are related to the heated volume. The paper notes variability of particle size associated with the nanosecond pulse [72].....15
Figure 2.2. Graph by Russo et al. shows relative decay rates of measured optical emission from two plasmas initiated with lasers having all properties equal except the pulse duration [72].....16
Figure 2.3. Plasma formation and ablation timeline by femtosecond laser illustration by Labutin et al. [76]. 18
Figure 3.1. Solstice Ace femtosecond laser with steering mirror and power meter visible in the foreground.....33
Figure 3.2. Plasma size observed in UF_6 gas resulting from ~2.5 W femtosecond laser. For scale, the plasma diameter is between 2 and 3 mm. 34
Figure 3.3. Plasma in UF_6 gas resulting from ~6 W femtosecond laser. For scale the plasma is approximately 5 mm long and 2 mm in height. 35
Figure 3.4. Fluorination of Sample Chambers 41
Figure 3.5. Crystalline UF_6.....43
Figure 3.6. fs-LIBS Testing arrangement.....46
Figure 3.7. fs-LIBS High Power Equipment Configuration 50
Figure 3.8. Fitting window *dr* Pair 1 and Pair 8 60
Figure 4.1. fs-LIBS spectra from five UF_6 samples collected with a delay of 848 ns and gate width of 938 ns in a sampling configuration with high-pressures of approximately 60 Torr and laser power of about 6 Watts creating the plasma. 63
Figure 4.2. LPLP Survey Fits 69
Figure 4.3. HPLP Survey Fits 73
Figure 4.4. HPHP Survey Fits.....76
Figure 4.5. LPLP Investigation Fits 79
Figure 4.6. HPLP Investigation Fits.....82
Figure 4.7. HPHP Investigation Fits.....85
Figure 4.8. Improved SNR MVLSF fits.....88
Figure 4.9. Graph comparing subtraction of a single detector offset value from each pixel versus an offset based on the pixel-by-pixel subtraction of the offsets obtained from multiple dark images. 92
Figure 4.10. Graph comparing the "*dr*" Fitting Window approach with the approach of treating the entire spectral window (e.g., 424.3 nm to 424.5 nm) as the area over which fitting error will be minimized.....94
Figure 4.11. Plasma Emission Valuation Timelines showing each nanosecond of plasma life from 0 to 3566 ns based on that nanosecond's inclusion in a

delay and gate width combination that yielded a “good” MVNLSF-12-based assay prediction. 100
Figure 4.12. Plasma Emission Valuation Timelines of each testing configuration showing each nanosecond of plasma life from 0 to 3566 ns based on that nanosecond’s inclusion in a delay and gate width combination that yielded “good” MVNLSF-12-based assay predictions. 104
Figure 4.13. Precipitate formation on 38.103% Sample Chamber 105
Figure 4.14. Progressive data captures while precipitate forms in 38.103% sample chamber. 106
Figure 4.15. Precipitate deposition on sample chambers other than 38.103% . 108
Figure 4.16. Spectral Fits for 38.103% Sample 110
Figure 4.17. Plots of 1/Λ for 317 eigenvalues of *S* between 2 spectra and plots of the right-most 15 eigenvalues of *S* ($1/\Lambda_{(right)}$) to provide an indication of assay relative to the 0.287% reference spectrum. 113
Figure 4.18. Illustration of Bootstrap Sample creation 117
Figure 4.19. Diagram of the Assay Classification Experiment using HOGSVD-DTW features about unknown-assay spectra to make a determination about the assay most closely matching in the training data. 119
Figure 4.20. Confusion Matrices for MATLAB *ClassificationLearner* algorithm classifying HOGSVD-DTW features about unknown spectra to the assay class they most closely match. 121
Figure 4.21. Assay estimations using an ARES model which includes training data for all the assays tested. 125
Figure 4.22. Results of ARES models estimating assays based on training data that does not include the full range of assays in the test data. 127
Figure 4.23. Importance-of-Wavelengths in differentiating spectra of different assay 129
Figure 4.24. Improved SNR Kinetic Series Fits using Additional Isotopic Shifts 131
Figure 4.25. Graph comparing the error magnitude for assay measurement using the original 12-pair MVNLSF algorithm and the 14-pair MVNLSF (MVNLSF-14) measurement approach, which adds the 2 isotopic pairs identified as having benefit for fs-LIBS measurement in this research. The error magnitude data is charted as the square root of the sum of the squared errors for each sample assay measured in each testing configuration. 133
Figure 4.26. Sinusoidally Varying Plasma Emission Intensity at ~ 2 Hz 145

Chapter One

Introduction and Background Information

Introduction

This research adds to the state-of-the-art for laser-based plasma emission technologies which provide for assay measurement of UF_6 gas, the output of a gaseous centrifuge enrichment plant (GCEP). It follows a multi-pronged approach to further development toward a continuous laser-induced plasma emission-based assay measurement system through the following original contributions:

- Exploration of potential advances in accuracy through femtosecond Laser-Induced Breakdown Spectroscopy (fs-LIBS) isotopic analysis of UF_6 gas
- Demonstration of application-specific techniques and procedures to apply femtosecond LIBS to UF_6 gas
- Application of previously undemonstrated spectral evaluation techniques to provide enhanced guidance to users of LIBS-based systems for UF_6 gas isotopic measurement

The following sections describe why this research is of value to nuclear security professionals and to nuclear material enrichers. Absorption-based and emission-based assay measurement techniques have both been demonstrated, but emission-based techniques leverage the characteristics of the femtosecond laser more effectively than absorption-based techniques where the femtosecond laser's speed may add unnecessary complexity [1, 2]. Additionally, emission-based LIBS techniques appear closer to deployment [3]. This fact increases the near-term benefit that could be provided through additional understanding of techniques, accuracy improvements from femtosecond lasers, and enhanced analysis associated with emission-based techniques. Therefore, this research focuses on emission-based techniques and potential enhancements therein.

Background

The majority of uranium enrichers conduct their enrichment processes using gaseous UF_6. The enrichment of the ^{235}U isotope is an important step in the production of nuclear fuel for most of the nuclear power plant designs currently deployed. Nuclear enrichers are currently reliant on Mass Spectrometry (MS) to obtain the accuracy that they need for optimizing new designs of enrichment equipment [3-6]. During commercial operation, enrichers must rely on the accuracy of MS to certify that their products conform to specifications of their customers [4-6]. Uranium enrichers currently lack a good option for providing

continuous monitoring of the enrichment levels they are producing and must rely on process knowledge to assure a high-quality product prior to the point of measurement with a mass spectrometer [7, 8]. This research does not address the issues likely to arise as a fs-LIBS assay measurement system is modified for on-line measurements, but rather will focus on the underlying measurements that must be mastered before modifications for on-line use should be considered.

The same enrichment equipment that processes gaseous UF_6 for the nuclear power industry can be used to continue the enrichment process to ^{235}U percentages that are relevant for nuclear weapons. This fact makes monitoring of nuclear facilities very important. The International Atomic Energy Agency (IAEA) is tasked with monitoring enriched uranium production at declared facilities. The IAEA lays out the following objectives surrounding this monitoring function:

1. "Objective 1: The timely detection of the diversion of significant quantities of natural, depleted or low enriched UF_6 from the declared flow through the plant, and the deterrence of such diversion by the risk of early detection" [7, 9].
2. "Objective 2: The timely detection of the misuse of the facility in order to produce undeclared product (at the normal product enrichment levels) from undeclared feed and the deterrence of such misuse by the risk of early detection" [7, 9].
3. "Objective 3: The timely detection of the misuse of the facility to produce UF_6 at enrichments higher than the declared maximum, in particular highly enriched uranium, and the deterrence of such misuse by the risk of early detection" [7, 9].

The IAEA is currently forced to collect 1-10 g of gaseous UF_6 and transfer that sample through a rigorously managed chain of custody to a central laboratory for analysis by MS [3, 10]. This process leaves large gaps in coverage when the facility could operate outside its agreed-to limits without detection.

Existing Methods of Measuring UF_6 Assay

There are several methods currently available for taking assay measurements in the field and laboratory. Each has pros and cons, but none has provided the combination of continuous measurement, accuracy, and low cost that current researchers are seeking to achieve. Some of the prevalent current methods for assay measurement are discussed in this section. The methods discussed are not limited to laser-based techniques, but are simply the most prevalent methods currently used in support of commercial nuclear activities and nuclear safeguards.

Mass Spectrometry

The current standard in both the commercial enrichment and nuclear security fields for isotopic analysis is the mass spectrometer [11-16]. The mass spectrometer offers the accuracy necessary for commercial enrichers to demonstrate that they have satisfied their customer's specifications. Many of the academic publications dealing with isotopic analysis compare proposed techniques against the mass spectrometer [3, 11, 12].

Mass Spectrometry is not limited to solid uranium forms. Gaseous samples of UF_6 are directly measurable using a gas source mass spectrometry. Gas source mass spectrometry systems produce relative uncertainties measuring the ^{235}U:^{238}U ratio as low as 0.03% [11]. These systems are expensive, not usually portable, and require expert operation [12, 17]. Continued development of LIBS-based techniques, such as fs-LIBS, has the potential to address these shortcomings [3].

COMbined Procedure for Uranium Concentration and Enrichment Assay

Another method for measuring enrichment of solid forms of uranium in the field is the COMbined Procedure for Uranium Concentration and Enrichment Assay (COMPUCEA). COMPUCEA combines two measurement strategies. First, COMPUCEA incorporates energy-dispersive X-ray absorption edge spectrometry, which involves a source of X-ray excitation to create an electromagnetic emission spectrum unique to the interrogated element, in order to measure uranium elemental content [10]. Second, COMPUCEA uses gamma ray spectrometry to measure uranium enrichment [10]. COMPUCEA incorporates two $LaBr_3$(Ce) detectors for increased throughput [18]. Gamma-ray spectroscopy systems are a very helpful tool for many safeguard applications [19]. They provide accurate and sensitive determination of the ^{235}U enrichment, but they require up to an hour to realize a measurement of an oxide sample with low ^{235}U content [19]. COMPUCEA also requires a labor-intensive sample preparation process performed by a chemist [3].

COMPUCEA offers typical combined measurement uncertainty of 0.25% relative, meaning the uncertainty in the measurement is 0.25% in comparison to the quantity of ^{235}U itself [10, 18]. COMPUCEA has been used for physical inventory verification since 2007 and in 2011 the IAEA authorized COMPUCEA for certain on-site measurements [18].

Techniques for Monitoring GCEP Process Piping

On-Line Enrichment Monitor (OLEM)

The On-Line Enrichment Monitor (OLEM) was designed to specifically detect diversion, excess production, and production of higher than agreed assays at GCEPs [20]. The OLEM uses a collimated sodium iodide activated with thallium NaI(Tl) spectrometer as its primary measurement instrument [20]. In 2011, prior to the construction of the OLEM, it was envisioned to have target uncertainties as a high as 3% for the product [20]. Reports of OLEM performance have included feedback that the system is difficult to calibrate and maintain, is easily bypassed, and cannot detect whether the gas is flowing within the process piping that it is monitoring [7]. Fig. 1.1 shows the general layout of the OLEM system [21].

Cascade Header Enrichment Monitor (CHEM)

The Cascade Header Enrichment Monitor (CHEM) was designed to use the 187.5 keV gamma-ray photopeak to assess the amount of ^{235}U in the process piping of a gaseous centrifuge plant [22]. The CHEM uses X-ray fluorescence 98.4 keV x-ray from uranium with a ^{57}Co X-ray fluorescence source to determine the total amount of uranium present in the process piping [22]. Once the ^{235}U and total uranium present are known, the enrichment can be calculated.

Continuous Enrichment MOnitor (CEMO)

The Continuous Enrichment MOnitor (CEMO) was researched by the United Kingdom Atomic Energy Authority and URENCO [7]. The CEMO uses a Thallium-doped Sodium Iodide (NaI(Tl)) scintillator and a ^{109}Cd transmission source to measure enrichment in process piping where the pressure is less than 10 Torr [7]. The greatest differentiator for CEMO was that it was not invasive to the process piping it was monitoring [7]. The location of CEMO relative to the OLEM system is also shown in Fig. 1.1. Note that the CEMO location is in close proximity to, and perhaps within, the cascade itself. This location would likely not be permitted by enrichers because of their need to protect proprietary and potentially classified information about how their cascades operate.

Current Status of Enrichment Monitors

CHEM and CEMO are no longer used and had significant limitations during operation which include: limited diameter piping applicability, pipe thickness, and pressure windows of operation, reliance on short-lived sources requiring regular replacement, and an inability to detect whether the process gas being monitored is flowing or stagnant [7]. OLEM is still in use but, as previously mentioned, also suffers from challenges similar to those that plagued CHEM and CEMO.

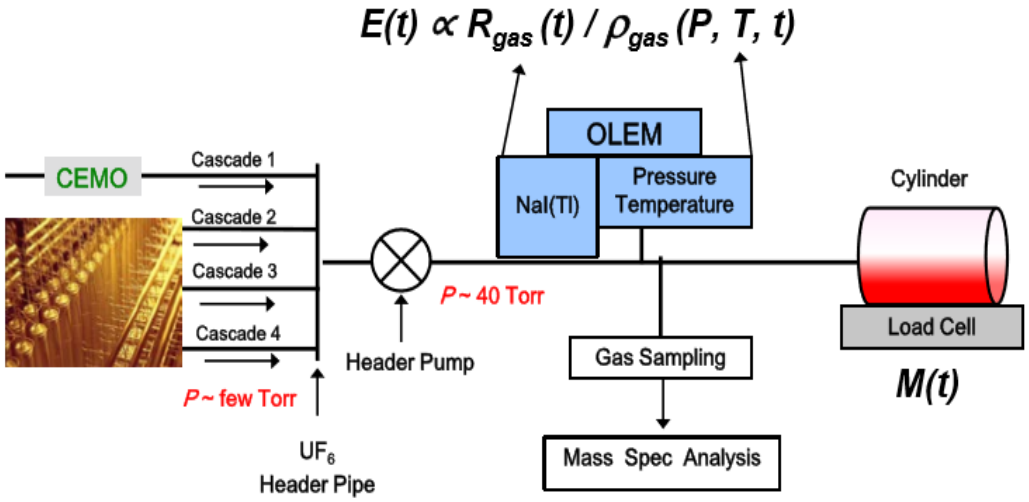


Figure 1.1. Depiction of OLEM with CEMO shown for reference [21].

Rationale for this Research

Motivation

This background indicates that a gap still exists between current technology and the need that the nuclear security community and the commercial enrichment firms have for assay measurement that is continuous, accurate, and affordable. The current solutions offered to these industries fall short in one or more of the characteristics and either drive up cost or, in some cases, force operations to proceed with incomplete data. This research involves applying a femtosecond laser and high precision spectroscopic equipment to an underserved, but well published and publicized, problem set. In the recent past the publications have centered around low-cost man-portable systems that inspectors can move and connect to various systems and locations versus this research which will focus on accuracy and precision rather than portability [23-25].

The goal of this research is further development of the tools that enable the underlying measurement technology needed for operators of gaseous centrifuge enrichment plants or those charged with the monitoring of GCEPs to execute continuous, accurate isotopic measurements of the UF_6 flowing through process piping of these facilities. Again, for clarity, this research does not seek to addresses the challenges of making on-line measurements of UF_6 gas flowing through a piece of piping, as would be expected at an operating enrichment facility.

There is complementary research underway within Lawrence Berkeley National Laboratory (LBNL) and Oak Ridge National Laboratory (ORNL) [23, 24, 26, 27]. This research performed at The University of Tennessee – Knoxville (UTK) is an extension of the research already underway. The opportunity for extension of the national laboratory research stems from the fact that UTK has a femtosecond laser (benefits of femtosecond lasers will be discussed in Chapter 2) whereas the type of laser employed by the laboratories is a nanosecond unit due to a different objective that the laboratories have. The laboratories are developing a system which is intended to be a man-portable and field-deployable system capable of making measurements that are useful for an inspector operating in a foreign GCEP.

The purpose of this research effort is to explore the enhanced precision of the femtosecond laser (e.g., greater energy deposition over a smaller volume) to provide accuracy that approaches that of a mass spectrometry system. This level of accuracy is necessary for operators of GCEPs to optimize the production of their machines and meet the American Society for Testing Materials specifications for their product [5] . Additionally, the ability to conduct these higher accuracy measurements continuously could become useful when

declared foreign GCEPs agree to continuous monitoring. A continuously operating femtosecond laser-based assay measurement system could operate unattended for long periods of time in a foreign GCEP, thus permitting greater insight into the operation of those facilities than has been possible in the past.

Differentiators

The first differentiator for this research is that it provides the benefits mentioned above to the underlying measurement technology necessary for both the on-line enrichment monitoring and mass spectrometry users by determining a method for applying a suite of equipment that has not been brought to bear on this problem in the past. Another significant differentiator is that the goal is to achieve precision as near to a mass spectrometer as possible while preserving the possibility of continued development toward a continuous monitoring capability of an OLEM-type system. Another contribution to the current laser-induced plasma emission-based spectrometry body of knowledge is that this work includes process development and some optimization of the most effective approach to making these measurements of UF_6 using a femtosecond laser. Finally, the resulting spectral data is analyzed using tools and techniques that have not been applied to this problem set with its particular technical, political, and safety/security complications.

Chapter Two

Literature Survey

Scope of the Survey

This literature survey considers laser-induced emission-based assay measurement. There is a suite of absorption-based techniques which utilize lasers to make measurements about materials based on which portion of the laser pulse is absorbed by the material of interest. One significant challenge that absorption techniques must overcome is the need for simultaneous measurement of the ^{235}U and ^{238}U absorption [3]. This simultaneous measurement is needed for accuracy because the inherent noise in isotope measurement systems is largely correlated noise due to the flickering of the laser power source, variations in the sample introduction system, fluctuations in atomization, and interference noise from power supplies [3]. Correlated noise can be addressed for absorption-based systems through the use of multiple lasers arranged to interrogate the same physical area of a sample, but this complexity is not needed for an optical emission technique such as fs-LIBS where the single laser energy source excites both ^{235}U and ^{238}U simultaneously [3]. Therefore, these absorption techniques are out of the scope of this review for the reasons mentioned and because, as Chan et al. indicate in their scoping study, the atomic optical emission spectrometric techniques have a higher probability of reaching the International Target Values (ITVs) deemed by the IAEA to be achievable analytical accuracy and precision levels [3, 28]. Therefore, this review addresses techniques where laser pulses are used to create an emission and that emission is then analyzed to make determinations about the material being measured.

Methodological Approach to the Survey

Laser-Induced Emission-Based Assay Measurement

The most basic description of laser-induced plasma emission-based assay measurement is that a laser pulse is created and then focused to form a plasma. The plasma will exceed the threshold of energy necessary to break down the material being interrogated and leave many of the atoms, at least momentarily, in an excited state. It is well understood that elements emit light of characteristic frequencies as they return to a lower energy state [29-33]. The characteristic light is collected and evaluated to determine which characteristic frequencies are present, thereby allowing an assessment of which elements are present [34, 35]. This technique can be used to determine not only which elements are present, but can also be used to determine which isotopes of the elements are present, and even make assessments about the relative abundance of those isotopes [31, 32, 36-44].

Processes Similarities

There are several names and acronyms used to refer to various techniques which follow the basic process described above. Examples include:

- LIBS – Laser Induced Breakdown Spectroscopy [45-49]
- LIAES – Laser Induced Atomic Emission Spectroscopy [50, 51]
- LIPS – Laser Induced Plasma Spectroscopy [52-54]
- LAMIS–Laser Ablation Molecular Isotopic Spectrometry [55-61]

These processes are similar and often involve the same or similar equipment. The general term LIBS will be used for the purposes of this review. Other terms will only be used to draw a distinction between a specific laser-induced emission-based process and the others to clarify a particular technical topic.

Inclusion of Solid Ablation

Measurements of UF_6 are typically executed on samples that are in a gaseous state. However, LIBS of solids and of the ablation processes will be discussed to provide additional insight to the processes that occur within the gaseous samples. There are many considerations regarding the temporal nature of the plasma and the differences between the plasma produced by nanosecond versus femtosecond lasers[54, 62, 63]. These differences are important to include to help guide better understanding of the physics involved in the femtosecond versus nanosecond gaseous LIBS measurements. Additionally, as will be discussed in detail throughout this chapter, the solid LIBS literature helps to explain why femtosecond LIBS appeared to offer potential accuracy enhancements worthy of exploration in this dissertation and research [62, 64].

It should be noted that, although there are significant differences in the physical process of creating a plasma through ablation of a solid and the formation of a plasma in a gas, the initial hope at the outset of this research was that the plasma emissions of solid uranium would be similar to the plasma emission from UF_6 gas. However, Chan et. al conclude that emissions that showed significant promise in the 424.3 to 424.5 nm range for solids ultimately suffered from too much self-absorption to yield accurate assay measurement of gaseous UF_6 gas [27]. Self-absorption is typically observed for emission lines where the lower level of the transition is the ground state or close to the ground state [33]. These emission lines are called resonance lines and because the emission must pass through the cooler outer layer of the plasma, likely populated by many atoms in their ground state, they have a high probability of being absorbed [33]. The absorption can be extensive enough to produce reduced intensity deformations in the spectral peak referred to as self-reversal [33]. Therefore, the LISA-UE research group elected to refocus their effort on a spectral window with no

resonance lines [27]. Nonetheless, this research continues to focus on the 424.3 to 424.5 nm range for UF_6 gas plasma emission, to give insight to whether the self-absorption is as severe when using a femtosecond laser to create the plasma.

Themes

The topics covered in this review of relevant work are intended to cover the following themes:

- Impact on the practitioner attempting to gain knowledge and determine the appropriateness of a LIBS approach to conducting increased precision isotopic analysis of materials relevant to commercial enrichers and nuclear security professionals.
- Selection of emission lines and system configuration choices that the commercial enricher and the nuclear security professional must evaluate and select to enhance the usefulness of laser-induced emission-based assay measurement technology in their applications.
- Providing the enricher or nuclear security practitioner an understanding of the light gathering and detecting technologies to be considered.
- Employing various techniques which assist with extracting useful information from the spectral data provided by the LIBS-type system. Included in this section is a brief explanation of Higher Order Generalized Singular Value Decomposition (HOGSVD) which is a means to potentially extract structured numerical information embedded in the data from these systems.
- Developing the underlying measurement technology needed for organizations tasked with monitoring the enrichment activities of declared foreign enrichment facilities, and also highlighting an additional need for research which can potentially benefit enrichers as well.

Isotopic Shifts

The key capability required for assay measurement is to determine the relative abundance of the isotopes of interest in the measurement. Every element produces a characteristic spectral emission as it de-excites from an excited state. Additionally, the energy of the spectral lines emitted does depend slightly on the isotope [44]. This dependence is the result of the slightly different charge distribution within the nucleus and resulting differences in the way the nucleus interacts with the electrons [44]. LIBS processes rely on the presence of this isotopic shift in the spectral line energy emitted by one isotope relative to another. The first isotope shift to be measured with the assistance of a laser was completed in 1966 for stainless steel using a Q-switch ruby laser [65]. Subsequent enhancements in lasers, computers, spectrometers, and other

ancillary equipment have improved the accuracy and broadened the applicability of this technique.

The first study that raised the LIBS technique as a viable means of measuring uranium isotopics was published by Pietsch in 1998 [66, 67]. The specifics of the technique for measuring the relative abundance of isotopes will be discussed later, but first additional detail on isotopic shifts is needed. There are two primary contributions to the isotopic shift (IS): the field shift (FS) and the mass shift (MS). Their contributions to the isotopic shift are shown in the relation: $IS = MS + FS$.

Mass Shift

The mass shift establishes that each atomic level is described by the angular momentum and the energy for a given atom [44]. The different number of neutrons in the nucleus that exists between two different isotopes of the same element obviously results in a difference in the mass of the atomic nucleus between the two isotopes. King reports that, since the angular momentum of a level has a definite fixed value, only the energy of the level can be changed so that the angular momentum can remain the same for the level [44]. This change in energy is referred to as the mass shift and is a contributor to the overall isotopic shift in uranium [68]. The mass shift is also called the reduced mass effect [44]. In classical mechanics, a one-electron atom or ion can be treated as a single particle with a reduced mass $mM/(M+m)$ interacting with an infinitely massive particle at rest, where m is the mass of an electron and M is the mass of a point nucleus [44]. For a classical orbit of a given shape and momentum, the binding energy $T_{(M)}$ depends on the nuclear mass according to the relationship $T_{(M)} \propto \frac{M}{M+m}$ [44]. The experimentally observed shifts between a heavy (H) and light (L) isotope can be approximated in a spectrum using the following relationships: $\frac{\nu_H - \nu_L}{\nu_H} = \frac{m(M_H - M_L)}{M_H(M_L+m)}$, $\frac{\nu_H - \nu_L}{\nu_L} = \frac{m(M_H - M_L)}{M_L(M_H+m)}$ where ν is the frequency [44]. The calculation of shifts for complex atoms continues to be an area of research to improve accuracy and completeness of the theoretical models [68].

Field Shift

In addition to the easily conceptualized mass shift there is also a field shift that contributes significantly to the total isotopic shift in uranium [68]. The field shift is the result of a change in the size and shape of the electric charge distribution of the nucleus [44]. The altered electric charge distribution is the result of differing energies of atomic electrons between isotopes [44]. The energies associated with the atomic electrons differ between isotopes because, although isotopes of an element share the same number of protons, the number of neutrons is different. The differing number of neutrons leads to different distribution probabilities for location of the protons between isotopes [44]. These differences

in the probability distribution of particles in the nucleus and the changed size and shape of the electric charge distribution affect the energy of an atomic level resulting in a field shift [44].

Hyperfine Structure

There are some isotopes which possess an odd number of nucleons. When there is an odd number of nucleons a nuclear magnetic moment results [44]. The nuclear magnetic moment causes magnetic hyperfine structure (HFS), which complicates the measurement of an isotopic shift [44]. The hyperfine structure consists of many closely packed spectral peaks which can appear as a band if the spectral analysis equipment cannot resolve the individual peaks. The measurement of an isotopic shift between a specific line and a band is troublesome because an assessment has to be made where to measure from within this hyperfine structure [44]. The HFS has been shown to be negligible in cases where the spectral line width is greater than 14.5 pm, but the spectral resolution of the equipment in this research is approximately 8 pm so HFS will be included in the fitting algorithms described in Chapter 3 [69].

LIBS Applicability for Uranium Isotopic Analysis

As discussed previously, LIBS is an emission-based technique that measures photon emissions principally from atoms. LIBS has been generally thought of as a measuring technique best suited for determining whether a particular element is present in a sample because, for most elements, the isotopic shift in electron energy levels is not sufficient to allow measurement except in very light or very heavy elements [70]. According to Mao et al., in the case of light elements, “the different masses of isotopes cause a relatively large fractional change in the mass of the atom, which in turn alters the electron motion with respect to the center of gravity of the atoms and hence the associated electronic energy levels” [70]. In the case of heavy atoms, “the large nucleus modifies the electronic energy level of the atom through interactions between the shape and the size of the nuclear charge distribution with the field of the electrons” [44, 70]. Fortunately, uranium is sufficiently heavy that the isotopic shift between ^{238}U and ^{235}U can be measured [68]. This section will analyze some of the recent developments and technical challenges reported by recent research involving LIBS.

Mass spectrometry systems are the acknowledged accuracy standard for isotopic measurement, but several benefits to using a LIBS system are discussed below [11-16]. Additionally, as the precision and accuracy of the LIBS systems continue to improve, there will be increasing applications where their accuracy is sufficient, especially when including initial and operating cost in the evaluation:

- MS systems must compensate for mass biases, which are estimates of isotopic ratios that do not match the true value, by using a mass basis correction. No mass bias correction is needed for uranium isotopic analysis in emission-based methods [13, 14, 69].
- The separation of the laser from the radioactive contamination is a large benefit in keeping the complex and expensive hardware clean and serviceable. Contamination is expected with a MS process [69].
- The range of photon-emission-based measurements offers the possibility of conducting an analysis from a greater distance than would be necessary to assure lack of radioactive contamination [69, 71].

There are still unknowns associated with LIBS processes that drive error potential into the measurements. Drawing on a solid ablation example to illustrate probable unknowns with gaseous LIBS, pulsed laser ablation is difficult to predict accurately in terms of exactly how much material will be ablated [72]. In addition to the unknown mass which becomes plasma, there is “no unified theory” of the “chemistry of the plasma” or the “aerosol properties” resulting from the ablated materials’ becoming plasma [72]. The potential variability in the mass that becomes plasma and the size of the plasma have the potential to affect the self-absorption of the emission.

There is another significant technical difference between LIBS systems having to do with the speed of the laser that is being used. The speed of the laser refers to how quickly the laser can deliver energy or provide a pulse to a target. The current standard within the industry is the nanosecond laser, that is, a laser that can deliver an individual pulse over a period measured in nanoseconds [73]. There has been an advancement to femtosecond lasers, ones which can deliver a pulse in a period measured in femtoseconds. The ability to deliver the pulse in femtoseconds changes the nature of the interaction the laser has with the material it is interrogating as well as the plasma created in the process. The proportion of laser energy absorbed or even reflected by the plasma depends on many conditions, including time, temperature, electron density, and mass density [72].

There have been many articles published which compare the performance of nanosecond versus femtosecond laser pulse widths and what effects the pulse widths have on the LIBS technique when applied to solid samples [54, 62, 63, 72, 74]. There have even been arguments made that the speed of the pulse is not important compared to the energy fluence of the laser [62]. There is a threshold of about 50 to 75 mJ per pulse required to create plasma in air for instance [46]. Obviously, more than this threshold energy is required to assure that plasma is created regardless of the material form [46]. It is also generally understood that increased energy produces increased plasma volume [46]. In the case of uranium, additional energy may be a benefit because uranium is not atomized

efficiently in low energy plasmas [75]. There is significant ongoing research targeted at understanding the differences between LIBS techniques conducted with nanosecond versus femtosecond lasers. This research adds to that body of knowledge.

Ablation of Solids

The differing characteristics of nanosecond and femtosecond lasers is important in both gaseous samples, which are the targets for this research, and solid compounds. There is limited information available regarding the effect that femtosecond and nanosecond lasers may have on the process gas within a GCEP. Therefore, a brief discussion of the recent research of femtosecond versus nanosecond laser ablation of solids is included below. This information will aid in understanding the impact of different speed lasers when analyzing the relative micro-destructive impacts of femtosecond versus nanosecond lasers that can be expected when applied to UF_6 gas.

In general, when targeting solids, nanosecond lasers make larger diameter, more melted-looking craters, whereas femtosecond lasers tend to produce more regular appearing craters. In a recent comparative study of femtosecond versus nanosecond lasers the nanosecond laser produced a 300 µm diameter crater 13 µm deep after 30 pulses [74]. The femtosecond laser produced a comparatively small 75 µm diameter crater that was 150 µm deep after 500 pulses [74]. In addition to the reduction in crater diameter, the femtosecond laser transfers little heat into the surrounding material in comparison with the nanosecond equivalent [76]. This is in part due to the electron-to-electron collisions which are the mechanism for reestablishing thermal equilibrium [76]. The research reported on solid material ablation leads to the conclusion that the femtosecond lasers will produce less micro-destruction of UF_6 than equivalent nanosecond lasers, potentially reducing the risk to plant operating equipment.

Nanosecond LIBS

Currently, nanosecond lasers are more common in LIBS systems than femtosecond lasers are. This is likely due to the laser plasma heating offered by nanosecond lasers because they offer a larger, longer lasting plasma as seen in Fig. 2.1 [72]. The larger and longer lasting plasma, shown in Fig. 2.2 [72], makes emission collection easier. Plasma heating can be extended even further with the addition of follow-on nanosecond laser pulse(s) to further excite the species in the plasma, although it should be noted that this is possible with femtosecond lasers as well [77].

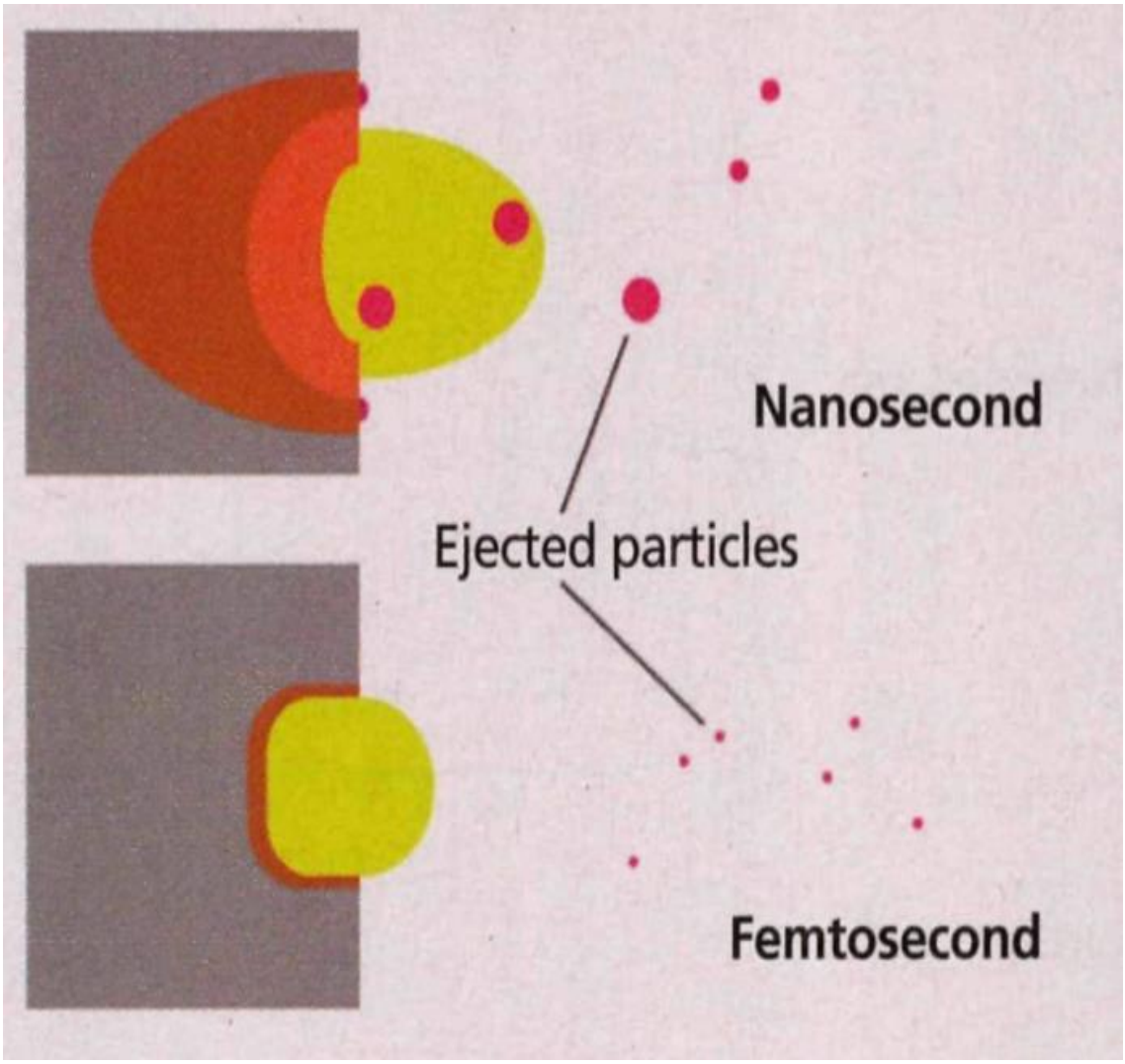


Figure 2.1. Russo et al. concept diagram representing direct ejection of particles. The particle sizes and size distribution are related to the heated volume. The paper notes variability of particle size associated with the nanosecond pulse [72].

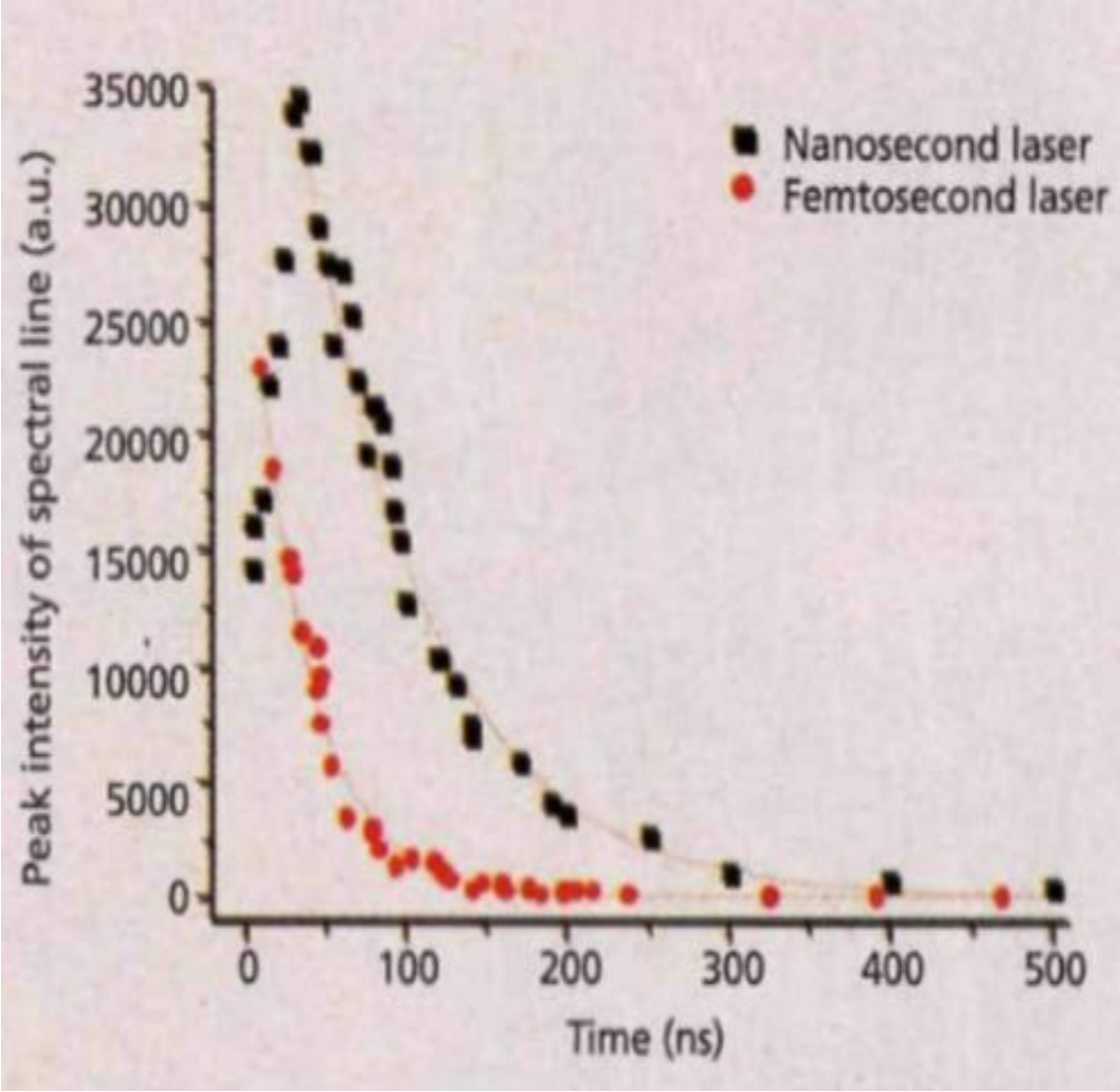


Figure 2.2. Graph by Russo et al. shows relative decay rates of measured optical emission from two plasmas initiated with lasers having all properties equal except the pulse duration [72].

An early study comparing nanosecond and femtosecond lasers' ablation performance at atmospheric pressure found that the nanosecond laser produced a slower and more predictable aerosol expansion [73]. Additionally, the researchers concluded that the nanosecond aerosol trajectories could be predicted using computational fluid dynamics whereas the femtosecond plumes resulted in a four times greater dispersion distance and higher velocity variability [73].

Femtosecond LIBS

The energy absorption in the interrogated material is greater with a femtosecond laser based in part on the high energy/area-time [72]. The femtosecond laser drives nonlinear multiphoton absorption which limits the penetration depth of the laser pulse [72]. The result of this nonlinear behavior is that the energy per unit volume from a femtosecond laser pulse is greater than what can be delivered by nanosecond laser pulses [72]. In fact, the nanosecond laser is still illuminating the sample while the plasma is expanding [19]. This can be envisioned by looking at Fig. 2.3 created by Labutin et al., which depicts the ablation of material resulting from a femtosecond laser pulse at various time steps following the initial interaction of the pulse with the material [76]. The femtosecond pulse is over before any mass can leave the surface [72].

The femtosecond laser essentially provides an abrupt powerful pulse and then clears the way for the collection of the emission to begin before any of the interrogated material can escape. Russo et al. confirmed that this is the case by using femtosecond time-resolved imaging targeted above the sample surface [72]. Their images confirmed that no physical entity departs the surface on the femtosecond time scale [72]. However, electrons have been measured picoseconds after the laser pulse [72, 78].

A benefit of the abrupt powerful pulse described above is that, in the case of a solid, there is less melting of the interrogated material when using femtosecond pulses than is observed with nanosecond pulse lasers. Russo et al. explain that heating to a melt phase is to be avoided when possible, because the melting presents the opportunity that "preferential vaporization" and "elemental migration" can occur within the bulk material [72]. These processes can begin to occur after a single pulse and serve to reduce accuracy of the analysis because the stoichiometry of the sample being ablated is reduced [72]. Clearly the femtosecond pulse serves to reduce or eliminate these processes in solids. The heat-affected zone is reduced as a result of the femtosecond pulse. The reduction in the heat-affected zone serves to reduce the volume of material ablated to the nanometer range [72].

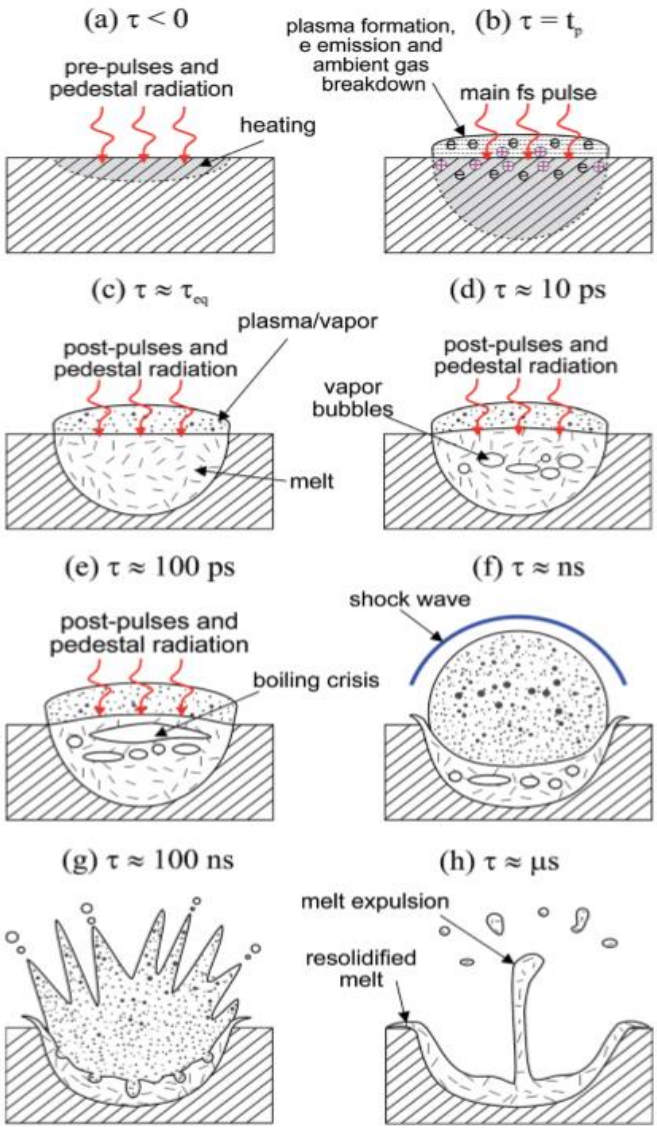


Figure 2.3. Plasma formation and ablation timeline by femtosecond laser illustration by Labutin et al. [76].

The reduction in ablated material combined with the high energy per unit volume produces smaller particles being ejected and nucleated as a result of femtosecond pulses [72]. There are similar advantages in gaseous femtoseconds LIBS which will be discussed later in Chapter 2.

Femtosecond laser ablation provides advantages for applications that need excellent precision in terms of focal volume, disassociation of molecules, and lack of interaction with the plasma once formed [77]. Additionally, although not explored in this research, the femtosecond lasers act quickly enough that researchers are presented the opportunity to excite (or more clearly re-excite) an existing plasma at different times within the plasma life cycle [77]. Conversely, the nanosecond laser pulse interacts with the plasma simply due to the length of the pulse, whereas the femtosecond laser offers an additional investigative tool due to the ability to vary the delay from an initial pulse to an additional pulse. This capability to deliver pulses of laser energy at discrete points within the plasma life cycle differentiates the femtosecond laser as an analysis tool from the nanosecond lasers which are still depositing energy even after the plasma has initially formed.

Emmert et al. conclude their comparison of nanosecond and femtosecond lasers for LIBS of depleted uranium metal with a statement indicative of the additional precision they observed in the femtosecond-produced spectral lines by describing what they call the “fingerprint lines” of uranium appearing earlier and without any significant plasma continuum, which was present in their nanosecond LIBS spectra, and they cast a positive light on future femtosecond research [74]. The “fingerprint lines” are the prominent spectral emissions from depleted uranium metal generated by fs-LIBS and compared with nanosecond LIBS in their study [74].

As stated initially, this discussion of the benefits of femtosecond LIBS, including solids, indicates potential benefits to using femtosecond LIBS to analyze UF_6 gas. These positive indications were a significant motivator for this research.

Gaseous Femtosecond LIBS

Literature pertaining to gaseous femtosecond LIBS, particularly as it relates to isotopic measurement of nuclear material, is less prevalent than for solids, but there are publications which have relevance for fs-LIBS of UF_6 for assay measurement. Hsu et al. compared femtosecond and nanosecond LIBS in a gas sensing experiment conducted at elevated pressure [79]. They found that while signal level and stability of ns-LIBS “significantly decrease with increase in pressure”, fs-LIBS signal level “increases with the increase in pressure while maintaining stability in the pressure range of 750 – 30,000 Torr [79]. This result

obtained by Hsu was conducted on nitrogen rather than UF_6 and was performed under significantly different pressure conditions, but highlights the value of conducting this research at different pressures to determine whether the benefits of pressures below 40 Torr observed during nanosecond laser-based LISA-UE research apply to fs-LIBS [79, 80].

Cao et al. conducted a study of low pressure argon which bounds the pressure ranges tested in this research [81]. They found that changes in the ambient pressure from 4 Torr to 638 Torr "produces large variation in emission intensity and plasma lifetime" [81]. Additionally they found that the ambient pressure had strong influence on how detectable various emission lines would be with some favoring lower pressures while others favored high pressure [81].

Heins and Guo conducted experiments testing the stability of fs-LIBS in gases and determined that fs-LIBS has intrinsically higher stability in gas relative to nanosecond-pulse LIBS [82]. Their tests were conducted on atmospheric pressure argon, krypton, and xenon with a Ti:sapphire laser generating a 68 fs pulse at 800 nm [82]. Heins and Guo attribute the stability that they observed to multiphoton ionization (MPI), which they argue is stable at the high energy intensities delivered by femtosecond lasers and much less stable with nanosecond laser LIBS [82].

Parameters that Impact Laser-Based Spectroscopy

Emission Spectrum and Line Selection

The selection of the spectral lines which are used in the isotopic analysis necessary for determining the assay of UF_6 is important. The choice of which spectral region and which specific emission lines to measure is influenced by line intensity, spectral interferences, continuum background emission, and self-absorption [83]. The goal in the selection is to pick lines where the isotopic shift between the isotopes of interest is greatest and where they can be observed most clearly. Many factors of the experimental setup determine how clearly the spectral lines can be measured. Additionally, some techniques attempt to glean data about the relative abundance of the isotopes by evaluating the area within the peak (without curve fitting) for the line of interest. This further necessitates that the spectral lines that are chosen be as separated from interfering or overlapping lines as possible.

The 424.437 nm line associated with ^{238}U is observed to be the most commonly selected. This is primarily because it is offset from the 424.412 nm line associated with ^{235}U by 25 picometers, which is a large enough separation that many spectrometers can easily resolve the difference of these two peaks and thereby enable at least coarse isotopic analysis [66]. In addition to the isotopic

shift, the intensity of the spectra is an important consideration when determining which wavelengths to evaluate for assay measurement. Research by Chinni et al. on the emission intensity of LIBS spectra of depleted uranium metal indicates that the intensity of the emitted light is near optimum between 400 nm and 500 nm [84].

There are benefits to be gained from the analysis of multiple peaks to determine assay with ultimate precision achieved after 21 lines are included in the measuring algorithm [85]. There are algorithms which take advantage of peaks as well as spectral formations to more fully resolve the isotopic makeup of the interrogated material. These techniques require additional measurement beyond the 424.437 nm and 424.412 nm emissions discussed above.

Line Accuracy and Isotopic Shifts

In measuring assay with fs-LIBS, it is critically important to know accurately where the uranium lines are located in the spectra and what isotopic shift is to be expected between the uranium isotopes of interest. The wavelength of the uranium lines varies to some degree in the published research. Chapter 4 includes discussion of how the fitting algorithm in this research handles isotopic pairs that do not agree with the dominant 424.4372 / 424.4122 nm isotopic pair, as could be the case if there were an error in the location of some of the uranium lines.

There is growing interest in improving the accuracy of isotopic analysis using multiple spectral lines and isotopic shift [67, 85, 86]. This increases the challenge of line selection because, in addition to issues discussed earlier in this section, the researcher must select a spectral region of interest, and then determine which of the lines and shifts that are confidently reported in published literature can be resolved and measured by the equipment that the researcher is using.

Song et al. conducted a process of line selection based on parameters that were relevant to their research and then provided an exhaustive summary of how the wavelengths and isotopic shifts that they used compared with the others that were currently published. This gave the reader an understanding of the data as well as provided confidence that the wavelengths and isotopic shifts used in their research were well supported by published literature [67].

A broader selection of lines for use in isotopic determination was published by Chan et al. which is very useful for those interested in uranium isotopics because it compiled experimentally determined line shifts from technical reports and documents that are no longer available to the general public [85]. The resulting lines that were identified had isotopic shifts greater than 10 picometers, had a

relatively strong signal-to-background-noise-ratio, and had minimal potential spectral interference from uranium itself [85].

Both the work of Song et al. and that of Chan et al. relied on accurate published energy levels and shifts for uranium. Jean Blaise published “Energy Levels for Atomic Uranium (U I)”[87]. Jean Blaise et. al. later published “Energy Levels and Isotopic Shifts for Singly Ionized Uranium (U II)”[88]. Then Chan et al. and Song et al. made use of the seminal information in these two publications [67, 85, 87, 88]. The first Blaise document is directly useful for the energy levels of Uranium I [85, 87]. The second required that published energy levels for Uranium II ^{234}U – ^{238}U be converted to ^{235}U – ^{238}U through a conversion factor [85, 88]. This research also makes use of these seminal works when searching for additional potential isotopic shifts which may be detectable in fs-LIBS spectra.

Effects of Pressure and Vacuum

The benefit of performing LIBS in reduced pressure environments has been well documented in the literature [89]. Choi et al. indicate that the benefits of reduced pressure include minimized Doppler, collisional, and Stark broadening [83]. Performing LIBS at reduced pressures (pressures below atmosphere) can result in enhanced spectra [83]. Again, drawing on examples from solid LIBS, these enhancements include an increase in spectral intensity, improved spectral resolution, increased ablation, and more uniform ablation craters. The LISA-UE research team researching nanosecond LIBS on gaseous UF_6 samples has similarly observed reduction in spectral clutter below 40 Torr with continued improvement down to 8 Torr [80]. These enhancements are generally seen when using both femtosecond and nanosecond lasers [89].

Extracting Isotopic Information from Spectra

There has already been significant development in the techniques which can be used to derive information from the captured spectra from LIBS-based processes. It is often the case that the best technique for executing additional analysis is not readily apparent at the outset of a project. For this reason, many techniques are often applied. The results of these techniques are then compared critically to determine which provides the most value to the end user of the data.

One of the first considerations is how many spectral lines should be included in an analysis. Although the result would vary between techniques and configurations, Chan et al. investigated the effect of increased spectral lines on isotopic accuracy [85]. In every method used, the precision improvements are miniscule beyond 20 spectral lines [85]. The conclusion Chan et al. draw is that signal strength outweighs isotopic shift in influencing the analytical performance

of the measurement technique; therefore, focus should be on enhanced light collection efficiency [85].

Once the spectra have been obtained, the challenge remains to determine the isotopic abundances of interest to the user. The approach described by Chan et al. where they use a simple two-component Lorentzian spectral fitting with constraints is the baseline method selected for this research [69]. As an example of the constraints, they include forcing the linewidths for the ^{235}U and ^{238}U components to be equivalent [69].

The most recent advancement in approaches to spectral fitting has been documented by Song et al. and additional publications by Chan et al. continue to evolve the approach [24, 27, 67]. The multiple-line-pair fitting algorithm requires development of a spectral line database [67]. The vicinity of the spectral data is selected based on the volume of high-resolution data already existing around the well-studied 424.437 nm line [67]. The range around that vicinity was selected based on an iterative process where Song et al. add spectral lines based initially on visually assessed strength and then continue adding lines until a satisfactory spectral fit is provided. The resulting 12-line pairs needed to provide a satisfactory fit between 424.300 nm and 424.500 nm are shown in Table 2.1 [67]. The multiple-line-pair approach improved the absolute isotopic ratio of ^{235}U from about 4% when a single line pair is used to about 1% when the multiple-line-pair fitting is applied [67].

Principal Component Analysis and Partial Least Squares Regression

Among the most commonly reported techniques for analysis of spectral data resulting from LIBS-type interrogations is Partial Least Squares (PLS) regression and Principal Component Analysis (PCA) [60, 67, 70, 85, 90, 91]. Advanced versions of numerical techniques are investigated in this research because they offer an alternative approach to attempting to understand the assay of a material based on its spectra without the need for detailed isotopic shift information.

Singular Value Decomposition

The default algorithm for computing PCA, after mean centering the data, is the Singular Value Decomposition (SVD) [92]. Recall that SVD of a matrix is a factorization of that matrix into three matrices as shown in (1).

$$A = U S V' \quad (1)$$

Table 2.1. 12 Isotopic Shifts (IS) Identified by Song et al. [51]

Isotopic Pair #	U-238	U-235	IS (nm)	IS (pm)
1	424.4372	424.4122	0.025	25
2	424.3085	424.3065	0.002	2
3	424.3221	424.3241	0.002	2
4	424.3344	424.3127	0.0217	21.7
5	424.3546	424.3546	0	0
6	424.3780	424.3705	0.0075	7.5
7	424.3914	424.3822	0.0092	9.2
8	424.3917	424.3850	0.0067	6.7
9	424.4444	424.4409	0.0035	3.5
10	424.4695	424.4649	0.0046	4.6
11	424.4712	424.4683	0.0029	2.9
12	424.4883	424.4903	0.002	2

The matrix U has orthonormal columns, referred to as the left singular vectors. The singular values s_j are present in the major diagonal of the diagonal nonnegative matrix S. These values s_j are arranged from largest to smallest as the column number *j* increases [92, 93]. The matrix V is composed of orthonormal columns, called the right singular vectors. These are the vectors such that the singular value s_j in matrix S is the length of the projection of matrix A in the direction $V\ (:, j)$ [92, 93]. Mathematically, the vector direction is row *j* in the inverse matrix V^{-1}, but the properties of V computed in SVD make V^{-1}equal to the transpose $V'$of V itself.

In real-world applications of SVD, it is convenient to define the oriented energy of matrix A in vector direction $V(:, j)$ as shown in (2).

$$E_{V(:,j)}(A) = (A\,V(:,j)'\big(A\,V(:,j)\big) = \big||AV(:,j)|\big|^2 = s_j^2 \qquad (2)$$

The ordering of the singular values $s_j$from largest to smallest means the corresponding columns *j* in matrix V are orthonormal external directions for maximum to minimum values of oriented energy. In fact, the direction vector *V(:,1)* with index *j = 1* computed by SVD is optimal in the sense that no other vector direction exists that gives a larger oriented energy for matrix *A* [92, 93]. SVD has been used to analyze data captured from LIBS systems [94]. However, recall SVD only offers insight pertaining to a single matrix.

Generalized Singular Value Decomposition

SVD theory and applications were expanded with the notable publication of Generalized SVD (GSVD) for two matrices [95]. A subsequent contribution by De Lathauwer et al. proposes the application of GSVD to signal processing of digitized data [96].

Let A_1 and A_2 be matrices with full-column rank (no linearly dependent columns) and the same number of columns (they can have different numbers of rows). Generalized singular values can be interpreted as quantifying the significance or relative information content of columns in the shared matrix X in the decompositions shown in (3) and (4) [92, 95, 97, 98].

$$A_1 = U_1\,S_1\,X' \qquad (3)$$

$$A_2 = U_2\,S_2\,X' \qquad (4)$$

It is important to understand that (3) and (4) are not SVD computed separately for the two matrices. GSVD is computed for both matrices simultaneously and the shared matrix X is used in both decompositions [95, 98].The columns of X are the generalized right singular vectors. Unlike SVD, these columns are neither orthogonal nor normalized to vector-length 1; however, the columns are linearly independent and there is a well-defined inverse matrix X^{-1}.

The singular values s_{1j} in diagonal nonnegative matrix S_1 are ordered by increasing values and the singular values s_{2j} in matrix S_2 are ordered by decreasing value. The generalized singular values gs_j are the ratios $gs_j = \frac{s_{1j}}{s_{2j}}$ in increasing value for $j = 1,2, \dots, n$.

There is an important GSVD optimality result for oriented energy ratios [95, 98].

- If $gs_j = 1$, then the two matrices (signals) have equal oriented energy in the direction that is row *j* in the inverse matrix X^{-1}. This means that projecting in that direction does not distinguish between the two signals by the energy projected in the direction.
- If $gs_j > 1$, then in direction row *j* in X^{-1} the oriented energy in A_1 is bigger than the oriented energy in A_2.
- If $gs_j < 1$, then the direction has the opposite meaning.

The optimality property of GSVD is that the best vector direction for signal A_1 over signal A_2 is the direction row in X^{-1} for which the generalized singular value gs_j has the largest value [95, 98]. Similarly, the vector direction for which gs_j has its smallest value is the best vector direction for A_2 over A_1. The GSVD computation automatically finds these optimal vector-directions.

Higher Order Generalized Singular Value Decomposition

In 2011 another advancement was published; it leveraged SVD to what was termed Higher Order Generalized SVD (HOGSVD) to make an assessment of the degree to which the genes of different genetic organisms matched [97]. The original algorithm for HOGSVD permits the simultaneous decomposition of two or more matrices that have full-column rank and the same number of columns (the matrices can have different numbers of rows). The most recent version removes the constraint to full-column rank but does require the same number of columns [99]. GSVD can now be viewed as HOGSVD applied to two matrices (samples of two digitized signals) that do not have to be full-column rank. In essence HOGSVD is a simultaneous singular value-based decomposition of multiple matrices which can reveal the geometric similarities (quantified in oriented energy values) that all datasets have in common as well as pairwise

dissimilarities that distinguish one dataset from another [92]. HOGSVD has the form shown in (5), (6), and (7).

$$A_1 = U_1 S_1 X' \quad (5)$$

$$A_2 = U_2 S_2 X' \quad (6)$$

$$\ldots$$

$$A_n = U_n S_n X' \quad (7)$$

Usually there is not a single “best direction” for maximum or minimum oriented energy ratio of all pairs of matrices simultaneously in the case of HOGSVD because the maximum oriented energy ratio will generally occur in a different direction for each different pair of matrices [92]. This is because some pairs may have a common geometric structure in a certain direction that other pairs do not.

Advanced SVD of LIBS Spectra

The SVD techniques that have been applied to LIBS spectra appear to have focused on attempting to ascertain the presence or absence of a particular element or material [94]. There appears to be a gap in the literature related to the application of advanced or higher order SVD analysis techniques specifically to isotopic analysis.

Singular value decomposition approaches are attractive because the computation burden can be low relative to other post-processing techniques. This lower burden could be critical to support continuous monitoring of the isotopic makeup of UF_6 gas flowing through a GCEP process pipe.

Dynamic Time Warp

Dynamic Time Warping (DTW) is typically thought of as a means of measuring the similarity between two signals (one dimensional numerical sequences) when both signals are scanned left-to-right [100]. DTW finds the optimal alignment between two sequences [100]. The signals are numerical values, such as the emission intensities captured by a spectrometer and ICCD. DTW can be applied to find the optimal alignment between two spectra. DTW accomplishes this by shifting datapoints in either spectrum locally by small amounts to minimize the overall error between the two (e.g., Euclidian error) while preserving the left-to-

right ordering of all the datapoints preserving features that may be present in both [100]. DTW is conveniently computed by dynamic programming by the MATLAB function **dtw**.

There will be two different applications of DTW in this research. First, when attempting to find an average representative spectrum for 5 captured spectra, DTW will be applied to determine the best representation of the spectral features included in the 5 individual spectra even if they were collected under different Stark shift and Stark broadening conditions. The second application will be through using the DTW-error or cost of the optimal alignment between two spectra [100]. The cost of the optimal alignment measures how dissimilar the sequences are after the optimal alignment achieved by DTW [100]. This DTW-error value is included as one of the features evaluated when attempting to classify an unknown spectrum based on the known assay spectrum it most closely matches.

Current Approaches and How this Research Fits

Technical Challenges

Accuracy Sufficient for Nuclear Security

The nuclear security function that the IAEA performs does not require the same level of accuracy that commercial nuclear research and development require. The IAEA needs to assure that the facility is operating within the agreed limits. The precision offered by the currently available systems described in the introduction have historically been viewed to provide adequate accuracy for that mission [20, 21] .

The IAEA is at times prevented from gaining detailed information about the facilities that they are monitoring owing to concerns that there is proprietary data about the enrichment technology that could be gained from greater accuracy. In the instances where the IAEA has installed systems like OLEM, the measurements have been taken outside the cascade of centrifuges itself on the piping feeding or withdrawing the cascade as a whole.

The problem is that if the IAEA is both excluded from the cascade itself and pushed to use online measuring systems that have relatively low accuracy and/or only permitted to capture hard samples for validation on a sporadic basis, the opportunity to operate outside the declared treaty limits exists. One of the potential future benefits of the current fs-LIBS research is the ability to gain higher precision real-time insight into the ramp-ups in inventory, the ramp-downs

in inventory, and the maintenance cycles occurring at the facility in order to understand whether the entire picture adds up to compliance.

Accuracy Sufficient for Nuclear R&D

The mass spectrometer is the gold standard for accuracy in UF_6 assay. The precision can be 0.03% relative abundance [11]. The precision is more critical in nuclear research and development because the errors inherent with systems such as COMPUCEA can cause significant uncertainty in the measurement of a centrifuge machine's or a cascade's separative work. For clarity, this research into fs-LIBS addresses the measuring technique that may enable future on-line measurement of enrichment processes, but does not seek to address the modifications needed to transition to on-line assay measurement.

Continuous Measurement Ability

The presence of UO_2F_2 deposits in the process piping presents a significant problem for the currently deployed continuous assay monitoring systems. These systems must estimate the amount of deposit and subtract the portion of the response associated with the UO_2F_2 from the total measured gamma signal to arrive at an assay assessment. Deposited UO_2F_2 was expected to be an issue for laser-based techniques as well, although it manifests itself in the form of a signal impedance due to reduced transparency of the windows which are necessary to allow laser light into the UF_6 pipework or to get the spectral emission out for collection and evaluation.

There have been recent reports of precipitate forming in the UF_6 gas sample chambers of the type used in this research without complete understanding of what the precipitate is or what may be causing it [24]. The drivers for this precipitate are noted by Chan et al., as areas where additional research is needed [24]. As will be discussed later, the precipitate formed in the course of this research as well. The precipitate does impede the collection of plasma emission.

Micro-Destructive Sampling Ramifications

A significant consideration that must be taken into account in the use of LIBS-based assay measurement is the micro-destructive nature of the technique. The implications of the micro-destructive assay measurement are not yet known to gaseous centrifuge plant operators. This is one of the areas where additional research is needed to fully understand the implications of any future transition to online measurement applications.

There had been a void in an explanation of what would be expected to occur within a UF_6 gas stream as a result of the laser interrogation and resulting plasma-induced dissociation of the UF_6. Early reporting by Dr. Leigh Martin indicates that, based on initial testing, UF_6 will recombine quickly following the plasma dissociation [101]. This conclusion was later supported by months of LIBS interrogation of samples which would have been consumed in weeks if the plasma dissociation was not followed by any recombination [80].

Methods in Development (Emission only)

Following a self-funded review, the NNSA selected the emission-based Laser Induced Spectrochemical Assay for Uranium Enrichment (LISA-UE) method for further development [3]. At the outset of that research, the basic method has been demonstrated for various enrichment samples of uranium-doped glass at different enrichment levels [67]. As this fs-LIBS research nears completion, the LISA-UE method has not yet been field-deployed but is far along its research plan and is making isotopic measurements on gaseous UF_6 in simulated field conditions [23, 24, 26, 27]. LISA-UE research continues to offer insight into the challenges of making accurate assay measurements with a portable system [24, 27].

The envisioned portability of the LISA-UE method would allow it to be connected to a cylinder or sampling port essentially anywhere within a declared facility [3, 10]. This portability and flexibility will answer many of the issues raised by IAEA inspectors summarized by Shephard [7]. To enable this portability, LISA-UE has been focused on nanosecond lasers. Based on the literature included in this review, additional precision was thought to potentially be available through the use of femtosecond lasers and enhanced algorithms for analyzing the resulting spectra [72].

There is an additional team with consistent input from Igor Jovanovic, researching laser-induced emission-based techniques for uranium isotopics. Morgan et al. has published recent research on the use of a compact Fabry-Perot etalon and a Czerny-Turner spectrometer to create a cheaper and more portable isotopic analysis system appropriate for uranium assay measurement [102]. Additional recent work from this group included a study by Ko et al. that proposed means by which a LIBS setup can be optimized and attests to the importance of future studies which are needed to better understand femtosecond pulse shapes and enhance the intensity of the emission lines in hopes of achieving higher intensity [103]. Javanovic and Hartig have collaborated on research focused toward enhancing the capability to execute standoff detection of uranium processing facilities as well [61].

There has been recent research conducted at the University of Tennessee that, while not directly supporting the isotopic analysis which is the focus of this review, provides fundamental information about LIBS related to uranium and/or gaseous centrifuge enrichment plant safeguards. [7, 8, 25, 104-106]. These publications will provide relevant information to nuclear security professionals intent on expanding the capability of LIBS-based measurement techniques.

Chapter Three

Materials and Methods

fs-LIBS System

Laser

The laser power source used to create the plasma in this research is the Spectra Physics Solstice ACE, shown in Fig. 3.1. The Solstice ACE provides 6 mJ of total energy and pulse widths of 94 femtoseconds [107]. The actual wavelength at installation measured 802 nm and the beam diameter is about 11 mm [107]. The laser operates with a repetition rate of 1 kHz.

One of the objectives of this research is to investigate the effect of reduced laser power. The laser power output was not intended to be adjusted on the Solstice ACE. There were settings that could be altered to result in lower power output, but the pulse width was no longer guaranteed to be in the femtosecond range if the power was reduced in this way. To create a low laser power configuration, the laser energy was redirected by 4 femtosecond-rated mirrors before reaching the focusing lens. Each redirection resulted in a loss of power. The laser energy reaching the focusing lens just outside the sample chamber was measured between 2 and 2.5 W in this configuration. The reduced power was still sufficient to produce a plasma in the UF_6 gas of the size shown in Fig. 3.2.

The femtosecond plasma is not very bright or persistent and therefore creates challenges collecting enough of the plasma emission for spectral analysis. To attempt to enhance the plasma emission, the table configuration was modified to avoid use of the steering mirrors. In this configuration the focusing lens and sample chamber were placed in line with the opening in the laser cabinet where the beam exits. This allowed focusing the laser energy without the use of any redirecting mirrors and increased the laser energy reaching the focusing lens to ~6 W. That increase produced a slightly larger and brighter plasma, shown in Fig. 3.3, which appeared more elongated than the ~2 W plasma.

Spectrometer

The spectrometer separates the collected light emitted from the plasma by wavelength. The wavelengths are separated spatially to allow measurement and integration over a time period by a gated detector which will be discussed below.



Figure 3.1. Solstice Ace femtosecond laser with steering mirror and power meter visible in the foreground

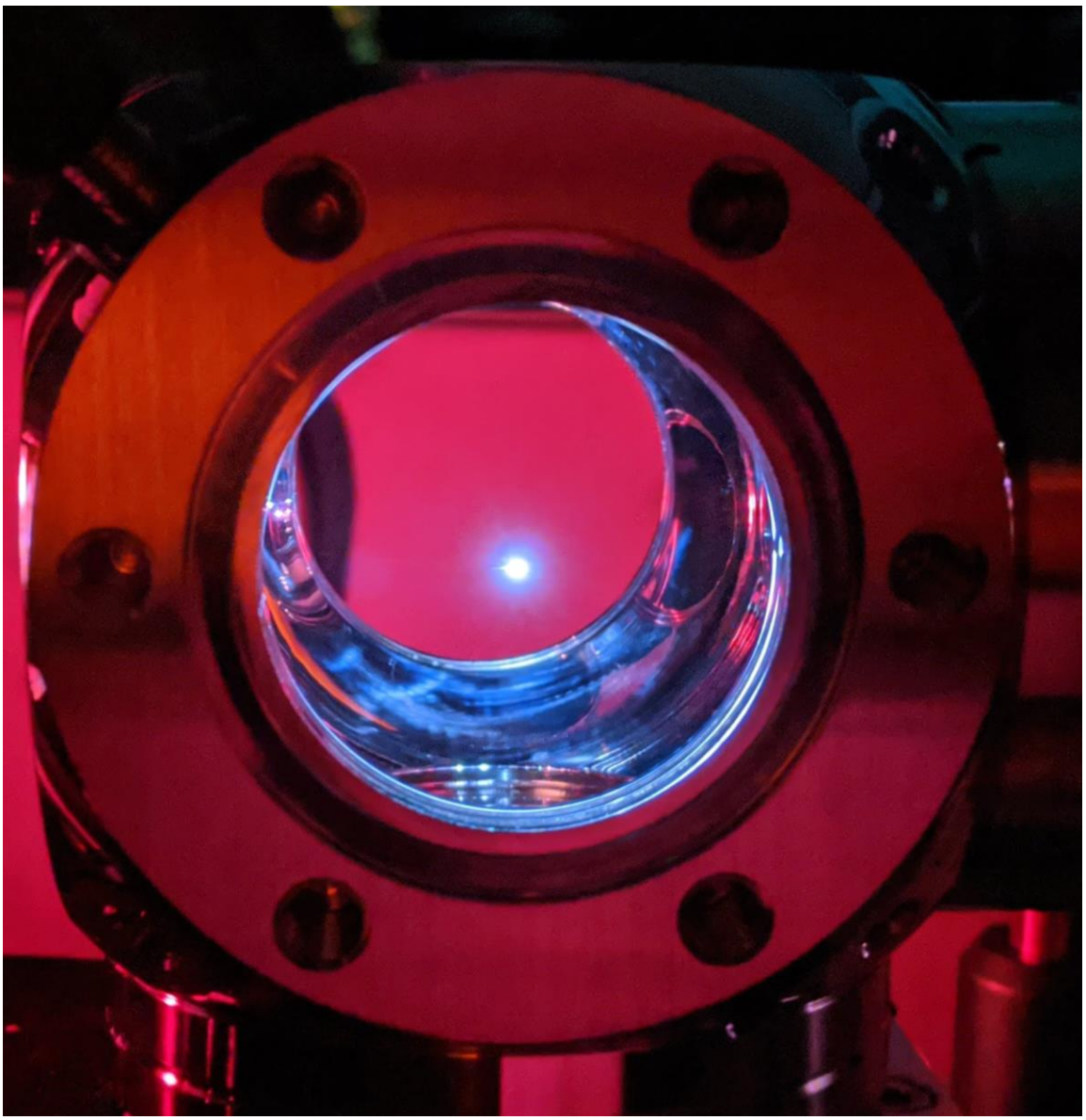


Figure 3.2. Plasma size observed in UF_6 gas resulting from ~2.5 W femtosecond laser. For scale, the plasma diameter is between 2 and 3 mm.

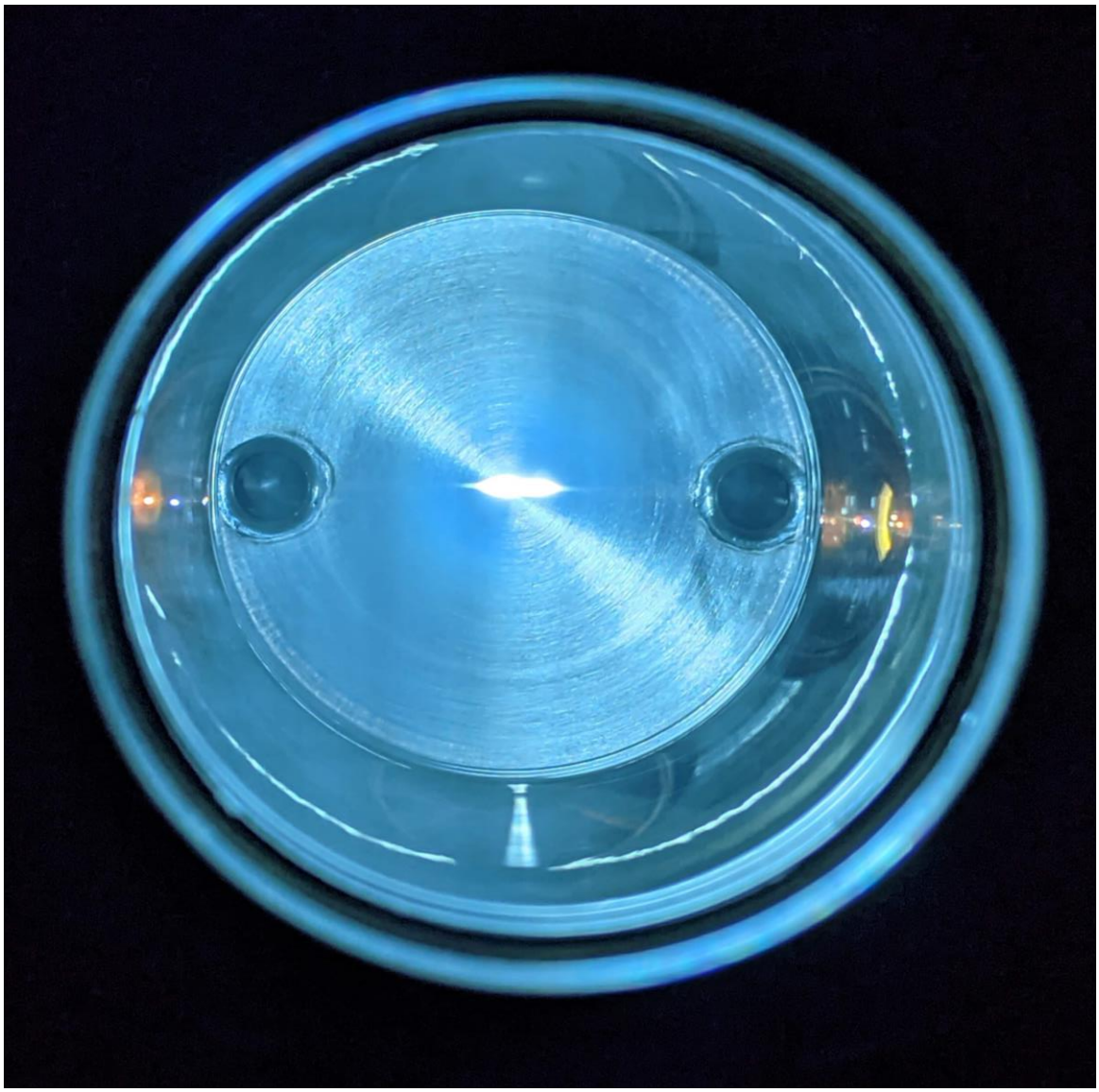


Figure 3.3. Plasma in UF_6 gas resulting from ~6 W femtosecond laser. For scale the plasma is approximately 5 mm long and 2 mm in height.

The combination of spectrometer and the gated detector can provide an assessment of the intensity of each wavelength of light that is collected. The isotope ratio of elements can be measured using sufficiently high-resolution spectrometers in association with a LIBS-type process [66, 108].

A Horiba 1250M spectrometer was selected based on the spectral dispersion provided by its length. The 1250M is configured with a 3600 grooves per millimeter grating. The selected grating balances the range to encompass the 424.437nm line and the need for high resolution for detecting the small isotopic shifts between ^{235}U and ^{238}U. The grating equation shown below has a theoretical maximum wavelength of 555 nm in the first order for a 3600 grooves per millimeter grating [109].

$$d * (\sin(\alpha) \pm \sin(\beta)) = n\lambda \quad (8)$$

In (8), d represents the distance between grooves, α is the angle of incidence, β is the angle of diffraction, n is the order, and λ is the wavelength. Horiba limits the recommended wavelength range from 150 nm to 450 nm, which is still sufficient for the planned experiments centered near 424.437 nm.

The spectrometer includes an entrance slit adjustable from 3 µm to 3 mm, a fully adjustable lens-based fiber optic interface, and fiber optic cable bundle with 19 individual fibers optimized to efficiently provide the collected light to the spectrometer. The fibers have a 200 µm core diameter and are arranged as a spot on the collection end and are stacked with a 240 µm center-to-center spacing on the spectrometer end to interface with the entrance slit. This configuration will not provide any geometric information about the plasma. The vertical arrangement of the fibers where they interface with the entrance slit of the spectrometer is confirmed by the presence of 19 detectable regions of greater light intensity when viewing an image of the spectrometer's output. Geometric information about the plasma is not necessary for the planned experiments.

Intensified Charge Coupled Devices

The spectrometer interfaces with an Andor iStar 334T Model # DH334T-18F-A3 (13 µm x 13 µm) Intensified Charge Coupled Device (ICCD). The primary characteristic that the ICCD offers is the ability to simultaneously monitor numerous bins of spectral energy being provided by the spectrometer rather than having to measure bins of energy one-at-a-time with a photo-multiplier tube. This simultaneous measurement is important because of the variability of the light source over short periods. This property is called shot-to-shot variability and it negatively impacts precision measurements when unable to measure the entire

spectrum at once. Another advantage of the ICCD is the ability to take relatively weak photon energy densities and amplify them to a more measurable signal.

Significant factors in the data that is collected during LIBS-based processes are the gate delay and the gate width used to collect the spectra. These are settings selected on the ICCD used in the experiment. The gate delay timing and gate width are critical parameters that require optimization based on laser power, sample material, pressure in the environment of the sample, and other factors. The Andor iStar 334T provides gate delay and gate width variability that are needed to research the plasma temporal characteristics and associated settings that yield the most useful spectra for making an isotopic determination. The optimum gate delay and gate width for this research differs from the published nanosecond laser induced plasma experiments conducted on UF_6 and must therefore be optimized for the fs-LIBS process.

Prior to initiating this research, the ICCD was evaluated to understand its performance characteristics. There are pixels which do report a higher energy offset than their neighbors. The effect of these pixels is minimized by both clipping the image to include only the pixel rows from 200 to 800 where the fiber optic cable shines most intensely and centering the spectrometer so that the region of evaluation falls between the areas where pixels with energy offsets are clustered.

During the majority of the fs-LIBS analysis of UF_6 assay, the ICCD detector offset was treated as a single constant which was subtracted from the captured image. The narrow wavelength region of interest permitted this assumption. However, as will be described in the results section, tests were conducted to confirm the validity of this approach.

Software

A computer program from Horiba, Lab Spec 6, was used to control the spectrometer [110]. Lab Spec 6 could have been used to control the ICCD when conducting scans of wavelength ranges that required the movement of the spectrometer and the data collection of the ICCD to be coordinated [110]. For the research described here the spectral range was sufficiently small that movement of the spectrometer was not required. Therefore, a computer program from Andor, Solis 4, was used to control the ICCD. Lab Spec 6 and Solis 4 both provide timing controls for gate delay and gate width based on trigger signals collected from the laser. The Solis 4 software was used to export text files of the images. The text file output consists of the emission measurement in arbitrary units (a.u.) for each pixel in a 1024 by 1024 format.

MATLAB 2021 was used for data analysis. Within the MATLAB environment a host of functions were used to accomplish the various analysis objectives. Among the most important was the function **fmincon** which was used to find optimum values for parameters in the various equations selected for fitting the spectral data captured experimentally. An adapted version of *Peakfit* was used for the peak analysis required to calibrate the collected spectra to wavelength [111].

System Performance

There were physical adjustments made to the spectrometer to sharpen the image and reduce tilt between the spectrometer and the ICCD. Following these physical adjustments the performance of the system was evaluated using a mercury pencil lamp and evaluation procedures based on Sansonetti et al. [112]. The resulting spectral dispersion of the fs-LIBS system is approximately 0.0025 nm per pixel. Based on evaluation of the peak center of the mercury emission lines near 313 nm, calculated for each pixel row individually between row 200 and row 800, there is a 1.5-pixel shift to the right. For example, if the center of the 313.1844 nm mercury emission line falls on pixel column 503 at row 200 the center of the emission line will fall on pixel column 504.5 at row 800. This tilt was too small to be corrected via physical rotation of the ICCD to spectrometer connection. The resulting spectral resolution is 0.008 nm based on the Full Width Half Max (FWHM) of the mercury emission lines near 313 nm. This resolution was determined to be sufficient for the research planned so no further tilt correction through software manipulation of the collected data was deemed necessary.

UF_6 Sample Material

The UF_6 material for this research was obtained from ORNL. Special thanks are owed to both Dr. Leigh Martin and Dr. Glenn Fugate for their assistance in sourcing this material. ORNL placed five different assays of UF_6 into the five sample chambers constructed for this testing. ORNL filled each of the sample chambers to approximately 60 Torr. The corresponding masses are shown in Table 3.1. Additionally, ORNL provided high precision mass spectrometry isotopic values for ^{235}U and ^{238}U.

Uranium Hexafluoride Sample Chambers

The sample chambers used in this research are essentially identical to those used by the LISA-UE researchers [3, 10, 26, 101]. As already mentioned, the intent is to minimize the number of variables, other than the femtosecond laser induced plasma, that differ between the UTK research and that of the LISA-UE.

Table 3.1. UF_6 Samples Provided by ORNL

Cell number	Isotope	Isotope weight (g)	Weight Percent U-235	ORNL Reported U-235 Enrichment
1	U-238	0.1796	4.417%	4.615%
	U-235	0.0083		
2	U-238	0.1862	0.268%	0.287%
	U-235	0.0005		
3	U-238	0.1251	37.823%	38.103%
	U-235	0.0761		
4	U-238	0.1514	18.339%	18.525%
	U-235	0.034		
5	U-238	0.069	62.088%	61.740%
	U-235	0.113		

The primary purpose of the sample chambers is to safely contain the UF_6 samples analyzed in this research. The material of construction is primarily stainless steel because of its compatibility with UF_6 gas [113]. The sample chambers must have provisions for optical access to the UF_6 gas to allow the laser energy to be focused into the sample chamber volume to create the plasma, permit the laser energy to pass through the sample chamber, and to allow plasma emission to be collected [26, 101]. Sapphire windows were selected for this purpose because of their resistance to UF_6 gas and their optical transmission range [26, 101].

The sample chamber also must have provisions for evacuation and filling through appropriate ports and valves capable of high vacuum operation and compatible with UF_6 gas [26, 101]. The sample chambers each received a dedicated MKS® Granville-Phillips® 902B Absolute Piezo Vacuum Transducer with a local display as well as provisions for connecting to a computer for logging of pressure data [26, 101]. Lastly, each sample chamber was equipped with a stainless cup on its bottom face to serve as a high-surface area interface with the thermoelectric cooler in the experiment setup [26, 101].

The five sample chambers assembled for this research were each leak tested by an inspector qualified to Level 3 of the Society for Non-Destructive Testing - Technical Committee - First Edition (SNT-TC-1A). Each sample chamber passed the leak testing process with a leak rate less than $1x10^{-8}$ standard cubic centimeters per second of gas flow.

The sample chambers were fluorinated to passivate the interior surfaces of the chamber against reaction with the UF_6. To accomplish this fluorination, the sample chambers were connected together and then connected to the fluorination system shown in Fig. 3.4.

The entire fluorination system with connected sample chambers was helium leak tested, and the system and the sample chambers were measured as having a leak rate less than $1*10^{-8}$ standard cubic centimeters per second of gas flow. The system was then heated to about 150°F. The fluorination system with the connected sample chambers was then held under vacuum for an extended period to remove as much residual moisture as possible. Next, 100% fluorine was then added in 2-5 Torr increments. A pause was taken between each incremental addition of fluorine to check for pressure stability and signs of an aggressive reaction. An aggressive reaction did not occur but would have been detected by warming of the sample chambers, tubing, or fittings. The system was filled in the incremental process until the pressure inside was approximately 30 Torr. This condition was then held for 24 hours.



Figure 3.4. Fluorination of Sample Chambers

Following the 24-hour hold, the heaters were de-energized and then, once at ambient temperature, the system was evacuated via chemical traps. The system was then raised to atmospheric pressure using nitrogen prior to disconnection of the chamber assemblies. The chambers were left at nominally atmospheric pressure nitrogen before being valved off and removed then removed from the fluorination system.

As mentioned earlier, ORNL provided the UF_6 gas samples for this research as well as the service of filling the sample chambers to approximately 60 Torr. This pressure was targeted because it is below the pressure where the UF_6 would be a solid at room temperature. The UF_6 pressure is further controlled using a thermoelectric cooler in contact with the stainless cup on the bottom of the sample chamber. There is no provision in the design to heat the sample chambers to increase the pressure.

Below room temperature and sub-atmospheric pressure (e.g., 9 Torr), the UF_6 is in a white crystalline form. Fig. 3.5 is a picture of how the UF_6 material appears in its solid form in the sample chambers following removal from the thermoelectric cooler.

UF_6 is a highly reactive material that is very moisture sensitive. The chemical reaction in (9) describes what occurs when UF_6 encounters the moisture present in air. This reaction is the reaction that would occur within the sample chambers if they experienced in-leakage of air.

$$UF_6 + 2\,H_2O \rightarrow UO_2F_2(S) + 4\,HF\,(g) \qquad (9)$$

The sample chamber design has proven very durable in testing at ORNL and LBNL [26]. The chambers are built with off-the-shelf parts intended for service in fluorine environments [113]. Initially there were concerns with potential in-leakage of air, consumption of UF_6 because of dissociation in the laser plasma, and fogging of the windows as reaction products built up on them [101]. Prior to use in this research, the chambers were tested by ORNL for leakage, laser damage to the windows, and for chemical compatibility [26, 101].

Fourier transform infrared (FTIR) analysis of the sample chambers containing UF_6 showed that the UF_6 was stable in the cell for over 8 days, indicating essentially no in-leakage of wet air [26, 101]. Fortunately, the sample chambers constructed for this research have now undergone months of testing at UTK with no major issues and only isolated occurrences of precipitate building up on the sapphire windows.

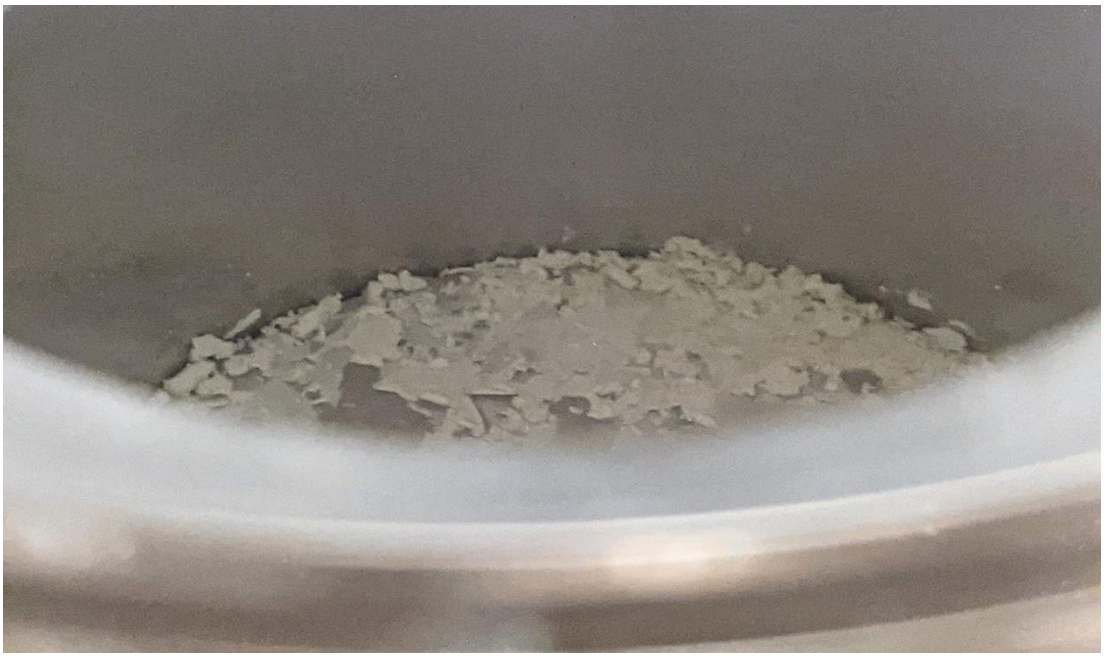


Figure 3.5. Crystalline UF_6

Spectral Line Database Generation

To prepare for analysis of the spectra in this research, development of a spectral line database was undertaken. There is no single source that provides the needed information. There are many potential isotopic shifts which could be observed and which might be useful for measuring assay. The challenge and hope in this research was to identify isotopic shifts visible in the fs-LIBS spectra that may not have been available to prior researchers using nanosecond LIBS techniques. Regardless of the laser energy source, isotopic shifts should meet the following criteria:

- The ^{235}U and ^{238}U candidate lines need to be strong optical emissions from fs-LIBS plasma [83, 85].
- The candidate lines should lack interference for both the ^{235}U and ^{238}U isotopes [83, 85].
- The candidate lines must be assignable to published optical emissions and published isotopic shifts.
- There must be an identifiable isotopic shift between the ^{235}U and ^{238}U isotope.
- The ideal situation is for the isotopic shift between the upper energy level of ^{235}U and ^{238}U and the isotopic shift between the lower energy level of ^{235}U and ^{238}U in a transition to be of different magnitude and direction [80].
- Conversely, if the isotopic shift between the upper energy level of ^{235}U and ^{238}U and the isotopic shift between the lower energy level of ^{235}U and ^{238}U in a transition are equal, there would be no observable difference between the isotopes in the transition [80].

Jean Blaise published a list of the energy levels of neutral atomic uranium which is useful when attempting to determine which transition may be the source of observed emissions in the captured spectra from the fs-LIBS experiments [87]. Subsequently Blaise published the energy levels of singly ionized uranium using ^{234}U [88]. The use of ^{234}U requires a correction factor to be relevant [85].

In 1980 Engleman et al. published the isotopic shifts for ^{234}U, which was selected because it lacks the HFS found in ^{235}U [114]. Similar to the work by Blaise, there would need to be a conversion performed to be relevant to ^{235}U [85]. Extensive lists of uranium emissions have been published by Richards, Palmer, and Payling which significantly expand the list of lines offer the opportunity to compare lines which appear in several lists but which differ slightly in exact value, as Song et al. noted and compared [39, 67, 115, 116].

A database by Kurucz et al. of atomic spectral lines has been made available via the Harvard-Smithsonian Center for Astrophysics which includes much of the spectral information that is useful for identification of lines [117]. However, it may

not include all the observed optical emissions, which is why the others are needed as well. The database includes the energy levels of the transitions and provides the wavelength in both air and vacuum [117].

These tables individually are not complete, but they do offer information that can be used in aggregate to assist in determination of which transitions are producing the observed optical emissions.

Candidate Spectral Window

One of the primary techniques employed by the LISA-UE team conducting research in this area used a multivariate nonlinear spectral fitting (MVNLSF) applied to the LIBS spectra, which initially relied on the 424.437 nm peak being in the spectral range [67]. Unfortunately, recent publications from the LISA-UE team indicate that the presence of self-absorption of the 424.437 nm resonance line is causing bias to reported enrichments [24, 27]. After extensive testing to find collection parameters which minimize this effect or analysis techniques which can compensate for it, the LISA-UE researchers concluded that the best approach is to avoid self-absorption by using other uranium emission lines that are not affected by self-absorption but which do offer sufficient isotopic shifts to extract isotopic enrichment information [24, 27]. However, the bulk of the published isotopic shift research has focused on the 424.437 nm range. This was another reason that this research elected to remain focused on the 424.437 nm range. There is also a need to explore whether the self-absorption reported by the LISA-UE team is altered through use of a femtosecond laser.

Overview of Experimental Procedure

The experimental procedure proceeds, as described in Chapter 2 for any LIBS process, except that a femtosecond laser is used. Therefore, the fs-LIBS testing method is very similar to the LISA-UE method which involves direct coupling of a small gas chamber with optical access to UF_6 gas contained within [10]. This small gas sample chamber is the experimental substitute for a component of the process gas system of a gaseous centrifuge enrichment facility [10]. Fig. 3.6 depicts the equipment arrangement for fs-LIBS testing.

The testing begins by establishing the thermal condition for the sample chamber, either allowing it to remain at room temperature or activating the thermoelectric cooler that the sample chamber sits on during testing. The conduction between the thermoelectric cooler and sample chamber is enhanced by moistening the interface with alcohol before setting the sample chamber on the thermoelectric cooler.

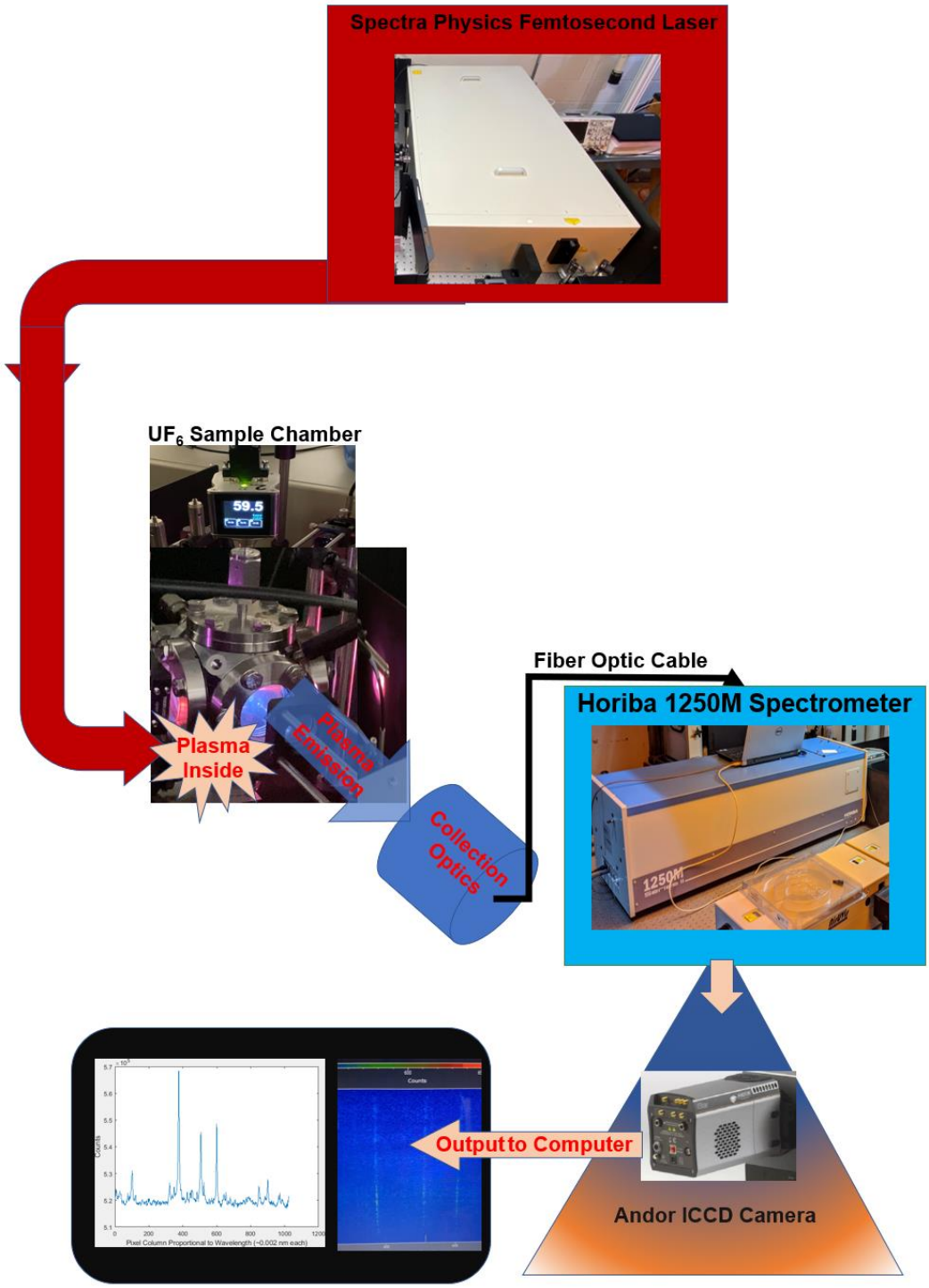


Figure 3.6. fs-LIBS Testing arrangement

The sample chamber is exposed only to cooling and at no point requires heating. The sample chamber is shown in position on top of the thermoelectric cooler in Fig. 3.6. The sample chamber pressure is displayed and logged by the vacuum gauge mounted atop the sample chamber.

As noted previously, the experiment plan for this research uses the Spectra Physics Solstice ACE femtosecond laser to create a plasma inside the sample chambers containing the UF_6 at the assays shown in Table 3.1. The femtosecond laser, shown in the red box in Fig. 3.6, is focused into the UF_6 gas sample chamber through the optical port.

The laser gas interaction creates a transient high-temperature (thousands of degrees Kelvin) plasma excitation source [10]. The high-temperature plasma is capable of breaking down the chemical bonds in the UF_6 [10]. The breakdown of the UF_6 into its constituent atoms creates the opportunity to promote some of the atoms into their excited states which, through radiative decay, emit photons that are characteristic of their elemental and isotopic identities [10].

The emission spectra are captured through an additional optical port, gathered by the collection optics, and routed to a spectrometer [10]. The collection optics consist of lenses which collimate the light and route it into a reflective collimator. The reflective collimator is connected to the input slit of the spectrometer via a fiber optic cable. The collection optics are depicted by the blue cylinder in Fig. 3.6.

The entrance slit is set to an opening of 20 micrometers based on optimization experiments conducted using a mercury lamp. The spectrometer is shown in the blue square of Fig. 3.6. The Horiba 1250 M Spectrometer is equipped with a 3600 grooves-per-millimeter grating. The diffracted plasma emission leaves the spectrometer to be measured by the ICCD which reveals spectral lines from atomic emissions [10]. The Andor Istar 334T ICCD measures the diffracted emissions and is shown in the multicolor triangle in Fig. 3.6.

After the spectra are captured, they are analyzed using various fitting methods to report an assay of the UF_6 contained in the sample chamber. Although the experiments were conducted on 5 different sample chambers, each containing a different assay of UF_6, much of the data reporting associated with the low power configuration is focused on 4 distinct assays because one of the sample chambers experienced formations of a precipitate on the collection window. This precipitate affected the sample chamber filled with 38.103% enriched UF_6 and hampered data collection because the relative weak plasma emission associated with the low power configuration was largely blocked by the precipitate layer.

Laser, ICCD, and Plasma Emission Timing Coordination

There are several timing characteristics monitored through an oscilloscope which are key to ensuring that the testing process is effectively investigating the temporal nature of the plasma. Timing information associated with gate delay, gate width, and exposure are recorded for each captured spectrum during the testing. The timing information remains linked to the spectra during post processing and eventual determination of an isotopic ratio of ^{235}U to ^{238}U in the sample. A central component of this research is determining where in the plasma life cycle the most valuable emissions occur for making an assessment of assay.

The most important timing signal to be monitored is the trigger pulse from the femtosecond laser. It is the baseline used for timing of other components in the fs-LIBS setup. Another important measurement is collected from a Thorlabs DET10A2 detector. It captures the time after the trigger pulse when either the laser scattering or the plasma emission triggers a response in the detector. Although this detector is insufficient to track the femtosecond laser pulse itself, it is useful to make a repeatable assessment of the time between the trigger signal and the beginning of the laser scattering or plasma emission. The measurement is key to establishing an offset to the gate delay values entered into the ICCD control software to ensure that the ICCD's data collection occurs during the plasma life cycle and that the gate delay and gate width occur at known points in time relative to the plasma emission initiation.

The Andor ICCD timing is based on the laser's trigger signal. The ICCD also provides signals associated with the opening and closing of its shutter that are monitored on the oscilloscope. These signals are largely used as a quality check to ensure that the ICCD shutter openings and closings are occurring when intended relative to the laser trigger signal and the initiation of plasma emission.

The oscilloscope monitoring of the timing signals coming from the laser, ICCD, and the plasma is vital to assure confidence that the testing is occurring in a coordinated fashion to extract the maximum amount of temporally resolved data from the fs-LIBS process. The collection and display of all this timing information on a single display provides a clear depiction of the relative timing of all the key testing parameters.

In actual practice over the course of the research, the time between the laser trigger and the emission of light varied slightly. Initial testing conducted in air at atmospheric pressure yielded an offset of 83 ns between the trigger pulse and the photocell response. Later in the research, the time between the trigger signal and the photocell response was shortened to 75 ns and then later measured to be only 70 ns. The variables that play a role in these times are the pressure of the medium in which the plasma is being created, the material being interrogated

by the fs-LIBS process, and the repairs and adjustments made by the Spectra Physics technician throughout this research to keep the laser operating at peak performance.

Parameters Investigated

Laser power and energy density

The Solstice Ace femtosecond laser produces a more energy-dense pulse than is typical from a nanosecond laser. Although the energy density of the pulse is greater, the plasma produced by a femtosecond laser tends to be smaller than a similar nanosecond laser. This reduced plasma size has an effect on the emitted light, which can be readily observed when comparing the plasma in Fig. 3.2 and Fig. 3.3.

Originally, it was thought that because the plasma is created with a more intense pulse, there would be differences in the energy levels of uranium that are populated by the plasma impulse as well as differences in the resulting emissions' ability to reach the detector. Because of the complexity of plasma physics, laser power had been planned to be adjustable to determine what effect the energy input has on the resulting spectra's ability to yield accurate assay measurements.

The power of the Solstice Laser is not intended to be adjusted. Reductions in power have the potential to increase the length of the laser pulse beyond the targeted 100 femtosecond pulse [107]. Despite the use of steering optics intended for femtosecond lasers, power reductions were observed along the beam path. The inefficiencies in the steering mirrors reduced the power from ~6 watts coming from the laser to ~ 2 watts as the beam encountered the focusing optics at the sample stage in what became known as the low power configuration for fs-LIBS testing.

Achieving the maximum power deposition into the sample chamber involved rearranging the equipment layout to permit the sample chambers to be located in line with the laser emission and at the appropriate height to avoid the use of any steering mirrors. This physical arrangement is used for the HPHP and HPLP testing configurations. The physical configuration is shown in Fig. 3.7. The sample chamber is shown in the center of the figure with its pressure transducer just outside of the top of the image. The femtosecond laser is on the right side of the image. The emitted beam from the femtosecond laser travels directly to a focusing optic with a 75 mm focal length, placing the plasma in the center of the sample chamber. After creating the plasma inside the sample chamber, the beam continues and can be seen on the left side of the image against the beam stop.

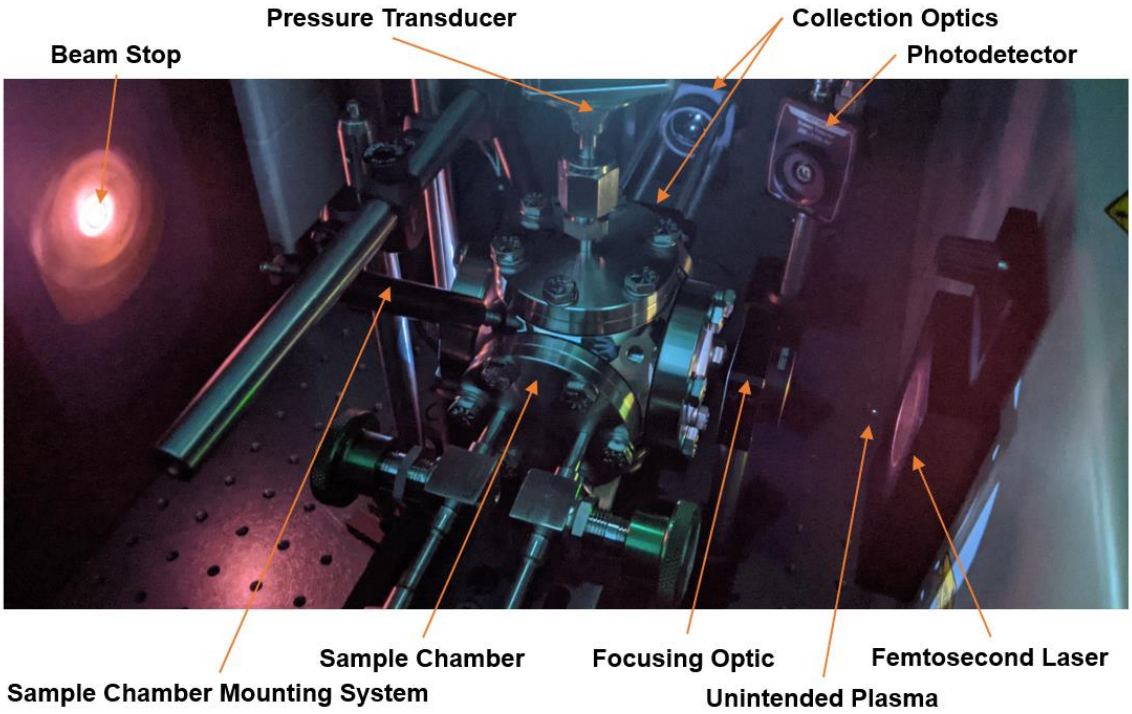


Figure 3.7. fs-LIBS High Power Equipment Configuration

The collection optics are also partially visible in Fig. 3.7. The lens that focuses the collected light into the reflective collimator is visible at the far end of the 4-bar cage system that maintains the collection optics alignment. The detector used to provide plasma emission timing information to the oscilloscope is visible to the right of the 4-bar cage system. Also visible in Fig. 3.7 is an unintended plasma just outside the laser's emission port. This is believed to be the result of reflection from the focusing lens. Adjustment of the focusing lens could alter this tiny plasma but could not totally eliminate it.

Delay and Gate Width Research Method

The goal of identifying optimum delay and gate width combinations to yield the most accurate fs-LIBS assay measurements required developing a series of delay and gate width combinations that cover the range of anticipated valuable plasma emissions, and which could be applied to each sample chamber and across multiple data collection campaigns.

The intention was to identify delay and gate width combinations that effectively avoid the Stark effects of line broadening and line shift as recommended by Song et al., in addition to the more common parameters of intensity and signal-to-noise ratio (SNR) which need optimization [67]. The delays discussed in this research are the delays after the trigger signal from the laser.

One "Survey" series of delay and gate width combinations progressively increased the step size of the delay by an additional 25 ns for each successive delay and gate width combination while the increase to the gate width itself remained at a fixed 25 ns increase for each of the delay and gate width combinations. This approach is targeted at obtaining a survey of the plasma life with a relatively small number of steps. These delay and gate width combinations are shown in Table 3.2 and are reported relative to the laser trigger signal.

A second "Investigation" series of delay and gate width combinations was employed to provide a closer investigation of the temporal nature of the plasma emissions by reducing the increase of the delay to be fixed at 5 ns for each successive delay and gate width combination. The plasma emission intensity was expected to rapidly decay following the laser impulse. However, after the first transition, the gate width in this series increased by a fixed 5 ns for each successive delay and gate width combination to provide a detailed look at the temporal nature of the emissions. Note that although the delay and gate width are increasing by the same rate in the investigation, the gate width starts with a 10 ns increase from the first delay and gate width combination and the delay is only indexed by 5 ns. Following the first transition they are increased equally.

Table 3.2. Delays and Gate Width Settings Used for Survey Data Collection

Survey Delays (ns)	Survey Gate Widths (ns)
83	108
108	133
158	158
233	183
333	208
458	233
608	258
783	283
983	308
1208	333
1458	358
1733	383
2033	408
2358	433
2708	458
3083	483

Given that the detector delay times must be large enough that almost all of the Stark effect subsides, the thinking in this series of delay and gate widths is that any subsequent emission that can be captured will be beneficial to the assay measurement and largely free of Stark effects [27]. Therefore, the gate widths grow at an increasing rate to capture sufficient plasma emission for an assay measurement. The resulting delay and gate width combinations are shown in Table 3.3.

A third “Kinetic Series” set of delay and gate width combinations, shown in Table 3.4, was employed to eliminate the overlap that existed between successive delay and gate width combinations present in the both the survey and investigation approaches. Such overlaps might seem necessary in an attempt to keep collection time minimized. However, the overlap complicated the analysis of where in the plasma life cycle the emissions are most valuable for making an assay determination. To address this shortcoming, the kinetic series of delay and gate width combinations was employed.

The delay and gate width combinations in the kinetic series fit together end-to-end to create a picture of the plasma emissions from initiation until the emission has largely disappeared. This approach resulted in straightforward evaluation of the value of each time period in the plasma life cycle. The drawback to this approach was that the collection times were lengthened to achieve the desired signal strength. As a result, the exposure times required during the kinetic series data collections in the high-power laser configuration were 15 to 30 times longer than the exposure times required for the survey and investigation series in the high-power laser configuration.

Exposure

Two different approaches were used to establish the appropriate exposure times. In the first rounds of testing through the survey and investigation data collection campaigns, the exposures were selected to attempt to place the peak of the 424.1664 nm and/or the 424.6260 nm line intensities between 40,000 and 50,000 counts on the fully vertically binned (FVB) format on the ICCD software. These FVB spectra provided by the software were not analyzed for assay. Their only purpose was to provide a consistent means of setting the exposure for a roughly consistent signal strength from one collection to another. This approach typically produced 424.4372 nm and/or 424.4122 nm line intensities that were 3 to 4 times the level of the combined detector dark offset and plasma continuum which appear as a noise floor out of which the spectrum rises. This method took a conservative approach to insuring the ICCD’s range was not exceeded by focusing on the most intense spectral emissions.

Table 3.3. Delays and Gate Width Settings Used for Investigation Data Collection

Investigation Delays (ns)	Investigation Gate Widths (ns)
83	88
88	98
98	113
113	133
133	158
158	188
188	223
223	263
263	308
308	358
358	413
413	473
473	538
538	608
608	683
683	763
763	848
848	938
938	1033
1033	1133
1133	1238
1238	1348
1348	1463
1463	1583
1583	1708

Table 3.4. Delays and Gate Widths Settings Used for Kinetic Series Data Collection

Kinetic Series Delays (ns)	Kinetic Series Gate Widths (ns)
70	25
95	50
145	75
220	100
320	125
445	150
595	175
770	200
970	225
1195	250
1445	275
1720	300
2020	325

The second method to establish the exposure time was used when setting the ICCD software to automatically collect kinetic series delay and gate width combinations. In this approach, the exposure time was set at a very low level and the kinetic series frame with the highest emission intensity was identified. The collection parameters of this hottest frame were then set into the ICCD software as the delay and gate width while the exposure was increased with a goal of identifying an exposure that would result in the hottest pixel on the collected image reaching 30,000 counts. Such counts would make good use of the effective measuring range of the ICCD and result in a strong signal for evaluation.

Partial pressure of gas being analyzed

The pressure of the UF_6 atmosphere inside the sample chamber has an impact on the measurement. As the pressure increases, the plasma appears more intense and, conversely, as the pressure decreases the plasma intensity is diminished. The expectation was that the lower pressures would produce a spectrum with fewer interfering peaks of minimal isotopic value based on the findings of Chan et. al [27]. The spectral congestion reported by Chan at higher UF_6 partial pressures must be balanced against the need for more intense plasma emission in the case of femtosecond laser produced plasmas in this research. The pressure inside the sample chamber is monitored during the testing via a MKS data logger which allows connection of the 902B pressure transducer to the USB port of a computer.

Precision calibration of collected spectra for assay measurement

This research uses a calibration approach that was specifically developed to tailor the accuracy of the wavelength calibration around the most prominent peaks involved with the assay measurement for every spectrum collected individually. This approach is taken to attempt to minimize the potential impact of Stark shift which can alter the wavelength center based on where in the plasma life the spectra are collected [27]. This function will be called simply the calibration function. The calibration approach is implemented as a MATLAB function which produces a wavelength calibrated output typically between 163 and 170 pixels or data points wide which is wavelength calibrated from the 1024 by 1024 image text file output from the Andor Solis software.

Initially the calibration function removes the top and bottom of the image leaving only pixel rows from 200 up to 800. The other rows fall outside the area illuminated by the 19 stacked fibers of the fiber optic cable. The calibration function totals the energy collected by every pixel remaining in each column. This process is called fully vertically binning the data in a similar fashion to the FVB

output from the ICCD software. The result is a spectrum of energies binned by wavelength but the bins only have numbers associated with the pixel column identification at this point rather than a wavelength to identify them.

The wavelength calibration approach is based on the location of 3 prominent peaks in each spectrum collected. The 424.1664 nm and the 424.6260 nm peaks are easily visually detectable and are used for calibration in every spectrum collected in the 424.4 nm region for this research. These peaks are just beyond the spectral window of interest between 424.3 and 424.5 nm. The 3rd peak used for calibration is 424.4372 nm for all samples below 50% ^{235}U. The 61.74% ^{235}U sample was calibrated using a 424.4122 nm peak as the 3rd calibration point since it was the more prominent peak in this sample.

In an actual measurement where no information about the expected enrichment is known, there is no reason that the 424.4372 peak could not be used for calibration for every sample until enrichments approach 100% ^{235}U. The 61.74% sample was evaluated using the 424.4372 nm peak and there was no significant difference observed in the calibration or the resulting assay measurements.

Once three distinct pixel ranges are established inside which the 3 calibration peaks are expected to occur, a peak fitting routine is used to fit Lorentzian functions to the spectral peak shapes in the pixel ranges. The peak fitting is executed by an additional MATLAB script called *PeakFit* available on the MATLAB file exchange [111]. The *PeakFit* script was adapted for the fs-LIBS calibration application in the following ways[118]:

- Heavily trimmed code to focus on Lorentzian fits
- Elimination of the code's ability to place a Lorentzian outside the range of data which existed to create baseline shifts
- Changes in the code so it now takes any Lorentzian that falls outside the range of data and puts it back in the center and gives it a minimal value
- Increased number of iterations in the function minimization routine to make sure that there is high repeatability
- Altered approach to use more efficient and adjustable **fmincon** versus **fminsearch** in the original *Peakfit*
- Added availability of a full-width-half-max output for each Lorentzian used in the fitting

The MATLAB function sorts the resulting Lorentzians by their amplitude and the most prominent is determined to be the true location of the center of the spectral emission. This determined true center would rarely be in the exact center of a pixel, which is why this process of calibration is important when making assay

determinations based on isotopic shifts which may only be a few picometers wide. The calibration function assigns peak wavelengths to these determined true centers of the peak. The MATLAB function **polyfit** is then used to fit a polynomial to the three resulting wavelength calibrated datapoints. Subsequently the MATLAB function **polyval** evaluates the polynomial at each pixel column to reassign the energy reporting by wavelength as opposed to pixel column.

The result of this calibration approach has offered the opportunity to constrain the optimization of the post-calibration shift variable λ_s in the multivariate nonlinear spectral fitting algorithm much more tightly than was reported in the prior publications [67]. The wider range of λ_s initially used in the research allowed the aliasing of peaks resulting in erroneous assay measurement.

The calibration of each spectrum to the most prominent peak used in the assay measurement and the constrained post-calibration shift variable λ_s in the multivariate nonlinear spectral fitting algorithm are key to how the calibration function is used to avoid the impact of Stark shift. The expectation is that if Stark shift affects the location of the most important peak for assay measurement, then the wavelength calibration will be skewed. This is visually apparent in graphs of the calibration function which can be scanned for spectra to cull. Additionally, by constraining the post-calibration shift variable λ_s in the multivariate nonlinear spectral fitting algorithm, the Stark-shift-affected spectra cannot be effectively fitted by the algorithm.

Description of the Fitting Algorithm Used for Establishing Baseline of fs-LIBS with MVNLSF

A slight adaptation of the published fitting algorithm proposed by Song et. al was selected as the starting point to baseline the performance of the fs-LIBS system [67]. The adaption involves the use of the $1/\pi$ term so that the Full Width Half Max is $2 * \omega$. The adapted fitting algorithm for the experimentally collected spectra takes the general form shown in (10).

$$I^{exp}(\lambda) = \sum_{\forall i}\left\{\frac{R\,A_i\,(k_i\,\omega_i)}{\left[\pi\left(\lambda-\lambda_s-\lambda^0_{235,i}\right)^2+(k_i\omega_i)^2\right]}+\frac{(1-R)\,A_i\,\omega_i}{\left[\pi\left(\lambda-\lambda_s-\lambda^0_{238,i}\right)^2+\omega_i{}^2\right]}\right\}+c_0+\varepsilon(\lambda) \qquad (10)$$

In (10), $I^{exp}(\lambda)$ represents the spectrum collected by the fs-LIBS system. The quantities R and $(1-R)$ are the ^{235}U atom percent present and the ^{238}U atom percent present respectively. For each *i*, A_i represents the area of the spectral peak *i* and the ω_i is its line width. The λ in (10) is the measurement wavelength and λ_s is a correction factor intended to allow some slight shifting between the

calibrated and measurement wavelengths. The c_0 is a constant which represents the plasma continuum background and the $\varepsilon(\lambda)$ is the residual of the fitting which is minimized by the MATLAB implementation of this algorithm. The k_i is a line width correction factor which was empirically determined by Song et. al based on theoretical line width ratios [67]. The line width correction factor proposed by Song et. al is shown in (11).

$$k = 1.00066 + 0.04168e^{\frac{-\omega_{238}\ at\ 424.437\ nm}{0.00717}} + 0.78404e^{\frac{-\omega_{238}\ at\ 424.437\ nm}{0.00170}} \quad (11)$$

The approach initially relies on the 12 isotopic shifts identified by Song et. al in Table 2.1 to evaluate the assay prediction ability of the fs-LIBS system [67]. Therefore, fitting algorithm initially has 16 variables which are optimized to minimize the fitting error, $\varepsilon(\lambda)$, of the spectra collected by the fs-LIBS system. The 12 parameters are: ω_i, A_i (initially 1 through 12 for the 12 isotopic pairs identified by Song et. al), λ_s, c_0, and R.

Fitting window data range (*dr*)

One goal that arose during this research was to explore the potential to make enrichment measurements without the benefit of an experienced spectroscopist establishing fitting windows tailored for each isotopic pair under evaluation. To that end the effect of the spectral fitting window is varied by adjusting a parameter, *dr*, as shown in Fig. 3.8. The *dr* is not equal to the range over which each isotopic pair will be optimized. The *dr* value is the distance in nanometers beyond the center of the ^{235}U and ^{238}U emission lines that make up the isotopic pair over which the fit will be attempted. It was also hypothesized that this approach of focusing on small fitting windows around the isotopic pairs might suppress the impact of spectral clutter in the resulting fit over the entire spectral fitting window of 424.3 to 424.5 nm. The *dr* fitting approach should also be considered for use when a practitioner wishes to evaluate two spectral regions separated widely in the ICCD's field of view to suppress the influence of spectral data between their regions of interest.

Fig. 3.8 illustrates how the separation of the isotopic pair in combination with the *dr* value sets the fitting window for each isotopic pair. The left-most spectra show the respective *dr* ranges for is isotopic pair number 1 from Table 2.1. The upper end of the fitting range for the 0.287% spectrum applied to isotopic pair number 1 and with *dr* = 0.043 yields 424.4802 nm. This is the addition of 424.4372 nm and the *dr* value. Following the same approach yields for the 18.525% spectrum a lower fitting range bound of 424.4362 nm associated with isotopic pair number 1 from Table 2.1. This is the subtraction of the *dr* value, 0.048 nm in this case, from 424.4122 nm. The spectra in the right-hand column of Fig. 3.8 shows the fitting window for pair 8 from Table 2.1.

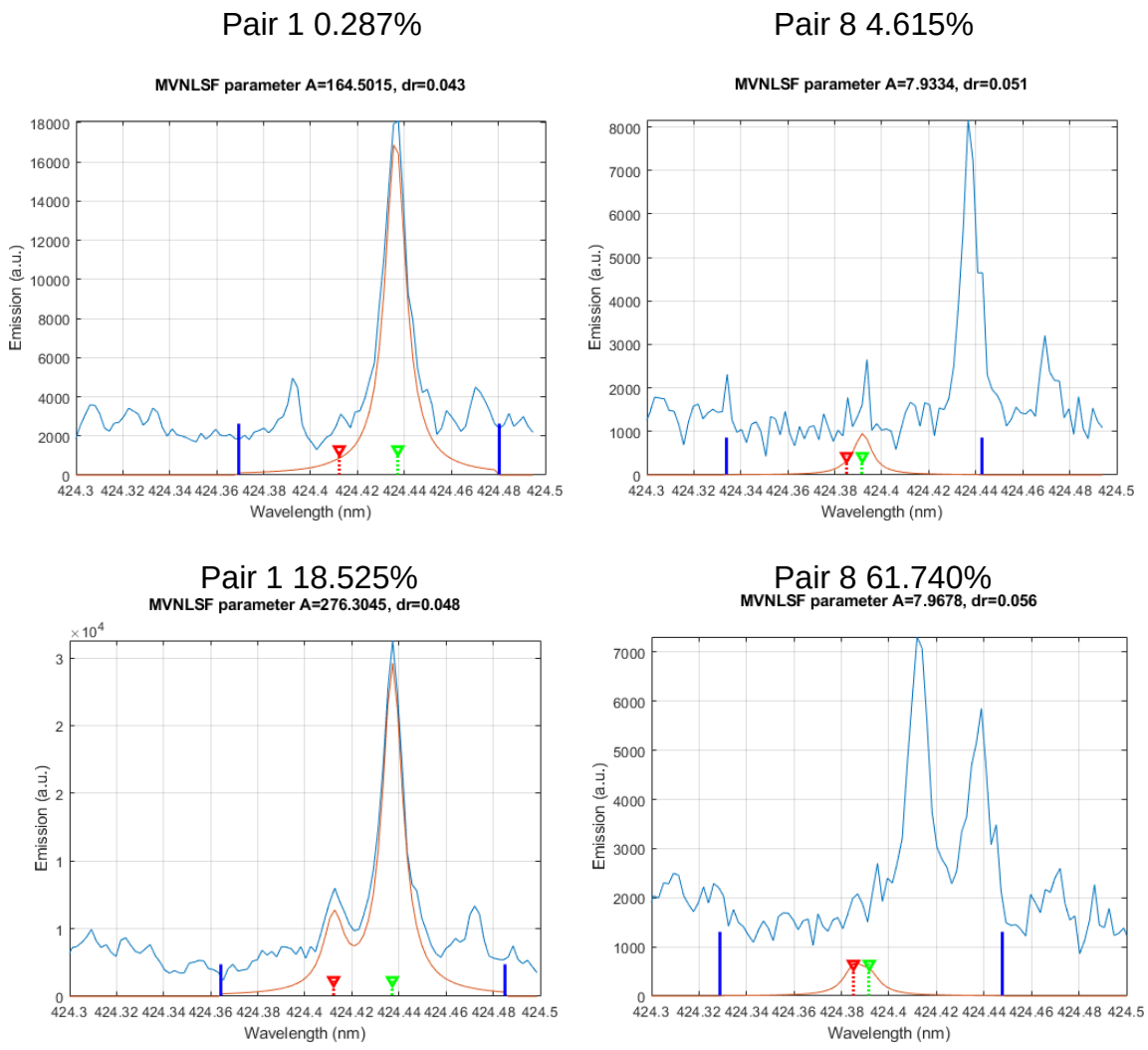


Figure 3.8. Fitting window *dr* Pair 1 and Pair 8

Song et al. advise that “the spectral range in which spectral fitting is applied should be accordingly shrunk to a region dominated only by the two isotopic peaks” [67]. This statement referred to the fitting of a single isotopic pair rather than the multiple spectral peak fitting algorithm that the authors propose later in the article, but in the fs-LIBS research the spectra being captured in the low-power low-pressure configuration exhibited a poor SNR. The limitation of spectral fitting window to the areas immediately surrounding each isotopic pair seemed to hold promise for reducing the impact of the poor SNR. It should be noted for large values of *dr* the fitting algorithm is applied to the entire wavelength range under investigation because of the closeness of the 12 isotopic pairs used in the MVNLSF algorithm.

Chapter Four

Results

The primary goal of this research is to complete a fs-LIBS assay measurement on multiple samples of UF_6 in a variety of test conditions and report the accuracy achieved. This goal was accomplished and the results are reported below. To my knowledge, this work is the first publication of fs-LIBS spectra for these enrichment levels of UF_6. Included in Fig. 4.1 are spectra from each of the five samples centered on the 424.4 nm wavelength to allow near central evaluation of the prominent 424.4372 nm and 424.4122 nm isotopic pair associated with ^{238}U and ^{235}U respectively.

The 38.103% sample chamber will be discussed separately from the four sets of results shown in in the figures and tables associated with the three primary testing configurations.

Spectral Fitting Figures

Throughout the remainder of this dissertation there are figures which present information densely and warrant explanation so that it need not be repeated for each figure occurrence. Above the spectral fitting figures, the MVNLSF-calculated assay is reported as a decimal value and the *dr* is reported. In the spectral fitting figures, the uppermost blue solid lines are the captured spectra from the ICCD. Each has been captured as an image and clipped to eliminate areas not receiving light from the spectrometer. The uppermost solid blue lines represent the full vertical binning of the captured image. These captured spectra have also been wavelength calibrated as described in Chapter 3.

The multicolored peaks shown below the solid blue line are produced by separate pairs of Lorentzian peaks. The amplitude of the Lorentzian peaks is optimized and reported by the fitting algorithm. The fitting algorithm is described in Chapter 3. Up to 12 individual Lorentzian pairs may appear below the solid blue line. These Lorentzian pairs correspond to the isotopic pairs identified by Song et. al [67]. Note that typically fewer than all 12 of the isotopic pairs will contribute to the final resulting fit.

The spectral fitting figures in the section titled *Additional Isotopic Pairs for fs-LIBS* include two additional isotopic pairs as potential contributors to the optimum resulting fitment of the spectral data. The contribution of the individual Lorentzian pairs appears below the spectral data and the fitted result because they have not yet had the c_0 constant, which represents the plasma continuum background, added to them.

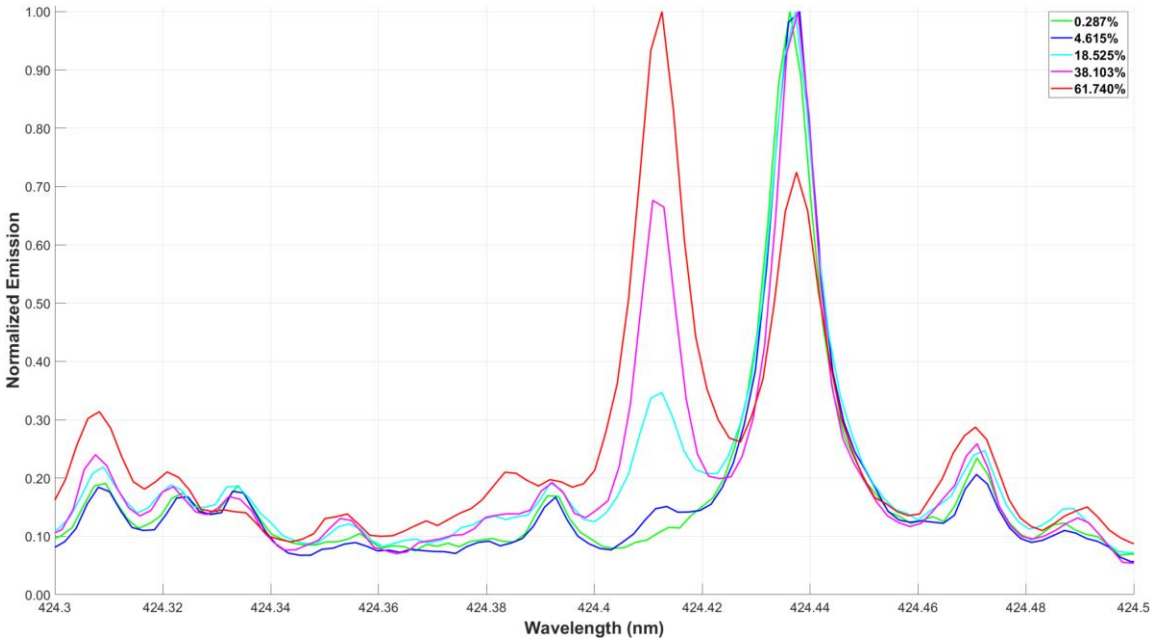


Figure 4.1. fs-LIBS spectra from five UF_6 samples collected with a delay of 848 ns and gate width of 938 ns in a sampling configuration with high-pressures of approximately 60 Torr and laser power of about 6 Watts creating the plasma.

Finally, the resulting fitting is shown as a red dotted line tracking the solid blue line closely. This color scheme applies to all the spectral fitting figures in this chapter. The spectral fitting figures report in unit of emission which are arbitrary units (a.u.). These units are affected by the ICCD setting and the post processing, but are traceable back to the number of electrons reaching the pixels on the ICCD chip.

Testing Configurations

The measurement campaign to capture data for this research includes three distinct sampling conditions. The sampling condition combined with the delay and gate width series are a testing configuration. The first sampling condition involved the sample chamber being chilled to the greatest extent possible by the thermoelectric cooler in combination with reduced laser energy focused into the sample chamber. This condition is abbreviated LPLP for Low-Power Low-Pressure.

The laser power reduction is accomplished by the losses in the three femtosecond rated mirrors serving as steering optics to direct the laser beam to the chamber. The laser power for each testing configuration is shown in Table 4.1. The thermoelectric cooling reduces the pressure inside the sample chamber. The pressure data was logged using a computer connected to the pressure transducer on the sample chambers. The average pressure for the samples during the data collection is included in Table 4.2.

The second sampling condition retains the thermoelectric cooler driving the sample chamber internal pressure as low as possible. The sample chamber and cooler have been relocated to be directly in line with the emission port on the laser casing. This closely coupled location avoids the use of steering optics and results in the maximum laser energy being delivered to the focusing lens to create a more intense plasma within the sample chamber. This condition is abbreviated HPLP for High-Power Low-Pressure.

The third and final sampling condition retains the HPLP laser configuration but is performed with the thermoelectric cooler not in operation. The sample chamber pressure is at its maximum in this configuration. It should be noted that this configuration most closely matches the conditions postulated by Glaser for enrichment facilities to operate [119]. This sampling condition is abbreviated HPHP for High-Power High-Pressure. This sampling condition was used for an additional testing configuration beyond the Survey and Investigation, called the Kinetic Series, which will be discussed separately.

Table 4.1. Laser Power at the Focusing Lens in Watts for the Sampling Conditions

ORNL Reported U-235 Enrichment	**0.287%**	**4.615%**	**18.525%**	**38.103%**	**61.740%**
Survey 1 LPLP	2.6	0.0	2.7	2.6	2.6
Survey 2 LPLP	2.4	0.0	2.5		2.5
Survey 1 HPLP	6.3	6.3	6.4		6.4
Survey 2 HPLP	6.3	6.3	6.3		6.3
Survey 1 HPHP	6.5	6.3	6.3	6.3	6.3
Survey 2 HPHP	6.3	6.3	6.3	6.3	6.3
Investigation 1 LPLP	2.2	0.0	2.4	1.9	2.7
Investigation 2 LPLP	2.5	2.5	2.5		2.4
Investigation 1 HPLP	6.3	6.3	6.4		6.4
Investigation 2 HPLP	6.3	6.3	6.3		6.3
Investigation 1 HPHP	6.5	6.3	6.3	6.4	6.3
Investigation 2 HPHP	6.3	6.3	6.3	6.3	6.3

Table 4.2. Average Pressure in Torr for the Sampling Conditions

ORNL Reported U-235 Enrichment	**0.287%**	**4.615%**	**18.525%**	**38.103%**	**61.740%**
Survey 1 LPLP	9.0	10.6	5.6	15.2	6.4
Survey 2 LPLP	9.7	11.2	5.1		6.7
Survey 1 HPLP	9.2	10.8	5.6		5.9
Survey 2 HPLP	9.8	11.1	5.3		6.1
Survey 1 HPHP	55.9	54.2	52.0	58.3	55.8
Survey 2 HPHP	55.6	54.2	52.0	57.7	55.8
Investigation 1 LPLP	9.7	10.7	10.7	23.9	6.4
Investigation 2 LPLP	9.7	11.4	11.3		6.8
Investigation 1 HPLP	9.2	10.8	10.7		5.9
Investigation 2 HPLP	9.8	10.9	10.8		6.4
Investigation 1 HPHP	55.9	54.2	52.0	58.3	55.8
Investigation 2 HPHP	55.6	54.2	52.0	57.7	55.8

Optimization of Collection Parameters

Gate Delay and Gate Width

The goal of determining optimum gate width and gate delay settings that yield the most accurate measurement of ^{235}U enrichment required that a baseline process for conducting the spectral analysis be established. The baseline process for this research was based on the MVNLSF approach published by Song et al. [67]. It is the MVNLSF- reported assays that will be used to evaluate each delay and gate width setting.

The results in each of the pressure and power regimes is the average assay calculated using the MVNLSF approach for *dr*=0.030 to *dr*=0.1. It was noted that the predicted assay largely stabilizes for *dr* values in this range. This is not surprising because beyond *dr*=0.010 the fitting range covers essentially the entire wavelength range of interest as shown in the Table 4.3. Further, as the *dr* value grows the contribution of the Lorentzian pair contributes to a wider region within the overall fitting window.

Low-Power Low-Pressure (LPLP) Surveys

The LPLP Survey testing configuration was anticipated to minimize spectral clutter and allow the primary peaks needed for the MVNLSF assay measurement to become more pronounced from the plasma continuum [80]. This series of delay and gate width combinations, labeled as a survey in Table 3.2, progressively increased the step size of the delay by an additional 25 ns (e.g., 25, 50, 75, …) for each successive delay and gate width combination while the increase to the gate width itself remained at a fixed 25 ns increase for each of the succeeding delay and gate width combinations. However, the femtosecond plasma is smaller and less persistent than the more common nanosecond-laser induced plasmas [72]. This weak plasma created challenges for collecting sufficient plasma emission for MVNLSF analyses.

Fig. 4.2 shows selected spectra from each of the LPLP Surveys performed on four sample chambers containing 61.740%, 18.525%, 4.615%, and 0.287% material. The spectra were collected with the delay and gate width settings shown in Table 4.4 for the corresponding assay. The delay and gate widths in Table 4.4 are those which yielded the most accurate average assay measurements from the five spectra collected at each delay and gate width combination. The spectra included in Fig. 4.2 were selected for the closeness of their MVNLSF-calculated assay to the actual assay of the sample. The explanation of the information provided in the spectral fitting figures in Fig. 4.2 is as described earlier in Chapter 4.

Table 4.3. Distance Between Isotopic Pairs and the Next Higher Isotopic Pair and *dr* Needed to Span Distance to the Next Higher Isotopic Pair

Isotopic Pair #	Lower Wavelength (nm)	Upper Wavelength (nm)	Separation (nm)	*dr* to span (nm)
2	424.307	424.309	0.014	0.007
3	424.322	424.324	-0.011	-0.006
4	424.313	424.334	0.020	0.010
5	424.355	424.355	0.016	0.008
6	424.371	424.378	0.004	0.002
7	424.382	424.391	-0.006	-0.003
8	424.385	424.392	0.020	0.010
1	424.412	424.437	0.004	0.002
9	424.441	424.444	0.021	0.010
10	424.465	424.470	-0.001	-0.001
11	424.468	424.471	0.017	0.009
12	N/A	N/A	N/A	N/A

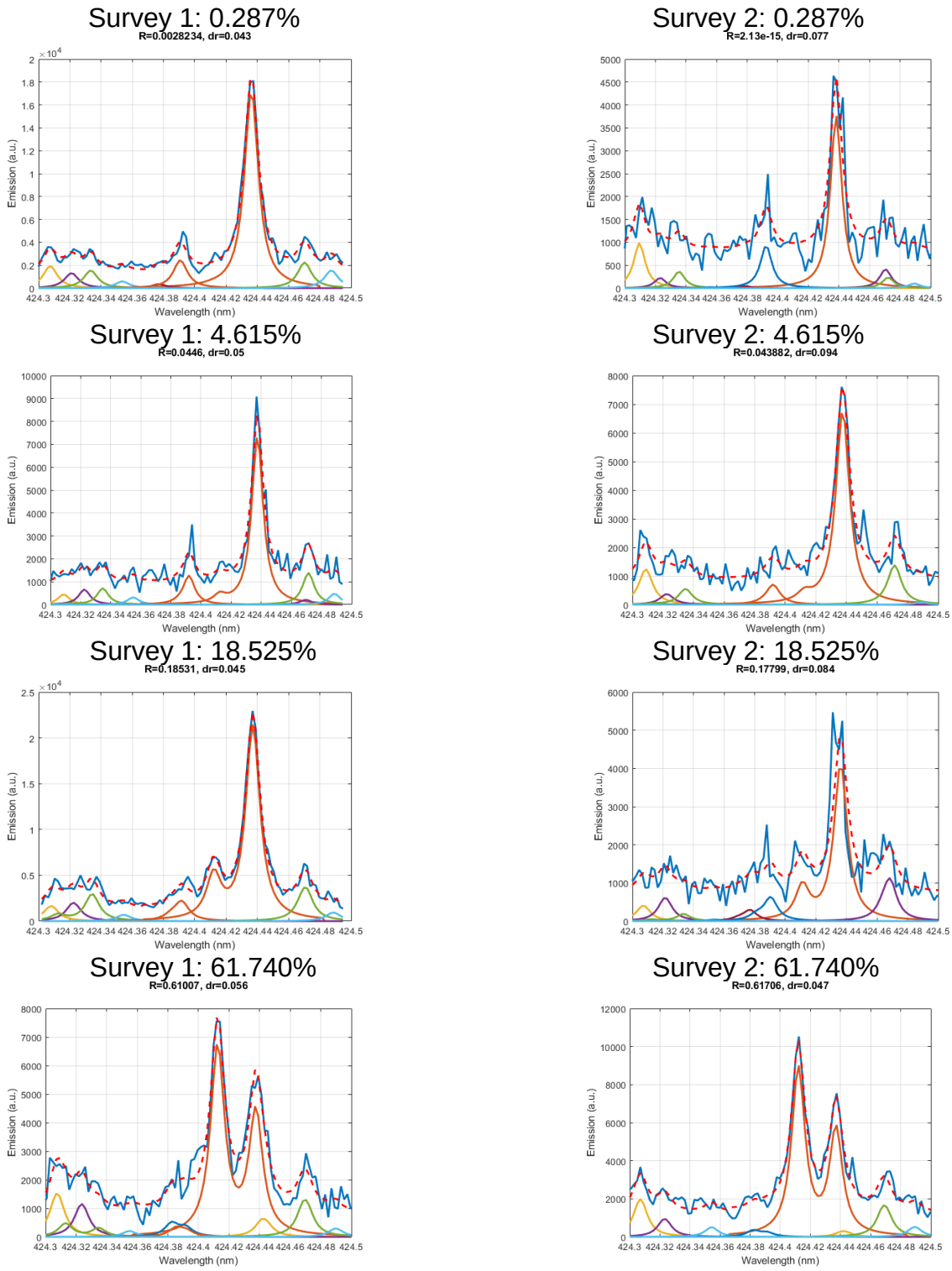


Figure 4.2. LPLP Survey Fits

The difficulty collecting sufficient plasma emission for the analysis is evident in Fig. 4.2. Note that the spectra with the lower emission energy, has a less accurate assay calculated by MVNLSF than its higher energy neighbor in each case shown in Fig. 4.2. Also, note that the presence of potential self-absorption to the point of self-reversal is evident in Survey 2 of both the 0.287% and 18.525% samples as well as Survey 1 of the 61.740% sample. The indicator is the bifurcated peak at the top of the otherwise normally shaped emission peak.

The configuration for low power and low pressure yields about 2.5 W reaching the focusing lens and the specific values for these sampling conditions are shown in Table 4.1. With the thermoelectric cooler energized, the average pressures for the samples range from a high of 10.6 Torr for the 4.615% sample to a low of 5.6 Torr for the 18.525% sample as can be seen in Table 4.2.

Note that in both of the 0.287% spectra, the second 18.525%, and the first 61.740% spectra there are noticeable deformations to the 424.437 nm emission. This is likely either a result of poor SNR associated with the weakened plasma or self-absorption and in the extreme cases where the peak has been bifurcated, potentially self-reversal [120]. The SNR for the LPLP ranged from 25:1 to as low as 5:1 based on the emission intensity of the 424.4372 nm and 424.4122 nm isotopic pair versus the calculated noise from the detector.

The results in Table 4.4 were generated by evaluating only the first five of the potential survey delay and gate width combinations listed in Table 3.2 because the low power configuration resulted in a weak plasma that did not persist for long enough to capture data at the later delay and gate width combinations. The fifth delay and gate width setting required exposures of 120 seconds. The ICCD is integrating the emission from 120,000 laser-induced plasmas in these lengthy exposures.

Table 4.4 lists the delay and gate width combinations that produced the closest average enrichment measurement to the actual enrichment of the sample. The MVNLSF-calculated enrichment is the average of the MVNLSF-calculated assay from dr=0.030 to dr=0.1. Recall that this is the region where the assay values were observed to have stabilized. This is a key distinction from the spectra selected for Fig. 4.2 where a specific spectrum was selected for its closeness to the actual sample enrichment.

The MVNLSF-calculated enrichments are the average of the MVNLSF-calculated enrichment for each of the five spectra captured at the delay and gate width combinations listed. The error from the ORNL reported enrichment is calculated so that the result will be positive for an overestimate of the enrichment and negative for an underestimate of the enrichment versus the sample’s actual ORNL-reported assay.

Table 4.4. LPLP Survey Results

ORNL Reported Enrichment	**0.287%**		**4.615%**		**18.525%**		**61.740%**	
Delay and Gate Width (ns)	158-158	233-183	233-183	158-158	158-158	233-183	158-158	158-158
MVNLSF Calculated Enrichment	0.92%	0.00%	4.05%	5.61%	18.2%	18.7%	63.6%	65.7%
Error from ORNL Reported Enrichment	0.63%	-0.3%	-0.6%	1.00%	-0.3%	0.18%	1.82%	4.00%
Standard Deviation	1.17%	0.00%	2.06%	4.86%	1.01%	3.97%	3.64%	3.39%
Relative Standard Deviation	128%	208%	50.9%	86.6%	5.5%	21.2%	5.6%	5.2%
RMSE	1.23%	0.29%	2.14%	4.46%	0.96%	3.56%	4.90%	4.83%
Mean Absolute Error	0.88%	0.29%	1.86%	3.40%	0.67%	3.25%	4.10%	3.82%

The standard deviation (SD), the relative standard deviation (RSD), the Root Mean Square Error (RMSE), and the Mean Absolute Error (MAE) are all calculated as averages of the MVNLSF results from *dr*=0.030 to *dr*=0.1 calculated for each of the five spectra captured at the delay and gate width combination listed in the table. The relative standard deviation is large, especially for the 0.287% sample, because the RSD is the standard deviation divided by the stabilized assay average from *dr*=0.03 to *dr*=0.1.

This data was important to capture because it was expected to provide an opportunity for minimal spectral clutter, but any benefits are outweighed by the difficulty obtaining sufficient SNR.

High Power Low Pressure (HPLP) Surveys

The HPLP Survey testing configuration results in approximately 6 W of laser power reaching the focusing lens with the thermoelectric cooler operating to produce as low a pressure as possible within the sample chambers. The laser power delivered to the sample has increased significantly over the LPLP configuration and the specific values reaching the focusing lens are shown in Table 4.1.

These surveys were performed one month after the LPLP surveys. The pressure that the thermoelectric cooler is able to drop the sample chamber is within 0.6 Torr of the LPLP testing. The average pressure of the 61.740% sample was 0.5 to 0.6 Torr lower than during the LPLP testing. The average pressures are reported in Table 4.2, but the conclusion is that the sample chamber integrity is still preventing much in-leakage and subsequent reaction which would increase the pressure in the chambers.

The SNR has clearly been improved by the increase in laser energy reaching the focusing lens in the HPLP sampling condition. The spectra shown in Fig. 4.3 were selected based on the closeness of their MVNLSF-calculated assay to the actual assay. The SNR for the HPLP ranged from 42:1 to as low as 17:1 based on the emission intensity of the 424.4372 nm and 424.4122 nm isotopic pair versus the calculated noise from the detector.

Table 4.5 identifies the delay and gate width combination that provided the most accurate average assay calculated using MVNLSF to evaluate the HPLP Survey spectra. The MVNLSF-calculated enrichment, SD, RSD, RMSE, and MAE are the average of the MVNLSF-calculated assay from *dr*=0.030 to *dr*=0.1. Recall that this is the region where the assay values were observed to have stabilized.

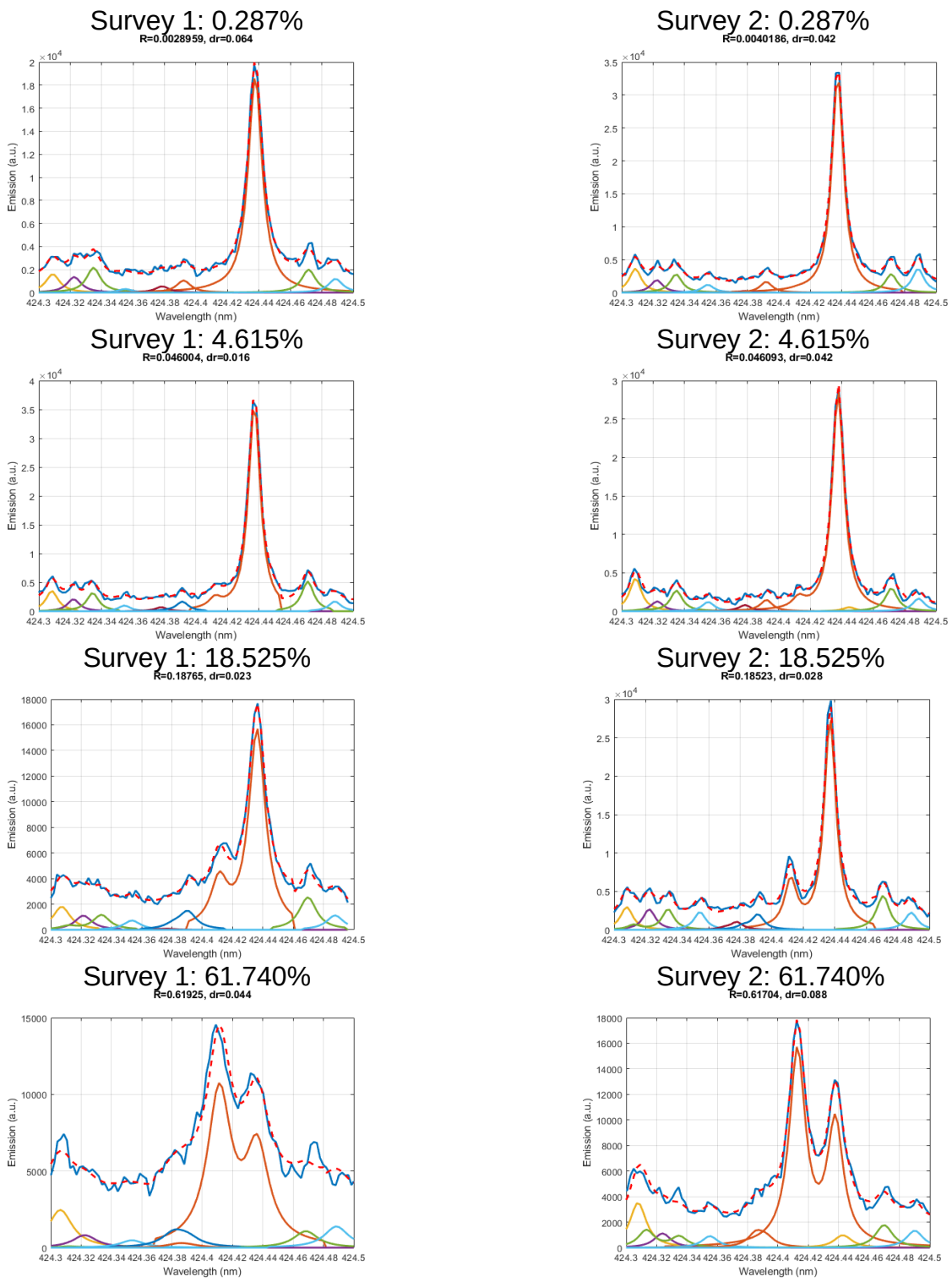


Figure 4.3. HPLP Survey Fits

Table 4.5. HPLP Survey Results

ORNL Report. Enrich.	**0.287%**		**4.615%**		**18.525%**		**61.740%**	
Delay and Gate Width (ns)	233-183	333-208	333-208	333-208	158-158	333-208	108-133	158-158
MVNLSF Calc'd Enrich.	0.23%	0.25%	5.20%	4.21%	18.8%	19.2%	63.6%	64.1%
Error from ORNL Report. Enrich.	-0.05 %	-0.04 %	0.59 %	-0.41 %	0.25 %	0.71 %	1.91 %	2.37 %
Standard Dev.	0.34%	0.30%	0.22%	0.67%	1.21%	2.15%	1.30%	2.27%
Relative Standard Dev.	148%	122%	4.1%	15.8%	6.4%	11.2%	2.0%	3.5%
RMSE	0.32%	0.27%	0.62%	0.74%	1.11%	2.05%	2.25%	3.12%
Mean Absolute Error	0.28%	0.26%	0.59%	0.53%	1.07%	1.63%	1.97%	2.41%

The delays and gate widths that produced the most accurate assay measurement are slightly later on average than those observed in the LPLP Survey testing configuration. The shift in the delay and gate width is unsurprising given the larger incoming laser power, but the slight improvement in the statistics of the spectral averages is a noted difference from nanosecond LIBS of UF_6 where at reduced pressure and reduced laser power, fewer peaks are present and the primary peaks for calculation of assay become more pronounced [27, 80]. In this case with fs-LIBS the improvement in the SNR is the driving factor improving the standard deviations reported. The accuracy of the assay predictions has not improved significantly from the LPLP survey.

High-Power High-Pressure (HPHP) Survey

The HPHP Survey testing configuration mimics the HPLP sampling conditions except that the thermoelectric cooler is not energized so the sample chambers are tested at room temperature where their pressures are just below 60 Torr. Fig. 4.4 shows the spectral fitting of the HPHP spectra which most closely matched the actual assay of the sample. The SNR remained similar to that of the HPLP Surveys, producing a maximum of about 40:1 based on the emission intensity of the 424.4372 nm and 424.4122 nm isotopic pair versus the calculated noise from the detector.

The delay and gate width steps were extended to capture as much of the plasma emissions as possible. Table 4.6 illustrates a significant trend toward delay and gate widths later in the time following the laser trigger signal. Table 4.6 also shows HPHP survey standard deviations which are slightly worse than the HPLP survey data.

Also, of note in Table 4.6 is that the HPHP testing configuration is the first in which the average of 61.740% sample's assay predictions is less than the actual enrichment. This is in agreement with the expectation of biased reporting due to self-absorption of the more prevalent isotope, creating a bias toward overestimation of the less prevalent isotope [27, 67]. The expected biases do not occur as consistently as reported in other UF6 isotopic LIBS research potentially because the femtosecond-induced plasma has a steeper density and temperature gradient than nanosecond-induced plasmas offering fewer self-absorption opportunities in the cold outer layers of the plasma [27, 67, 121].

Both of the 61.740% sample's delay and gate widths which produced this under reporting of the assay occurred quite late in the plasma life. The same is true of the second 18.525% survey where the late delay and gate width under reported the assay. However, the first 18.525% survey produced the most accurate measurement much earlier in the plasma life and overreported the enrichment.

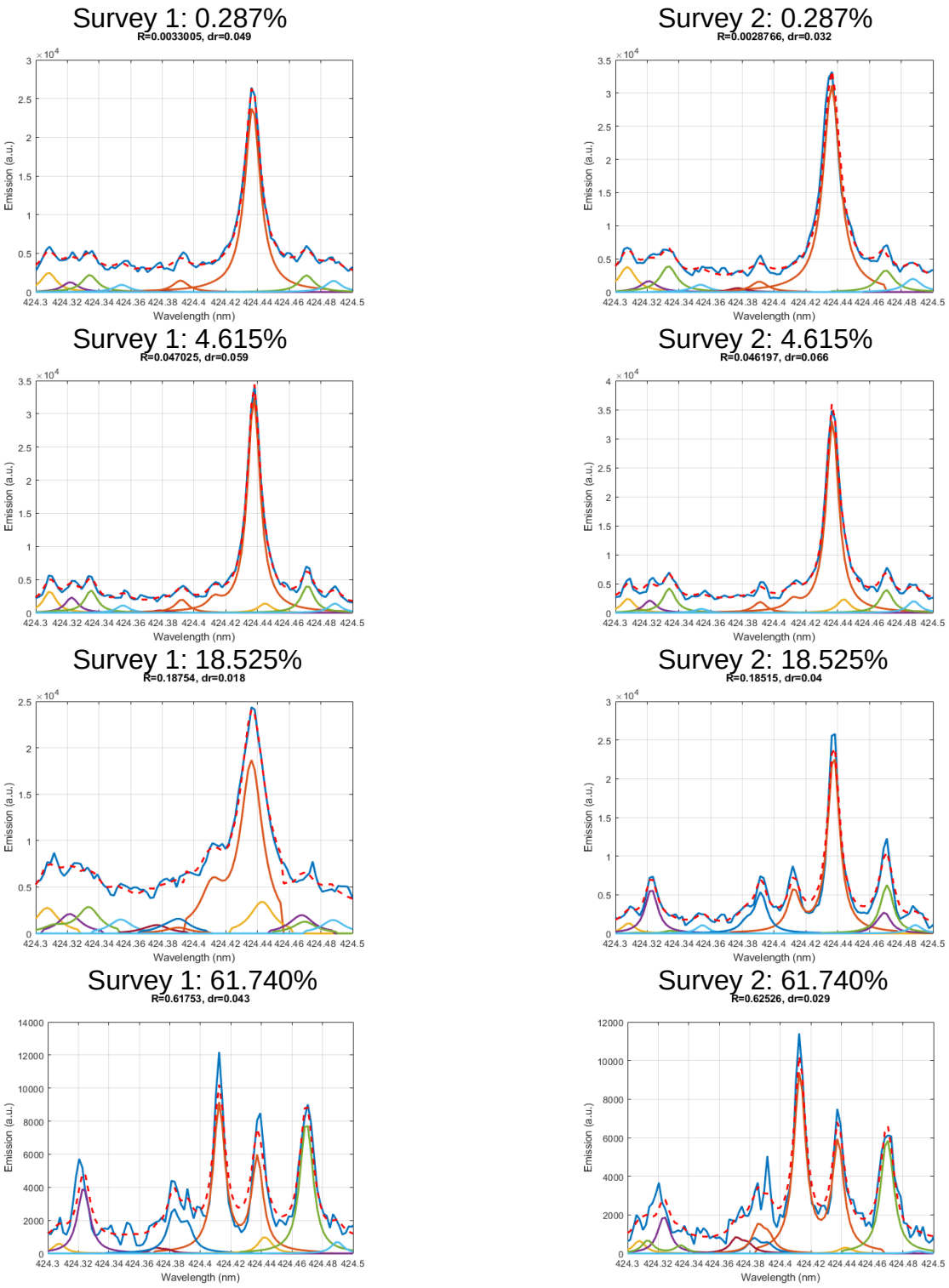


Figure 4.4. HPHP Survey Fits

Table 4.6. HPHP Survey Results

ORNL Report. Enrich.	**0.287%**		**4.615%**		**18.525%**		**61.740%**	
Delay and Gate Width (ns)	783-283	983-308	983-308	983-308	458-233	2358-433	2708-458	3083-483
MVNLSF Calc'd Enrich.	0.05%	0.40%	4.43%	4.44%	18.9%	18.4%	61.7%	61.7%
Error from ORNL Report. Enrich.	-0.24 %	0.11 %	-0.18 %	-0.18 %	0.33 %	-0.15 %	-0.01 %	-0.03 %
Standard Dev.	0.11%	0.82%	1.48%	1.63%	3.45%	2.24%	2.75%	5.95%
Relative Standard Dev.	224%	204%	33.3%	36.7%	18.3%	12.2%	4.5%	9.6%
RMSE	0.31%	0.75%	1.37%	1.52%	3.13%	2.06%	2.47%	5.33%
Mean Absolute Error	0.30%	0.54%	1.15%	1.29%	3.02%	1.74%	1.86%	4.96%

The 0.287% and 4.615% samples both have similar results for their first and second surveys where the most accurate delay and gate width began or ended at about the 1000 ns point after the laser trigger signal. The agreement between the delay and gate widths did not translate to alignment with the expected tendency toward overreporting of the less prevalent isotope since three of the four measurements are lower than the actual sample assay [27, 67].

LPLP Investigations

The LPLP Investigation test configuration retains the physical configuration previously discussed for the LPLP Survey and utilizes the investigation delay and gate widths listed in Table 3.3. The delay and gate width progression this research labeled as the investigation series reduces the rate of increase of the delay to only 5 ns (e.g., 5, 10, 15, …) for each successive delay and gate width combination.

The plasma emission intensity is expected to rapidly decay following the laser impulse as illustrated in Fig. 2.2. Therefore, the gate width in this series increases by a rate of 5 ns from one delay and gate width combination to the next, but it begins with a step of 10 ns (e.g., 10, 15, 20, …).

In the LPLP investigation the first 11 delay and gate width combinations are used before the emission becomes too weak to proceed further. The exposure required for the 11^{th} delay and gate width combination (358-413 ns) is 90 seconds. The ICCD integrates the emission from 90,000 laser pulses during these collections.

Fig. 4.5 shows selected spectra from each of the LPLP Investigations performed on the four sample chambers containing 61.740%, 18.525%, 4.615%, and 0.287% material. The spectra were collected with the delay and gate width settings shown in Table 4.7 for the corresponding assay. The specific spectra shown in Fig. 4.5 were selected for their closeness to the actual assay of the sample.

The SNR remained similar to that of the LPLP survey, producing a maximum of about 20:1 based on the emission intensity of the 424.4372 nm and 424.4122 nm isotopic pair versus the calculated noise from the detector.

Table 4.7 identifies the delay and gate width combination that provided the most accurate average assay calculated using MVNLSF to evaluate the HPLP Survey spectra. The MVNLSF-calculated enrichment, SD, RSD, RMSE, and MAE are the average of the MVNLSF results from dr=0.030 to dr=0.1.

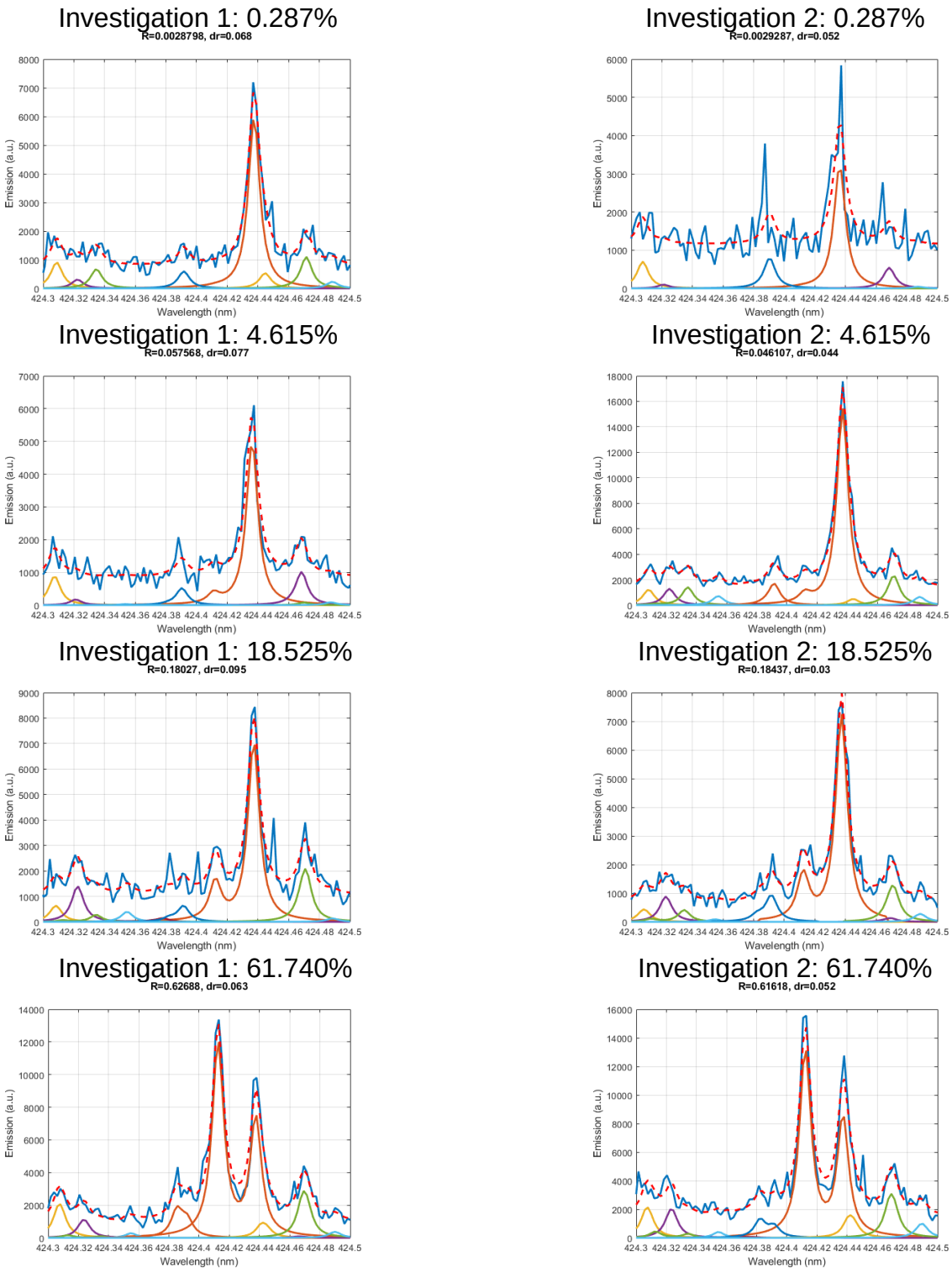


Figure 4.5. LPLP Investigation Fits

Table 4.7. LPLP Investigation Results

ORNL Report. Enrich.	**0.287%**		**4.615%**		**18.525%**		**61.740%**	
Delay and Gate Width (ns)	188-223	358-413	188-223	188-223	308-358	188-223	263-308	358-413
MVNLSF Calc'd Enrich.	0.25%	0.13%	4.03%	4.52%	18.9%	17.7%	61.3%	61.8%
Error from ORNL Report. Enrich.	-0.03 %	-0.16 %	-0.59 %	-0.10 %	0.37 %	-0.85 %	-0.39 %	0.03 %
Standard Dev.	0.43%	0.25%	3.19%	1.81%	3.70%	1.65%	2.22%	2.62%
Relative Standard Dev.	172%	193%	79.2%	40.0%	19.6%	9.3%	3.6%	4.3%
RMSE	0.39%	0.31%	2.92%	1.62%	3.33%	1.70%	2.03%	2.37%
Mean Absolute Error	0.33%	0.29%	2.63%	1.10%	2.37%	1.20%	1.83%	1.85%

HPLP Investigation

Fig. 4.6 shows selected spectra from each of the of the HPLP investigation. The spectra were collected with the delay and gate width settings shown in Table 4.8 for the corresponding assay. The spectra in Fig. 4.6 were selected for their closeness to the actual assay of the sample. With the exception of the first investigation of the 61.740% sample, the alignment between the measured spectra and the resulting spectral fit is significantly improved. The first 61.740% investigation spectrum exhibits the appearance of poor SNR and is the lowest, SNR=9.5:1, of the spectra in Fig. 4.6. The SNR ranges as high as 38:1 for the spectra in Fig. 4.6 based on the emission intensity of the 424.4372 nm and 424.4122 nm isotopic pair versus the calculated noise from the detector. The increased SNR allows more of the isotopic pairs to play a role in the spectral fitting.

During the HPLP Investigation there were some differences between the samples in terms of the number of delay and gate width combinations which could be tested before the emission became too weak to proceed. During the testing of the 0.287% sample the collection was terminated at the 1133-1238 step with an exposure of 37 seconds and the second repetition of the 0.287% sample investigation terminated at the 1238-1348 delay and gate width combination with an exposure of 55 seconds. The 4.615% sample was tested to the 1348-1463 delay and gate width combination and required 47 seconds of exposure. In the second repetition of the 4.615% investigation the signal was deemed too weak to proceed at the 1133-1238 delay and gate width combination. The 18.525% sample testing concluded with the 1033-1133 delay and gate width combination for both repetitions of the investigation and the exposure was 33 seconds. The first 61.740% investigations terminated at the 1583-1708 delay and gate width combination with an exposure of 70 seconds.

Table 4.8 identifies the delay and gate width combinations that provided the most accurate average assay calculated using MVNLSF to evaluate the HPLP Survey spectra. The MVNLSF-calculated enrichment is the average of the MVNLSF-calculated assay from dr=0.030 to dr=0.1.

The results in Table 4.8 noteworthy because they show that, although the 61.740% investigations produce the most accurate average assay measurements in later delay and gate width combinations, the other samples seem to trend toward earlier delay and gate width combinations for the most accurate average assay prediction. This tendency toward early delay and gate width combinations increases intensity available from the plasma and likely contributed to the apparent closer alignment of the measured spectra with the resulting spectral fit.

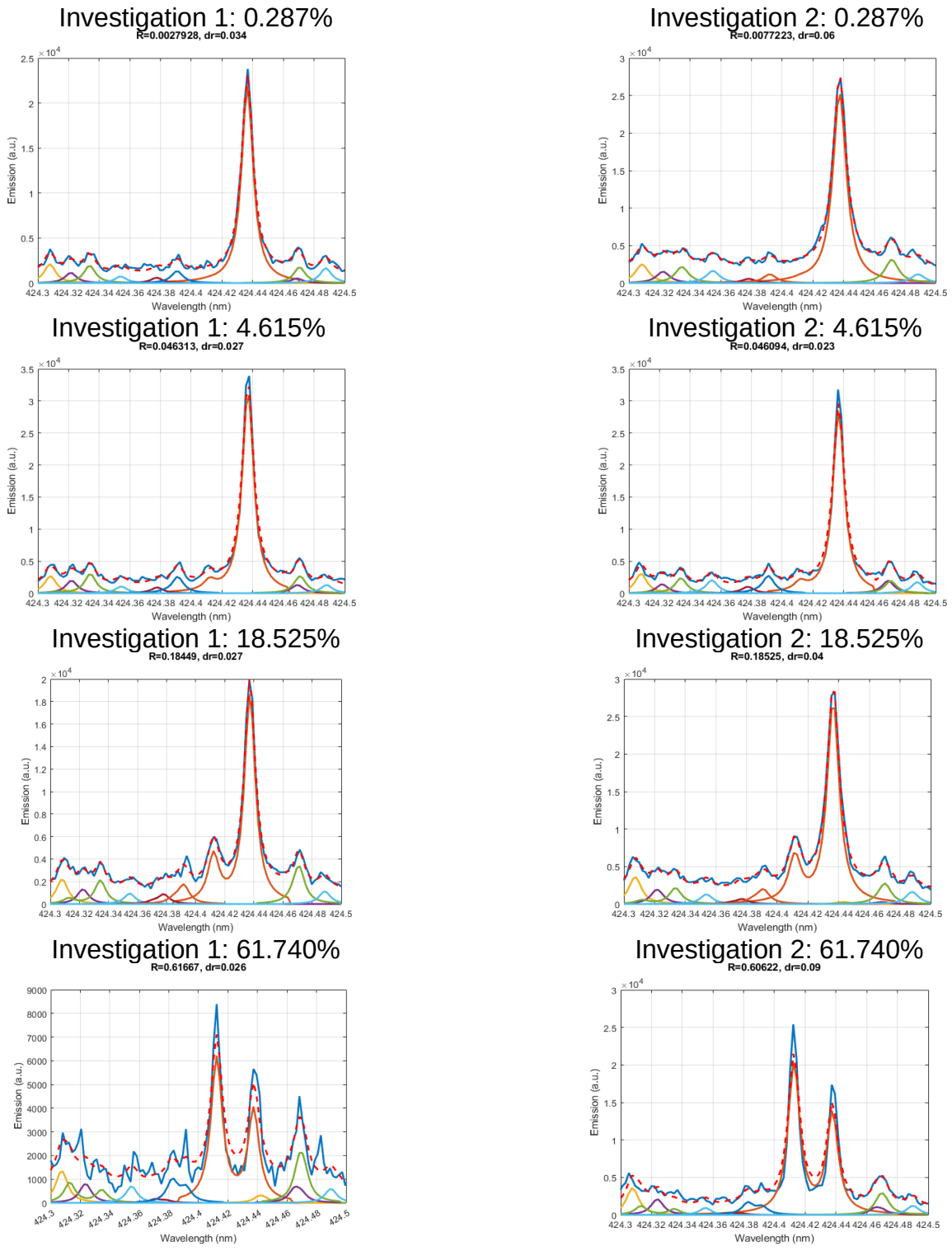


Figure 4.6. HPLP Investigation Fits

Table 4.8. HPLP Investigation Results

ORNL Reported Enrich.	**0.287%**		**4.615%**		**18.525%**		**61.740%**	
Delay and Gate Width (ns)	308-358	223-263	413-473	413-473	263-308	223-263	1463-1583	938-1033
MVNLSF Calc'd Enrich.	0.18%	0.18%	4.35%	4.71%	18.3%	18.9%	61.1%	61.5%
Error from ORNL Reported Enrich.	-0.11 %	-0.10 %	-0.27 %	0.10 %	-0.24 %	0.40 %	-0.64 %	-0.26 %
Standard Deviation	0.36%	0.40%	0.63%	1.46%	1.97%	1.51%	3.12%	1.34%
Relative Standard Deviation	198%	218%	14.6%	31.0%	10.7%	8.0%	5.1%	2.2%
RMSE	0.34%	0.37%	0.63%	1.31%	1.78%	1.41%	2.87%	1.22%
Mean Absolute Error	0.32%	0.35%	0.55%	1.17%	1.46%	1.19%	2.34%	0.98%

The first 61.740% sample investigation has the lowest SNR of any of the spectra selected for inclusion in Fig. 4.6. The first 61.740% investigation also has the highest standard deviation of this testing configuration. Given the weakness of the LPLP plasma and the challenge obtaining strong SNR, the HPLP was the next most likely testing configuration to produce highly accurate MVNLSF-measured assay and minimized standard deviations. The spectra in Fig. 4.6 (except the 61.740% investigation 1) do exhibit the reduced spectral clutter expected with the low-pressure testing and the resulting spectral fits are closely matched to the measured spectra, but this fact has not resulted in significantly improved assay measurement accuracy.

HPHP Investigation

The HPHP Investigation's most accurate spectral fits are shown in Fig. 4.7. The spectra were selected for their closeness to the actual assay of the sample. The alignment between the measured spectra and the resulting spectral fit is quite good. The SNR ranges between 28:1 and 45:1 for the spectra in Fig. 4.7 based on the emission intensity of the 424.4372 nm and 424.4122 nm isotopic pair versus the calculated noise from the detector.

The selected spectra included in Fig. 4.7 are from the most accurate delay and gate width combination shown in Table 4.9. Table 4.9 shows that the standard deviation does tighten to 0.26% for the second investigation of the 0.287% sample. The standard deviation reaches 1.79% for the second investigation of the 18.525% sample.

The trend of significant error in the assay reported for the 61.740% sample continues in the HPHP investigation results. Also, of note in Table 4.6 is that the HPHP testing configuration yielded two close measurements of average assay for the 61.740% sample. Both measurements are greater than the actual assay of the sample. This is contrary to the expectation of biased reporting due to self-absorption of the more prevalent isotope [27, 67].

Both of the 61.740% sample's delay and gate widths which produced this over reporting of the assay occurred quite late in the plasma life. The same is true of the 18.525% sample measurements, but in this case one of the measurements is lower than actual and the other is higher.

The 0.287% and 4.615% samples both have similar results for their first and second surveys where the most accurate delay and gate widths begin close to 1000 ns after the laser trigger signal and run to between 1500 ns and 2000 ns after the laser trigger signal.

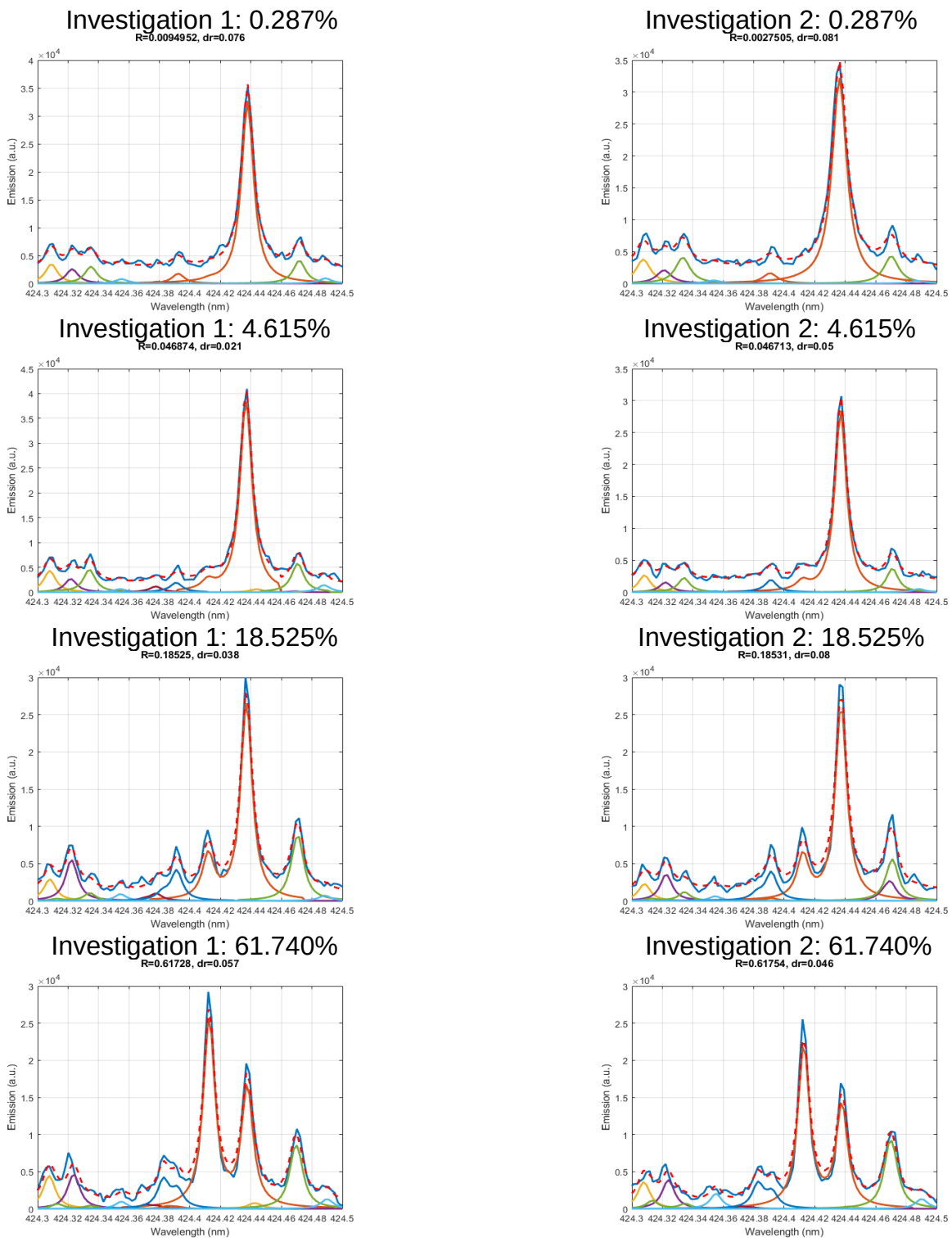


Figure 4.7. HPHP Investigation Fits

Table 4.9. HPHP Investigation Results

ORNL Reported Enrich.	**0.287%**		**4.615%**		**18.525%**		**61.740%**	
Delay and Gate Width (ns)	848-938	763-848	848-938	938-1033	1708-1838	1708-1838	1583-1708	1348-1463
MVNLSF Calc'd Enrich.	0.24%	0.12%	4.79%	4.77%	18.6%	18.2%	62.3%	62.4%
Error from ORNL Reported Enrich.	-0.05 %	-0.17 %	0.17 %	0.16 %	0.05 %	-0.31 %	0.60 %	0.70 %
Standard Deviation	0.54%	0.26%	1.07%	0.61%	0.76%	1.79%	0.93%	1.28%
Relative Standard Deviation	222%	222%	22.3%	12.7%	4.1%	9.8%	1.5%	2.1%
RMSE	0.49%	0.34%	1.01%	0.67%	0.82%	1.69%	1.03%	1.35%
Mean Absolute Error	0.41%	0.29%	0.82%	0.57%	0.70%	1.50%	0.81%	1.15%

Steps Taken to Enhance Spectral Information

The fs-LIBS system was challenged by the small plasma emission produced, especially in the LPLP configurations. Even the HPHP configurations, with approximately double the SNR, did not meet the hopes for fs-LIBS in terms of MVNLSF-measured assay accuracy or standard deviation of reported assays. Several steps were taken to improve the data analysis as well as enhance the spectral collection process.

Signal to Noise Ratio Enhancement

The reduction of noise and the enhancement of the signal seemed a key step to attempt to improve the ability of the MVNLSF fitting algorithm to report an assay from the captured spectra. The following enhancements were implemented and tested in the HPHP testing configuration. To reduce the noise expected from the ICCD, the speed at which the analog-to-digital (A/D) conversion takes place between the chip containing the photo-sensors and the 16-bit binary numbers interpretable by a computer was reduced from 5 MHz to 1 MHz. Additionally, the preamplifier gain for the ICCD was increased to 2X in an attempt to increase the signal strength at the same time the noise was being reduced by the A/D conversion speed reduction. Based on Andor's performance report for the ICCD, the resulting noise band around the actual no-noise counts will be reduced from about 900 counts to about 475 counts.

In addition to the changes to the ICCD settings, the exposures were extended to further increase the signal strength. The combination of the ICCD settings changes and the lengthened exposure increased the counts associated with the 424.437 nm emission line from a maximum of 35,500 under the original process and settings, to as high as 700,000 counts. Correspondingly, the SNR increased from a max of about 40:1 to as high as 1400:1 for the 424.4372 nm and 424.4122 nm isotopic pair. The 424.4372 nm emission line, or its isotopic shift the 424.4122 nm emission line, are the most intense in the spectral region being investigated. The increased SNR would affect all of the lines of interest in proportion to their intensity.

The expectation had been that the enhanced SNR would translate into better assay measurement results from the MVNLSF algorithm. Fig. 4.8 shows the resulting fits from application of the MVNLSF algorithm as well as the reported assay, R. The *dr* value for the spectral fitting is also shown. The alignment of the resulting spectral fits are at least as good as the spectral fits achieved during the HPHP sampling conditions. As in the earlier spectral fitting figures, the figures shown are the spectra and *dr* combinations. Selected from the best performing delay and gate width combination, which produced a measured assay close to the actual ORNL-reported assay.

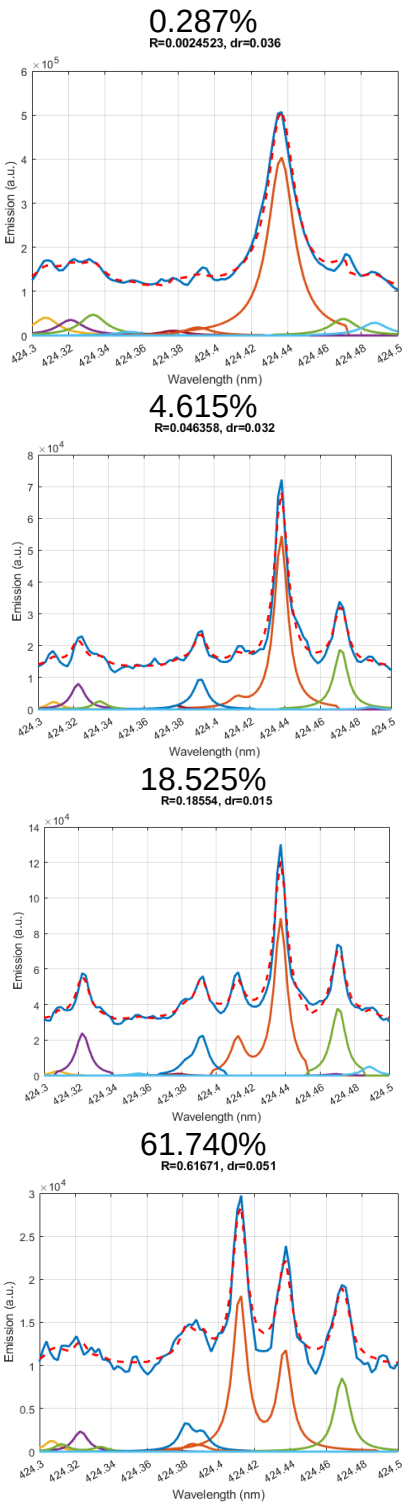


Figure 4.8. Improved SNR MVLSF fits

As in the earlier sections, Table 4.10 reports the MVNLSF-calculated enrichment, SD, RSD, RMSE, and MAE which are the average of the MVNLSF results from *dr*=0.030 to *dr*=0.1 for the five spectra collected at each delay and gate width combination tested. The noted delays and gate widths in Table 4.10 are those which produced the most accurate assay measurements for that particular sample.

Confirmation of ICCD Detector Offset Approach

Spectral clutter reported by the fs-LIBS system itself has a potential to impact the assay measurements undertaken on the collected spectra. To eliminate the possibility that the ICCD had developed some flaw potentially affecting the MVNLSF algorithm, dark images were captured. As had been the case when the ICCD was first being characterized, there were still several pixel columns which routinely had higher than normal readings when no light source was present for measurement. These, so called “hot pixels” were still off center toward the lower wavelength side of the area of the ICCD’s chip used for this research. The data collection was confirmed to still be targeted in areas that did not include these “hot pixels”.

Examining the dark images did not reveal any new hot pixels or failed pixels. The dark readings present in the region of interest of the ICCD appeared to be truly random and level on average from one side of the viewing range to the other. Cremers et al. recommend that the baseline be interpolated and subtracted point by point as part of their recommended preprocessing steps [33]. Therefore, to confirm that nothing was being missed in the interpretation of the dark images and to investigate the pre-processing recommendation, a test was developed for the fs-LIBS system to validate the assumption that the detector offset could be assumed to be a single constant subtracted from each pixel.

Once the first several rounds of data analysis were complete, a list of delays, gate widths, and exposures which produced the most accurate assay predictions were available. Five dark spectra were collected with the highest accuracy delay, gate width, and exposure settings. The laser was used for the triggering and all other settings on the spectrometer, ICCD, and computer were preserved, but the shutter to the laser remained closed during these collections. Subsequently, these five dark spectra were averaged and subtracted from the previously collected spectra that had produced the most accurate assay predictions. The subtraction is performed at the 1024-by-1024-pixel level so there is no risk of impact from vertical binning or calibration. The subtraction is on a pixel basis and could be a different value for every pixel based on the average values from the five dark images collected so there is no single offset established and subtracted as is the case in the baseline detector offset approach.

Table 4.10. Improved SNR Results

ORNL Reported Enrich.	**0.287%**	**4.615%**	**18.525%**	**61.740%**
Delay and Gate Width (ns)	445-150	1445-275	2020-325	2020-325
MVNLSF Calc'd Enrich.	0.33%	4.84%	18.63%	61.25%
Error from ORNL Reported Enrich.	0.05%	0.23%	0.10%	-0.49%
Standard Deviation	0.65%	1.65%	2.12%	5.17%
Relative Standard Deviation	195%	34.1%	11.4%	8.4%
RMSE	0.58%	1.50%	1.91%	4.65%
Mean Absolute Error	0.44%	1.15%	1.53%	3.74%

The intention with this test was to determine if there was any benefit to the MVNLSF assay measurement by using an averaged dark image from the detector. Fig. 4.9 shows that the results were extremely similar with each approach producing the most accurate assay reporting about half the time. The results were similar enough that the ICCD having developed a problematic group of pixels was eliminated as a potential error driver. Additionally, since the results did not conclusively point to the need for a point-by-point interpolated baseline subtraction, the testing proceeded with the baseline method of subtracting a constant detector offset from each pixel.

Effect of Averaging Spectra as Opposed to Averaging R values

The results reported thus far are the result of the MVNLSF algorithm applied to each of the five spectra collected at each delay and gate width setting individually. Then the five resulting assay measurements were averaged together to produce the data reported in the preceding sections. A series of MVNLSF assay predictions were made using a single average spectrum at each delay and gate width setting created from the five spectra collected at each delay and gate width setting. This is one of the spectrum preprocessing operations recommended by Cremers to prepare spectra for quantitative analysis that had not yet been evaluated [33]. These averages of the five spectra at each delay and gate width setting were generated in three distinct ways: calculating the arithmetic average of the raw incoming image data, executing dynamic time warp barycenter averaging (DBA) of the fully vertically binned spectra, and application of Piecewise Cubic Hermite Interpolating Polynomial (PCHIP) to generate a representative spectrum from the five fully vertically binned spectra at each delay and gate width setting [100, 122].

DBA and PCHIP are both methods of interpolating a representative signal, or spectra in this case, while preserving the shape of the spectra. None of the spectra averaging approaches produced significantly different result from the baseline process. DBA performed essentially the same as calculating the arithmetic average of the raw incoming image data. The absolute value of the average errors at each delay and gate width combination for DBA and the original approach are within 0.005% of each other, with each having the lower value about half the time. The PCHIP interpolation of the five spectra collected at each delay and gate width produced absolute average error values that were 0.005% larger than either DBA or the original method of averaging the resulting MVNLSF-calculated assay from the five spectra collected at each delay and gate width combination. The conclusion from this test is that spectra-averaging does not produce significantly different results from the baseline process.

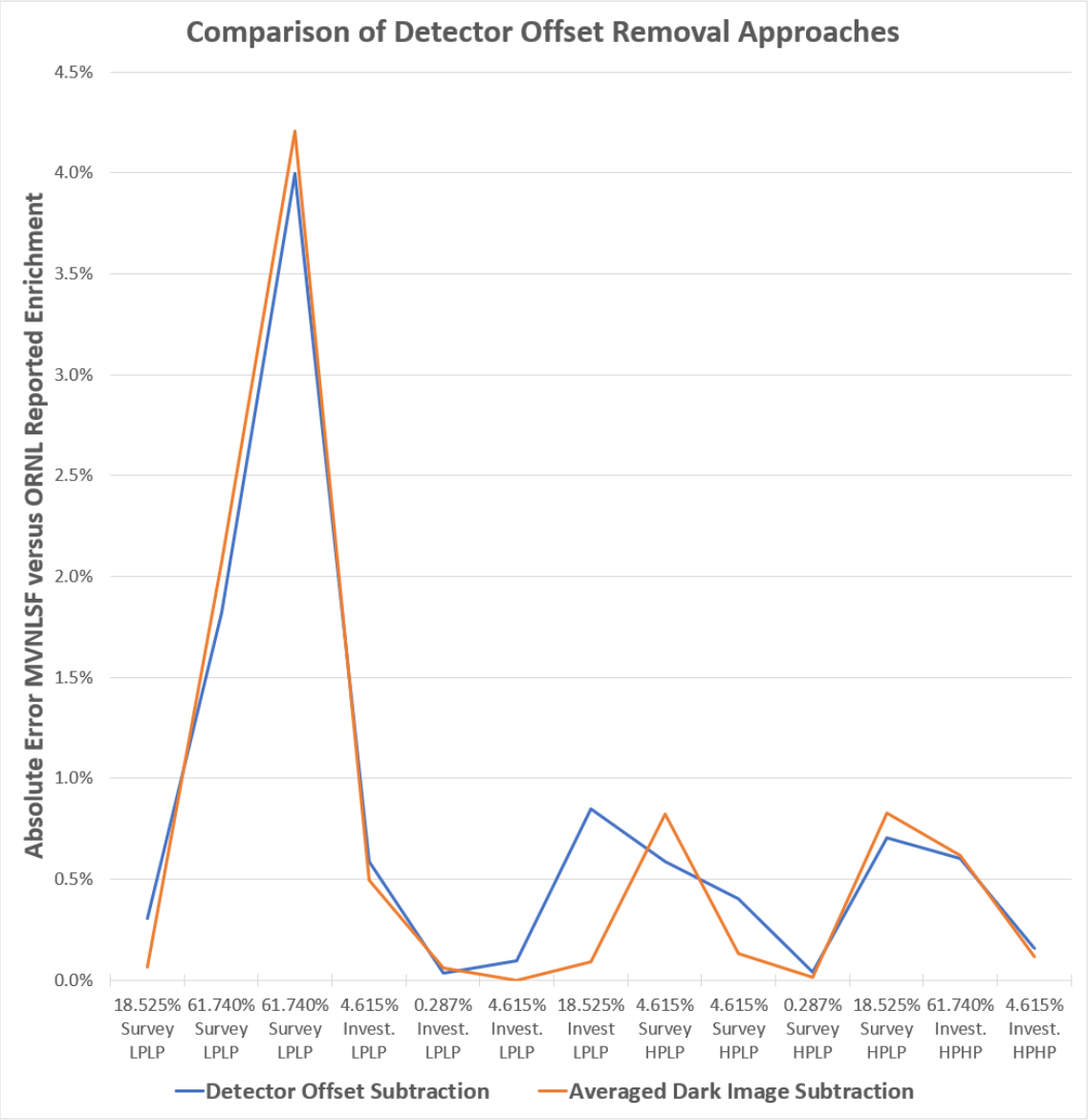


Figure 4.9. Graph comparing subtraction of a single detector offset value from each pixel versus an offset based on the pixel-by-pixel subtraction of the offsets obtained from multiple dark images.

Fitting Entire Wavelength Window Instead of *dr* Approach

The spectra that resulted from especially the lower power testing configurations yielded poor SNR. One of the hypothesized benefits of the *dr* fitting window approach was that the fitting algorithm would be targeted on reducing the fitting error around isotopic shifts that contribute to the assay measurement. This fitting window strategy is an attempt to reduce the chances that the MVNLSF routine would be attempting to fit spectral clutter as opposed to valuable spectral peaks.

There are two key ways in which the *dr* fitting window has direct impact on the error minimization algorithm. The first key impact is that if there is an area of the spectral window which is not covered by a *dr* window associated with one of the isotopic pairs being evaluated, then that uncovered portion of the spectral window is not included in the error calculation.

The second key impact is that even after the *dr* windows are large enough that they cover the entire spectral window without any uncovered areas, the *dr* value still plays a role in the error minimization. The *dr* window for each isotopic pair still serves as a cutoff point for that isotopic pair's Lorentzians to contribute to the overall fit in the spectral window.

Following the initial application of the MVNLSF using the *dr* fitting windows, the exact same spectra which yielded the most accurate assay measurements were rerun with the MVNLSF fitting algorithm adjusted to fit each Lorentzian associated with every isotopic pair over the entire spectral fitting window from 424.3 nm to 424.5 nm. Once the spectra had been re-analyzed using the entire wavelength window, the errors from the measured assay versus the ORNL reported assay were compared.

For each test conducted in each sampling configuration the square root of the sum of the squared assay errors for the 0.287%, 4.615%, 18.525%, and 61.740% samples were calculated for both the *dr* fitting window approach and the approach using the entire fitting window. The comparison of the resulting square root of the sum of the squared areas at each test and sampling configuration is shown in Fig. 4.10.

Although the two approaches are quite close in their error results, the *dr* fitting window approach produced more accurate assay measurements twice as often as the approach of fitting each Lorentzian over the entire spectral window. The conclusion drawn from this test is that use of the *dr* fitting window approach, including the averaging of the MVNLSF results from dr=0.030 to dr=0.1, does have benefit obtaining accurate assay measurements.



Figure 4.10. Graph comparing the "*dr*" Fitting Window approach with the approach of treating the entire spectral window (e.g., 424.3 nm to 424.5 nm) as the area over which fitting error will be minimized.

Comparing Survey, Investigation, and Kinetic Series Results

The fs-LIBS system provided data through three sampling conditions: LPLP, HPLP, and HPHP. There were also three delay and gate width series executed: survey, investigation, and kinetic series. The kinetic series data was collected with adjustments to the ICCD and exposure to increase SNR. Tables 4.11, 4.12, and 4.13 report the summary performance from each. The average error reported in Tables 4.11, 4.12, and 4.13 differs from the reporting in the previous testing configuration results tables. Tables 4.11, 4.12, and 4.13 do not provide information about whether the error was biased above or below the actual assay. Since the potential for opposite biases canceling one another exists in these tables, the absolute value of the errors reported in the previous tables is taken to allow the averaging of the measurements.

The lowest average error magnitude occurred in the HPHP Survey testing configuration. The survey was characterized by large steps in delay but the gate widths were held relatively short in comparison to the investigation measurement series. The smallest average SD, RMSE, and MAE occurred during the HPHP Investigation test configuration series. The investigation series was characterized by smaller steps in the delay, but the gate widths were allowed to grow quite large. The investigation series was targeted at determining where the most valuable plasma emissions began and then using the long gate widths to attempt to compensate for the weak plasma emission intensity in an effort to hold down the collection times.

Surprisingly, even with SNRs over 1400:1, the Kinetic Series did not result in improved assay prediction or minimized standard deviations. The improved SNR Kinetic Series focused on long exposure times to create the improved SNRs and it came close to achieving an average error as low as the HPHP Survey's. Oddly, the Kinetic Series standard deviation is nearly as high as the LPLP Survey results. The Kinetic Series results are also in contrast to the closeness of the resulting spectral fits to the measured spectral data. Although the spectral fits exhibited little fitting error, the assay predictions were more variable within the five spectra collected at each delay and gate width combination.

The biggest difference between the Kinetic Series and the HPHP Investigation, besides the significantly improved SNR for the Kinetic Series, is the gate widths. The gate width for the Kinetic Series increases by 25 ns for each subsequent delay and gate width combination, whereas the gate width for the HPHP Investigation increases at a rate of 5 ns for each successive delay and gate width combination (e.g., 10, 15, 20, …). This produces very long gate widths for the HPHP Investigation. The best performing gate widths for the HPHP Investigation ranged from 848 ns to 1838 ns. Although the Kinetic Series contained lengthier delays than the HPHP Investigation, its longest gate width is only 325 ns long.

Table 4.11. Comparison of Performance Statistics in Survey Configurations

Testing Configuration	**HPHP**	**HPLP**	**LPLP**
Average Error from ORNL Reported Enrichment	0.15%	0.79%	1.10%
Average Standard Deviation	2.30%	1.06%	2.51%
Average Relative Standard Deviation	67.8%	39.2%	63.9%
Average RMSE	2.12%	1.31%	2.79%
Average Mean Absolute Error	1.86%	1.09%	2.28%

Table 4.12. Comparison of Performance Statistics in Investigation Configurations

Testing Configuration	**HPHP**	**HPLP**	**LPLP**
Average Error from ORNL Reported Enrichment	0.28%	0.27%	0.32%
Average Standard Deviation	0.90%	1.35%	1.98%
Average Relative Standard Deviation	62.1%	60.9%	65.1%
Average RMSE	0.92%	1.24%	1.83%
Average Mean Absolute Error	0.78%	1.05%	1.45%

Table 4.13. Performance Statistics for Improved SNR Kinetic Series

Testing Configuration	**HPHP Kinetic Series**
Average Error from ORNL Reported Enrichment	0.22%
Average Standard Deviation	2.40%
Average Relative Standard Deviation	62.31%
Average RMSE	2.16%
Average Mean Absolute Error	1.72%

Plasma Emission Valuation

The results from analysis with the MVNLSF approach yielded different optimum delay and gate widths for each sample. To investigate this matter, every captured spectrum was evaluated individually via MVNLSF. For each sample, the spectra were ranked in order of how accurately MVNLSF predicted the actual assay of the sample. Those spectra, with their associated delays and gate widths, which yielded MVNLSF assay predictions within 0.5% ^{235}U for the 4.615%, 18.525%, and 61.740% samples, were labeled as providing good assay measurement. The 0.287% sample spectra were only considered to provide good assay measurements if their MVNLSF predictions were within 0.28% of the actual assay. This approach prevented spectra and MVNLSF assay predictions of 0 from being counted as good for the 0.287% sample. This segregation of the data into two classes, good-assay-prediction-value and not-good-assay-prediction, allows a value judgement of each nanosecond of plasma emission's contribution to accurate MVNLSF-based assay prediction.

To execute this plasma emission valuation, a timeline of the plasma emission is created that includes every combination of delay and gate width. This timeline begins when the trigger pulse from the laser is transmitted. The timeline ends at the greatest combined delay and associated gate width. Each nanosecond of plasma life between laser trigger (time zero) and the maximum delay and gate width summed, represents a bin on the timeline for a pareto-type evaluation.

A MATLAB routine was created that would perform the tedious work of binning the delay and gate width information. The routine cycles through every delay and gate width combination that provided a good assay prediction. For each nanosecond within the delay and gate width range of the good MVNLSF predictions, a value of one was added to each corresponding bin on the timeline of plasma life. This step is repeated for every spectrum that provided good MVNLSF prediction. Separately, the MATLAB routine goes back through every spectrum captured for each delay and gate width combination regardless of whether it was labeled as good or not to determine how many chances each nanosecond on the plasma emission timeline had as potential opportunities to provide a good measurement. Next the number of times the nanosecond was included in a good spectrum is divided by the number of times that nanosecond was included in any of the delay and gate width combinations. Fig. 4.11 shows the resulting plasma emission valuation of this pareto-type evaluation of the most accurate gate width and delay combinations. Fig. 4.11 includes every testing configuration on each plot; LPLP, HPLP, and HPHP. The blue dots represent the binned data corresponding to what percentage of the opportunities in the test data that nanosecond contributed to a good measurement. The red line is a polynomial fit to the binned plasma emission valuation to assist with identification of local maximums.

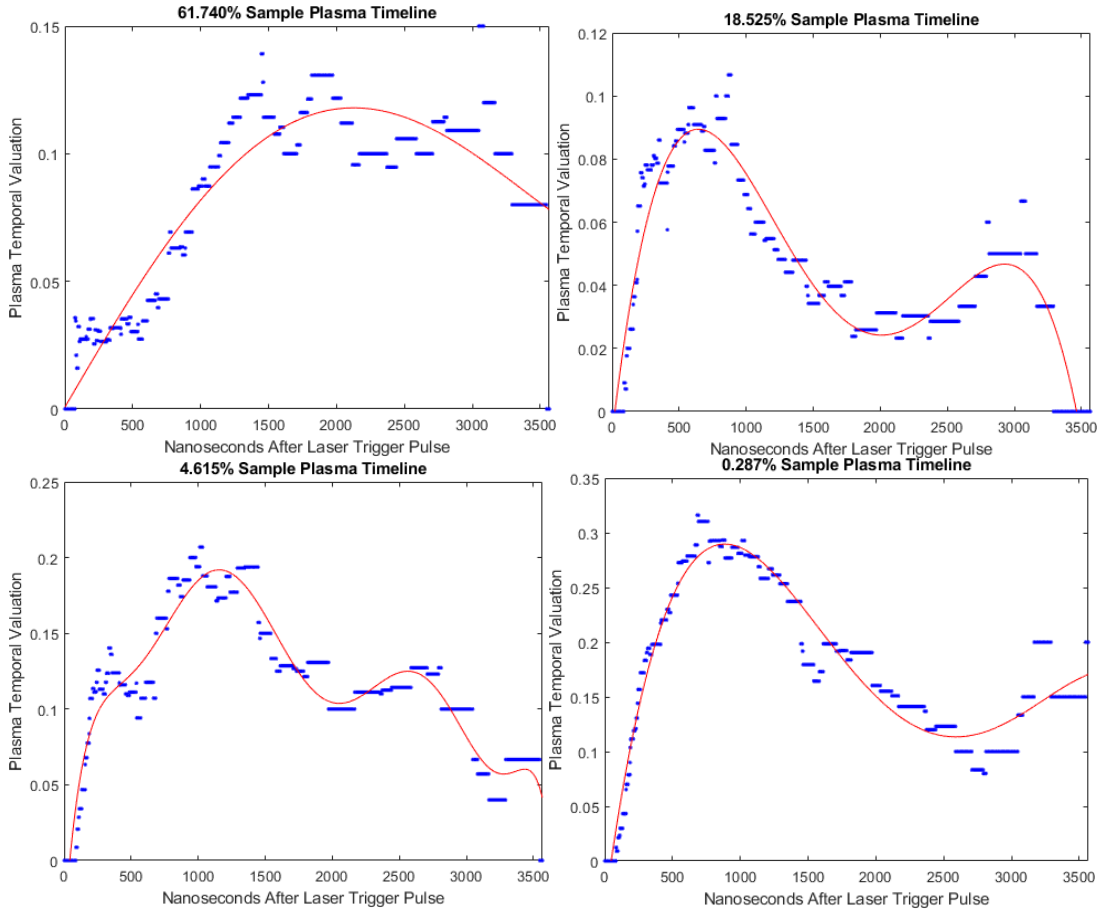


Figure 4.11. Plasma Emission Valuation Timelines showing each nanosecond of plasma life from 0 to 3566 ns based on that nanosecond's inclusion in a delay and gate width combination that yielded a "good" MVNLSF-12-based assay prediction.

The results shown in the plasma emission valuation clearly indicate that there is a difference between the samples in terms of when in the plasma life the most valuable emissions for assay prediction occur. The 4.615% and 61.740% samples have local peaks of valuable emissions before rising to their peaks of ~1000 ns and ~2000 ns respectively after the laser trigger signal. The 18.525% and 0.287% samples seem to follow a different pattern of fewer undulations in their valuation timeline and highest value plasma emissions occurring before 1000 ns.

An initial theory was that this difference in the delay and gate widths which provide the most accurate assay measurement could be related to the pressure of the sample chambers. The sample pressures had been logged and reported in Table 4.2. but there seems to be no correlation between the pressures and the most valuable delay and gate width combinations. The pressure data indicates that the 61.740% sample and the 18.525% sample have some similar pressures in the LPLP configuration hovering around 6 Torr. This does not align with the patterns shown in the plasma temporal valuation. As the pressure increases through the sampling conditions, the pressure of the samples seems to trend toward the 61.740% and 0.287% samples having similar high-pressure values near 56 Torr. The 4.615% sample and 18.525% sample average 54.2 and 52 Torr respectively in the HPHP testing configuration. This behavior also does not match what is observed in the plasma emission valuation.

The laser power shown in Table 4.1 also does not provide any clear explanation of what could be causing the different delay and gate width values between the samples. An effort was made to estimate the decay of the plasma emission. The plasma decay showed very similar decay constants for each of the four samples. What little difference there was showed that, in a similar grouping to the LPLP pressure data, the 61.740% and 18.525% samples had similar decay constants and the 4.615% and 0.287% samples showed similarities. Again, there is no clear pattern that matches the plasma emission valuation.

In a final attempt to verify that there was, in fact, a difference between the samples' temporal plasma emission valuations, a kinetic series test was performed where the ICCD is programmed to take a series of frames that capture the plasma emission temporally by indexing the delay and gate width values so that as one frame, or delay and gate width combination, ends the next one immediately begins. The kinetic series data collection was repeated five times for each sample to create the opportunity to analyze five spectra at each delay and gate width combination. The delay and gate width settings used for this kinetic series are shown in Table 3.4. Note that the kinetic series ends with a delay of 2020 ns and a gate width of setting of 325 ns. Therefore, there is no plasma valuation beyond 2345 ns.

Fig. 4.12 shows the four samples' plasma emission valuations broken down by sampling condition. The Kinetic Series delay and gate width associated with the most accurate MVNLSF assay measurements are also shown in Fig. 4.12 as stem plots for each nanosecond included in the delay and gate width combination.

The Kinetic Series data was collected in the HPHP configuration, so the stem plots are only included in the HPHP column of graphs. The agreement between the plasma emission valuation and the Kinetic Series is quite good, as evidenced by the alignment between the peak of the plasma emission valuation data and the location of the kinetic series stem plots, in Fig. 4.12 in every case except the 18.525% sample. However, we need to recall that the Kinetic Series ended 2345 ns after the laser trigger pulse. Therefore, the 18.525% kinetic series has achieved as close an alignment as is possible in this case with the plasma emission valuation data from the HPHP testing. Although a specific cause has not been proven for the difference in where the most valuable plasma emissions occur in the various samples, the difference is genuine based on the agreement between the plasma emission valuation timeline and the Kinetic Series results.

Potential Cause of Plasma Emission Valuation Difference by Assay

Examination of the Fig. 4.12 HPHP data, including the stem plots associated with the kinetic series, indicates that there may be a trend toward later high-value plasma emissions as assay increases. Additionally, there appears to be a common behavior between the 0.287% and 4.615% plasma emission value in that a steady rise is shown for each up to the peak plasma temporal value occurring between 500 and 1000 ns. This is in agreement with a publication by Rai and Thakur indicating that singly ionized and neutral atomic emissions are observed nearly 500 ns after plasma formation [121]. Each of the isotopic shifts shown in table 2.1 is attributable to a neutral or singly ionized atomic emission [67, 87, 88].

Similarly, a different behavior is shown in the Fig. 4.12 HPHP data for the 18.525% and 61.740%. There is more undulation in the plasma temporal valuation in the early part of the 18.525% and 61.740% emission before ultimately rising to a more sustained high-level plasma emission valuation that is more or less maintained until the end of the temporal window shown in Fig. 4.12. Note, that the agreement between the kinetic series stem plot and the plasma temporal valuation from the HPHP survey data and HPHP investigation data is as close as possible in these cases because the kinetic series has no later delay frames in its series.

One of the ways that this apparent assay dependence was investigated by looking at the contribution of the individual isotopic shifts contribution to the overall fitting denoted by the variable A_i which represents the area of the spectral peaks in equation (10). A pattern emerged which may be connected to the plasma temporal valuation behavior. The variable A_i values associated with isotopic pair number 7 in table 2.1 made up of the 424.3914 nm ^{238}U emission and the 424.3822 nm ^{235}U emission has an importance that steadily increases with increasing assay. Conversely, the variable A_i values associated with isotopic pair number 4 in table 2.1 made up of the 424.3344 nm ^{238}U emission and the 424.3127 nm ^{235}U emission has an importance that markedly decreases with increasing assay. The variable A_i values associated with isotopic pair number 4 are the 3rd and 4th largest in magnitude for the 0.287% and 4.615% samples. In the fitting of the 18.525% samples the variable A_i values are 8th or 9th largest and for the 61.740% sample they are the 11th or 12th largest. This means that although isotopic pair number 4 plays a prominent role in the fitting of the low assay samples it's importance steadily drops to the point that it is the least important isotopic shift for fitting the 61.740% sample. It is likely that the timing of the emission of these two isotopic pairs plays a significant role in the observed differences in the most accurate delay and gate width combinations for the samples in this research.

Precipitate Buildup in 38.103% Sample Chamber

A buildup of a grayish white substance formed on the interior surfaces of the 38.103% sample chamber during the very first fs-LIBS testing it received. The sample chamber was totally absent of any detectable deposition of any sort prior to the first fs-LIBS testing. Pictures of the way the precipitate appeared on the collection window as well as images, taken through clear portions of the laser exit window, showing how the precipitate appears on the inside of the 38.103% sample chamber are shown in Fig. 4.13.

The collection of the five repeated spectra was in process as the buildup formed. The effect on the plasma emission reaching the detection system can be observed in the captured spectra. Fig. 4.14 shows successive 20 second captures with a delay setting of 83 ns and a gate width of 108 ns. Note the steadily diminishing signal strength as the precipitate obscures optical access to the plasma.

The initial fs-LIBS analysis of this sample initiated when the sample pressure was 15.2 Torr. This pressure was considered slightly elevated relative the pressure that other samples were able to achieve when chilled by the thermoelectric cooler. The next highest pressure sample chamber under cooling is the 4.615% sample which typically achieved 11.1 Torr.

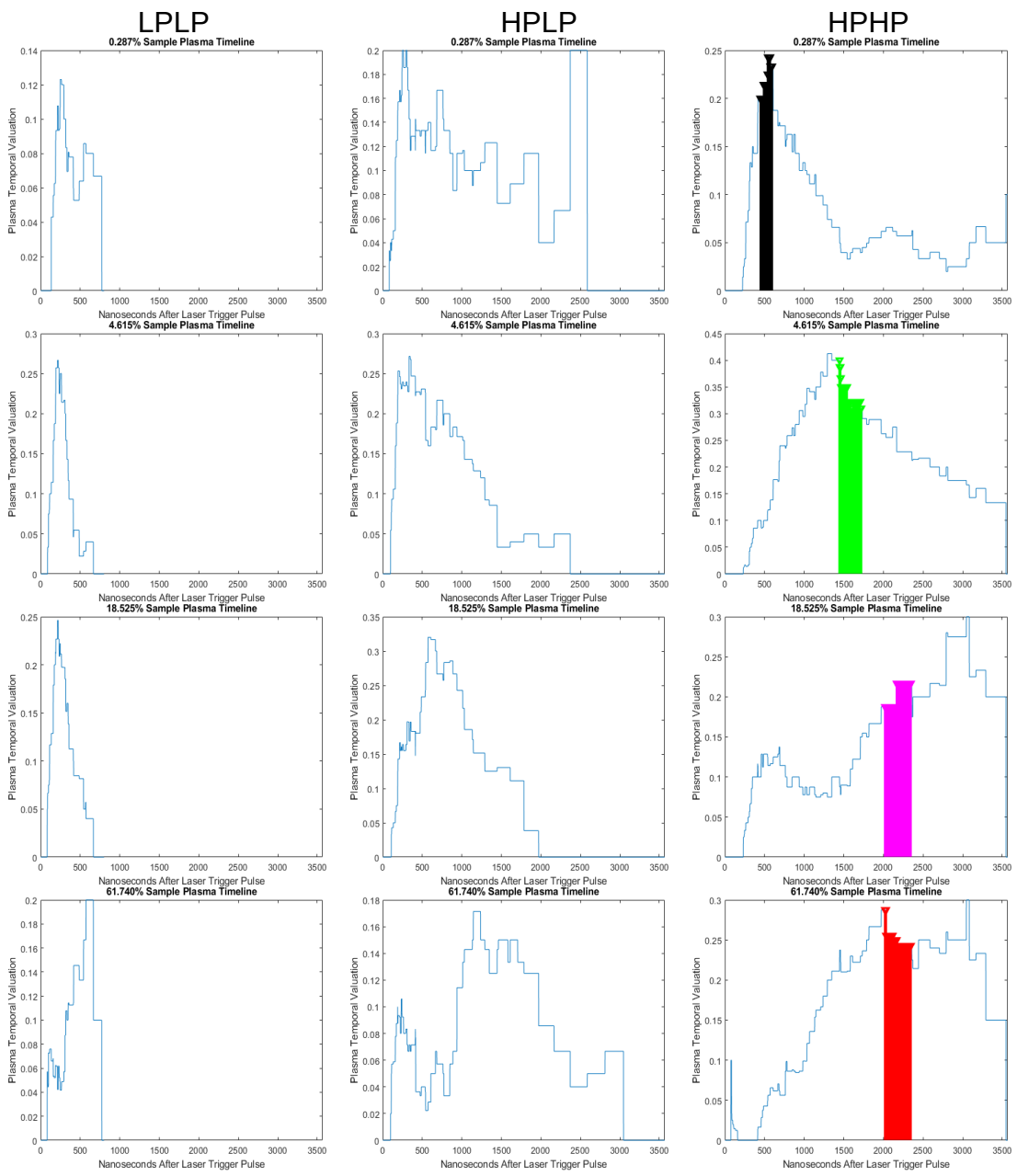


Figure 4.12. Plasma Emission Valuation Timelines of each testing configuration showing each nanosecond of plasma life from 0 to 3566 ns based on that nanosecond's inclusion in a delay and gate width combination that yielded "good" MVNLSF-12-based assay predictions.

Initial Formation of Precipitate



Plasma Viewed Through Precipitate



Precipitate Following HPHP Testing



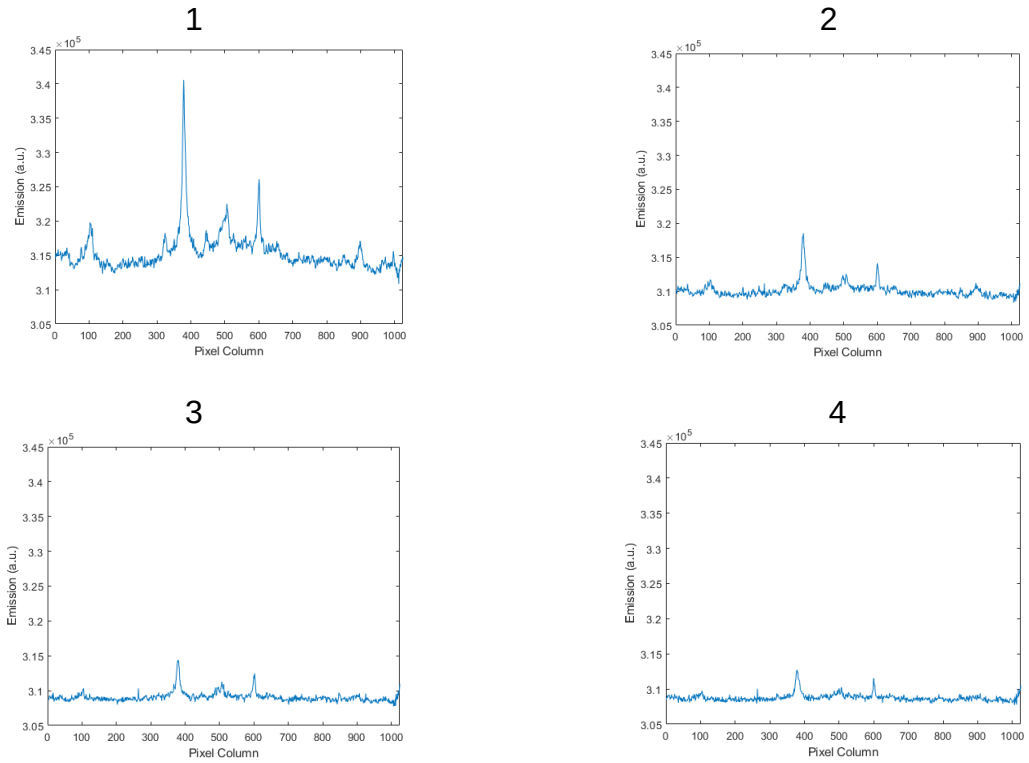
Precipitate on Laser Exit Window



Precipitate on Collection Window Interior Viewed Through Clean Section of Laser Exit Window



Figure 4.13. Precipitate formation on 38.103% Sample Chamber



Five 38.103% Spectra During Precipitate Formation

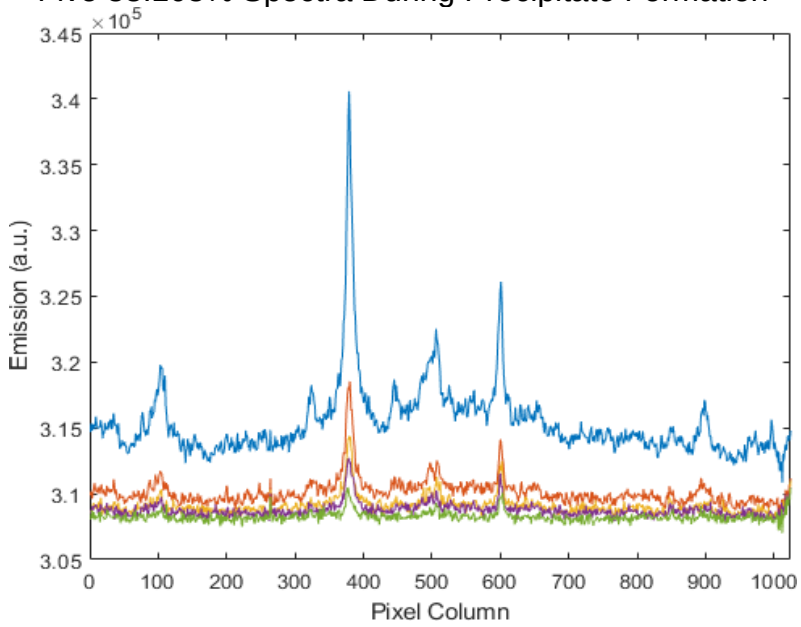


Figure 4.14. Progressive data captures while precipitate forms in 38.103% sample chamber.

The fogging from the precipitate was the most pronounced on the 38.103% sample chamber, but there were slight hazes that would form on the other sample chambers. Examples of the precipitate formation observed on the other sample chambers is shown in Fig. 4.15.

There has been a similar experience with some sample chambers in use at both ORNL and LBNL [24]. The national laboratory research team reported that once the reaction occurs the sample chambers which experience this fogging or cloudiness have slightly increased pressure by one or two Torr [123]. The lab research team reported that they had not been able to correlate the formation of the white precipitate with the amount of LIBS interrogation of the sample [123]. Seemingly, some sample chambers react forming the white precipitate and some do not [123].

A reasonable, but-yet-to-be-proven, theory is that a contaminate is present that does not react with the UF_6 until plasma-induced dissociation of the UF_6 molecule has occurred. After dissociation, a free fluorine atom may react with the contaminant. This could leave a fluorine deficient environment for UF_6 recombination, resulting in the precipitate of UF_5, for example. There remains a need to chemically identify the precipitate and better understand the photochemical reaction that creates it [24].

The initial observations during this research were that the 38.103% sample chamber could not be reduced to as low a pressure as the other un-fogged sample chambers under cooling even prior to the fs-LIBS-induced reaction. After the initial fs-LIBS investigation where the precipitate formed, the 38.103% sample chamber was only able to achieve 20.1 Torr as its lowest pressure during the remainder of this research.

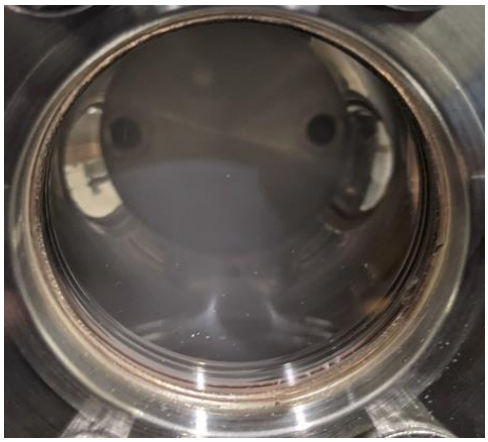
The precipitate was not evenly distributed in the sample chamber. Unfortunately, the fogging or cloudiness appears mostly on the collection window of the 38.103% sample, with little on the laser exit window, and very little on the laser entry window. The precipitate is not totally static once formed. During the testing conducted for this work there were slight variations in the distribution and intensity of the precipitate on the sample chambers.

The weaker, less persistent plasma associated with fs-LIBS has made achieving an acceptable SNR challenging and in the case of the 38.103% sample the precipitate fogging of the collection window forced a reduced test plan for the sample, which focused primarily on the HPHP testing configuration where there was less difficulty achieving reasonable SNR and where the most accurate assay measurements were achieved. Fortunately, the HPHP configuration yielded a bright enough plasma that this sample could be tested with exposure times adjusted to overcome the occluded collection window.

0.287% Entry Window 7/29/21



0.287% Collection Window 9/2/21



18.525% Entry Window 7/29/21



18.525% Entry Window 7/29/21



4.615% Collection Window 7/29/21



61.740% Collection Window 7/29/21



Figure 4.15. Precipitate deposition on sample chambers other than 38.103%

Spectral fits of the 38.103% sample spectra are shown in Fig. 4.16. As in the previous section, the spectral fits shown are selected from the best performing delay and gate width shown in Table 4.14 based on their accuracy to the actual assay of the sample. In the single test in the LPLP configuration reported in Table 4.14 the error from the ORNL reported value is actually lower than any other sample from that testing configuration. The standard deviation for the 38.103% sample measured in the LPLP configuration fell in the lower range of the standard deviations observed during the LPLP testing configuration for the rest of the samples.

The 38.103% sample measurements achieved accuracy and precision similar to the other samples in the HPHP testing configurations. The 38.103% sample did not yield as accurate an assay measurement as the other samples in the kinetic series measurements. The 38.103% sample measurements' standard deviation in the kinetic series were worse than all but the 61.740% sample. The measurement results are sufficiently close that more testing will be needed in future work to determine if the presence of the precipitate preferentially absorbs one isotope or if it is simply absorbing the plasma emission more or less evenly across the spectrum.

HOGSVD and DTW

One of the goals of this research is to identify opportunities for advanced SVD techniques to aid in the analysis of LIBS spectra for the purpose of determining assay. There are two primary applications where advanced SVD techniques are tested for potential benefit. One application explores the potential of advanced SVD techniques to make a determination about the assay associated with a UF_6 spectrum. This effort is important because it offers the potential to make determinations about assay without the detailed isotopic shift information required by MVNLSF. The other application of advanced SVD uses advanced SVD to identify candidate isotopic shifts that may enhance the assay measurement capability of multivariate spectral fitting approaches.

HOGSVD for Initial Assessment of Assay

Looking back at the HOGSVD formulas shown in (5), (6), and (7), we see that the X matrix is identical in each factorization. Finding the shared matrix X is the key to computing HOGSVD. Fortunately, there is a tractable algorithm which computes X by the eigenvalue decomposition of a single matrix *S* obtained by combining the input matrices in an appropriate way.

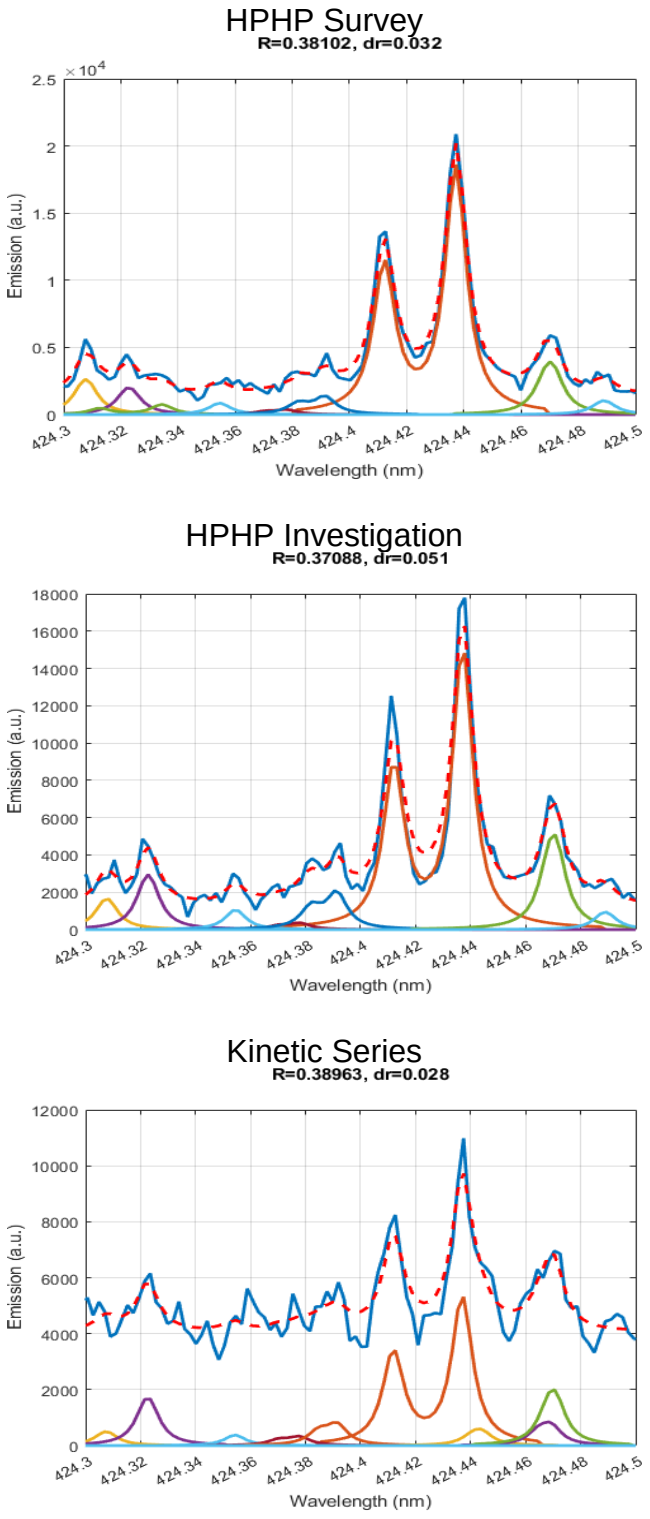


Figure 4.16. Spectral Fits for 38.103% Sample

Table 4.14. 38.103% Sample Results

38.103% ORNL Reported U-235 Enrichment	LPLP Survey	HPHP Survey 1	HPHP Survey 2	HPHP Invest. 1	HPHP Invest. 2	Kinetic Series
Delay and Gate Width (ns)	233-183	1208-333	1208-333	1708-1838	938-1033	1720-300
MVNLSF Calculated U-235 enrichment	37.97%	38.26%	38.74%	37.87%	37.54%	39.16%
Error from ORNL Reported Enrichment	-0.13%	0.16%	0.64%	-0.24%	-0.56%	1.06%
Standard Deviation	1.76%	0.81%	0.93%	2.36%	2.63%	3.72%
Relative Standard Deviation	4.6%	2.1%	2.4%	6.2%	7.0%	9.5%
RMSE	1.76%	0.75%	1.06%	2.13%	2.42%	3.49%
Mean Absolute Error	1.23%	0.55%	0.93%	1.80%	2.18%	3.07%

The X matrix is obtained from the eigen system shown in (12) and the decomposition shown in (13) [95, 97].

$$S\,X = X\,\Lambda \tag{12}$$

$$S = X\,\Lambda\,X' \tag{13}$$

The definition of the *S* matrix is subtle, but essentially it contains arithmetic averages for combinations of the decomposed matrices [95, 97]. Although the *S* matrix is not symmetric, it is proved that it has valuable properties of being square, real, with independent eigenvectors, and it has real (not complex) eigenvalues contained in Λ [95, 97]. Further, the eigenvalues of *S* have properties which are key to this investigation:

- They are always equal to or larger than 1[97].
    - The eigenvalues close to 1 correspond to eigenvectors in X that define a common subspace shared by all the original A matrices, which are fs-LIBS spectra collected from the UF6 samples [97].
- There is no upper bound to the eigenvalues [97].
    - Λ values much larger than 1 correspond to eigenvectors in X that distinguish at least one pair of the input matrices from each other [97]. Mathematically, the actual projection directions are the rows in the inverse matrix X^{-1}.

Given that there is no upper bound to the Λ values, the inverse ($1/\Lambda$), meaning the reciprocals of the diagonal elements of Λ, is used to aid visualization and interpretation. The $1/\Lambda$ values are bounded between 0 and 1. The $1/\Lambda$ values that are close to 1 still correspond to eigenvectors in X that define a common subspace (all the matrices have the same value of oriented energy when projected in a corresponding row-vector direction in X^{-1}). The $1/\Lambda$ values that approach 0 are those that now correspond to eigenvectors in X which define a distinguishing subspace. The plots of $1/\Lambda$ differ when comparing different assays and this variation can provide an initial assessment of the assay which can then be used as a guide for setting the starting values for a curve fitting algorithm such as the MVNLSF-type assay measurements conducted in this research. Additionally, parameters extracted from the plots of $1/\Lambda$ can be used as numerical representations of the likely assay of a spectrum. Fig. 4.17 illustrates how the plots of $1/\Lambda$ can illustrate the degree to which two spectra are similar and/or the degree to which they differ. In Fig. 4.17 the spectral average of multiple 0.287% samples is the reference spectrum to which the spectra of the assays listed above the plots of $1/\Lambda$ are being compared. The assays increase from left to right in both the upper and lower series.

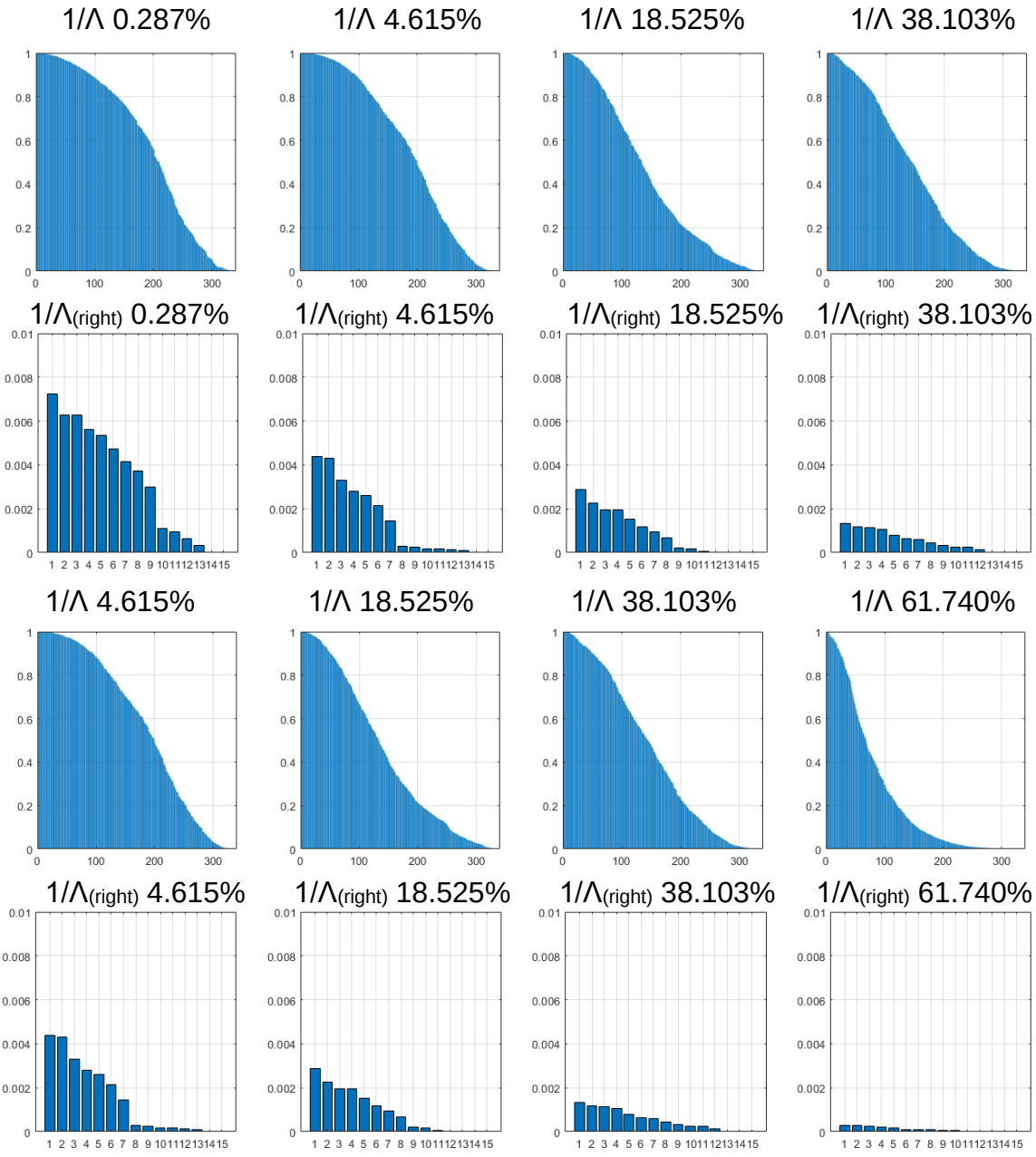


Figure 4.17. Plots of 1/Λ for 317 eigenvalues of *S* between 2 spectra and plots of the right-most 15 eigenvalues of *S* ($1/\Lambda_{(right)}$) to provide an indication of assay relative to the 0.287% reference spectrum.

In each of the plots included in Fig. 4.17 the vertical axis reports the $1/\Lambda$ values and the horizontal axis is the eigenvalues of *S* ordered from greatest to least. The ordering does not correspond to the wavelength in a spectrum. Note that in the upper left of Fig. 4.17 a 0.287% spectrum has been compared with the reference spectrum. This $1/\Lambda$ plot has a mostly convex shape indicating commonality between the spectra. Note also the two upper right $1/\Lambda$ plots. It appears that the plot associated with the 18.525% sample is less convex than that of the 38.103% sample. However, additional information is contained in the 2 plots immediately below reporting the right-most $1/\Lambda$ values, which are noted as $1/\Lambda_{(right)}$. The right-most portions of the $1/\Lambda$ plots are the regions where the distinguishing characteristics are reported. Here the differentiation between the 18.525% sample and the 38.103% sample is clearly observed with the 18.525% sample having larger $1/\Lambda_{(right)}$ values indicating more commonality with the 0.287% reference spectrum than the 38.103% spectrum shares. The bottom right plots of Fig. 4.17 show the highest assay sample, 61.740%. The difference is clearly shown where the $1/\Lambda$ plot is concave in appearance and the $1/\Lambda_{(right)}$ values are extremely small.

Factors related to the behavior of the $1/\Lambda$ values, such as the average, median, and skewness combined with similar factors related to the right-most, $1/\Lambda_{(right)}$, and left most, $1/\Lambda_{(left)}$, portions of the $1/\Lambda$ plot have great potential to offer densely packed information related to the likely assay of an unknown spectrum.

PCHIP Alignment of the Wavelengths in the A Matrices

The advanced SVD methods such as HOGSVD are applied to matrices. The columns in the A matrices shown in (5), (6), and (7) correspond to discrete wavelengths. Not only must all of the A matrices have the same number of columns but corresponding columns must represent the same wavelength in each of the A matrices. This can be accomplished through calibration of the of the pixel columns to individual wavelengths for all of the spectra collected in a data collection campaign. However, in this research, the data set had been collected over a period of months and in different testing configurations. Therefore, the pixel columns could not be relied upon to represent the same exact wavelength from one test to the next because of expected system error from temperature effects on the optical components and mechanical slack for the adjustable components within the spectrometer.

To align the columns of each of the A matrices to represent the same wavelengths, PCHIP in MATLAB was employed. Each of the wavelengths associated with columns of each of the A matrices were combined into a single ordered list. Based on the number of data points needed for the analysis, the selected number of wavelengths were taken from the vector of the ordered list of wavelengths.

If the A matrix being calibrated lacked the exact wavelengths in the down-selected ordered list, the datapoints in the A matrix are interpolated to provide wavelength values only at the down-selected ordered list of wavelengths which will be used in each of the spectral calibrations. This is repeated for every A matrix. At the end of this process, corresponding columns in the A matrices represent the same wavelengths in the spectrum.

Bootstrapping and other Advanced SVD Considerations

HOGSVD techniques require more samples or rows in the A matrices than columns to assure stability of the numerical algorithms [99]. There is no requirement that all the A matrices have the same number of rows, and full-column rank is not required as of 2021 [99]. The practice in this research has been to have approximately 10 times as many rows as columns.

The requirement for this large number of samples relative to the number of discrete wavelengths is a challenge when collecting data from LIBS processes. Bootstrapping is a technique in statistical sampling that can be applied to create additional representative samples [124]. The bootstrapped samples can be used to fill out the rows needed in the A matrices for the advanced SVD processes to work. Bootstrapping is not new to LIBS processes, although there is no indication that it has been used with LIBS spectra for the purpose of applying HOGSVD. Képeš et. al applied bootstrapping to LIBS spectra of archaeological samples and concluded that the collection of single-shot spectra with subsequent application of bootstrapping offered better signal stability than multi-shot accumulations and reduced standard deviation without significantly affecting the mean signal value [125].

The standard description of bootstrapping begins with a fixed number of samples, S, of a random variable, X, assumed to consist of independent and identically distributed random variables. Each bootstrap sample of this original data set is created by a random drawing of the values in the sample set, S, with replacement [124, 126]. Replacement means that the drawn sample goes back into S, so that it may be drawn again. The random drawing continues until there have been as many values of S drawn as were present in the original dataset. This is considered a bootstrap sample, but it does not preserve any ordering from the original dataset and therefore it is not a method that should be applied to spectra.

Bootstrapping of spectra requires that the left-to-right ordering of the original collected data must be preserved [127]. The bootstrap samples of the spectra in this research are created using the following process: for each of the n data points in the spectrum a new sample of the same, n, length will be created.

There will be 0, 1, or 2 occurrences of each data point from the original spectra in the new bootstrapped sample. The expected number of occurrences of each datapoint is 1. There is an equal chance that each datapoint from the original sample will occur only once or not at all in the bootstrap sample. Note in Fig. 4.18 that there are two scenarios where the value 'B' occurs once in the n and n+1 combinations shown, but there is only one scenario where the 'B' occurs twice or not at all. In essence this collection of bootstrapped samples of the original spectrum models very limited jitter in sampling the data and creates samples that are statistically typical to the original.

This approach of bootstrapping additional samples preserves the left to right ordering of the data points, does not fundamentally alter the data that is being analyzed, and produces the samples necessary to allow advanced SVD approaches to be used for exploratory data analysis of the fs-LIBS spectra that have been collected.

Explanation of the HOGSVD-DTW Dataset

Testing HOGSVD's ability to provide an assessment of assay requires establishing a dataset from which training, reference, and test data can be extracted. The HPHP investigation data was selected for this purpose since it provided a good combination of SNR as well as an ample supply of spectra collected from very early in the plasma life to very late.

Additionally, the HPHP investigation data includes all five sample assays; 61.740%, 38.103%, 18.525%, 4.615%, and 0.287%. For each assay 270 spectra were included. Each of the 270 spectra datasets consisted of 10 repetitions of the same delay and gate width beginning with a delay of 75 ns and a gate width of 83 ns and ending with a delay of 1708 ns and a gate width of 1838 ns. Table 3.3 lists the 27 delay and gate width combinations included in this data range.

The spectra were each created from the ICCD's image file using the precision calibration process described in Chapter 3. The detector offset was subtracted from each pixel of the image based on the median emission intensity reported by the top 30 rows of the ICCD's detector. This region of the ICCD did not receive incoming light from the fiber optic cable and is a good representation of the detector offset.

After the calibrated spectra were incorporated in the dataset, the dataset was normalized so that the emission intensities range between 0 and 1. The calibration process applied to each spectrum assigns wavelengths to each data point from the ICCD based on the location of 3 prominent peaks in the uranium spectrum.

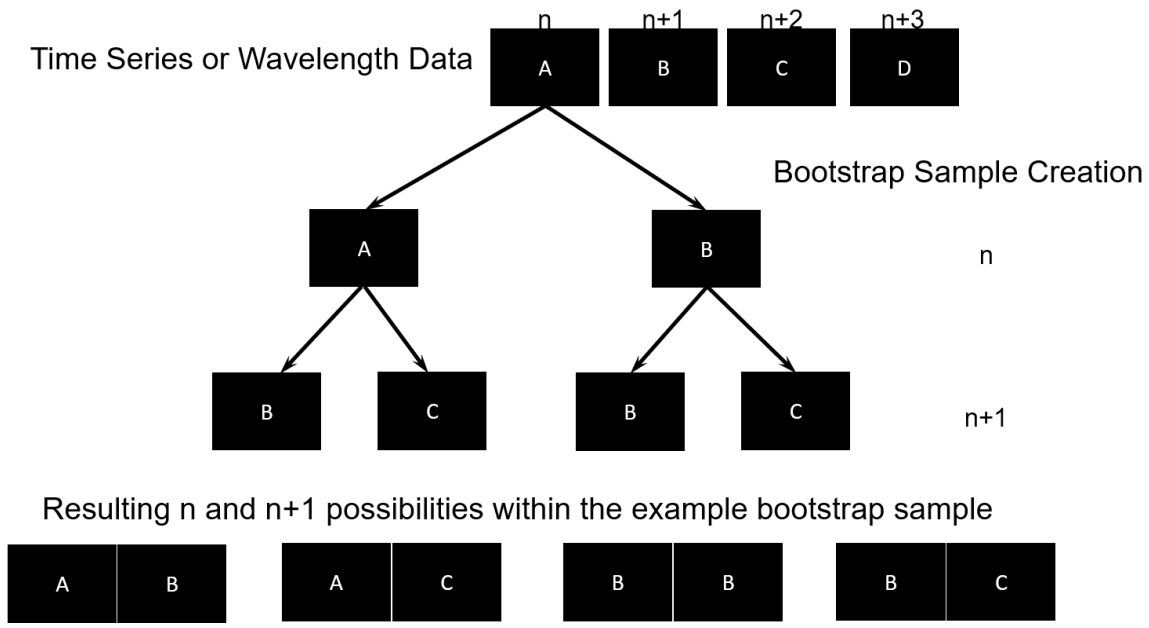


Figure 4.18. Illustration of Bootstrap Sample creation

To align the spectra so that they all have the same wavelength data points, a representative set of wavelengths was selected and each spectrum was interpolated to report values at those wavelengths using PCHIP. The use of PCHIP to align these spectra is justified since a spectrometer and ICCD could be calibrated at the beginning of a continuous data collection campaign so that each pixel column would represent the same wavelength for any spectrum captured during that campaign, but in this case the spectra were collected over a period of months in numerous data collection campaigns. The Bootstrap technique was applied to each of the 1350 spectra in the dataset to produce 2000 theoretically sound statistical samples based on the original spectra. The Bootstrap samples represent the data that could be coming in from an fs-LIBS system performing continuous monitoring of a GCEP process line.

In essence the PCHIP alignment and Bootstrap technique was performed to allow this dataset to more closely replicate the data that would be collected from a continuously operating fs-LIBS collection system installed and operating in a monitored foreign enrichment facility or in a commercial enricher's continuously operating production facility.

Assay Classification through Pattern Recognition with HOGSVD and DTW

HOGSVD combined with DTW provide an opportunity to make assessments of the approximate assay that a spectrum most closely matches. Both HOGSVD and DTW have been tested during this research to determine if the numerical feature information that they provide about unknown-assay spectra can be used to aid in the determination of assay through what is essentially a classification problem; unknown spectra are evaluated with HOGSVD and DTW and that spectrum can be classified based on the spectra in a training dataset that it most closely matches.

The MATLAB graphical user interface, *ClassificationLearner*, is used to build a model to evaluate the potential benefit of using summary information from HOGSVD and DTW to make a classification determination about what assay material a test spectrum of unknown (to the model) assay belongs to. The HOGSVD-DTW dataset described above provides the training, reference, and test data for this experiment. For the classification model the assays themselves are the class to which they belong.

The HOGSVD-DTW dataset is partitioned into two separate datasets **TA** and **TB** for each of the five classes, as shown in Fig. 4.19. The training dataset **TA** (left side of Fig. 4.19) is further partitioned into disjoint subsets for two reasons. First, DTW **(WC, WR)** optimally aligns two signals and returns a single Error number. Samples of these DTW Errors are needed to train the classification algorithm.

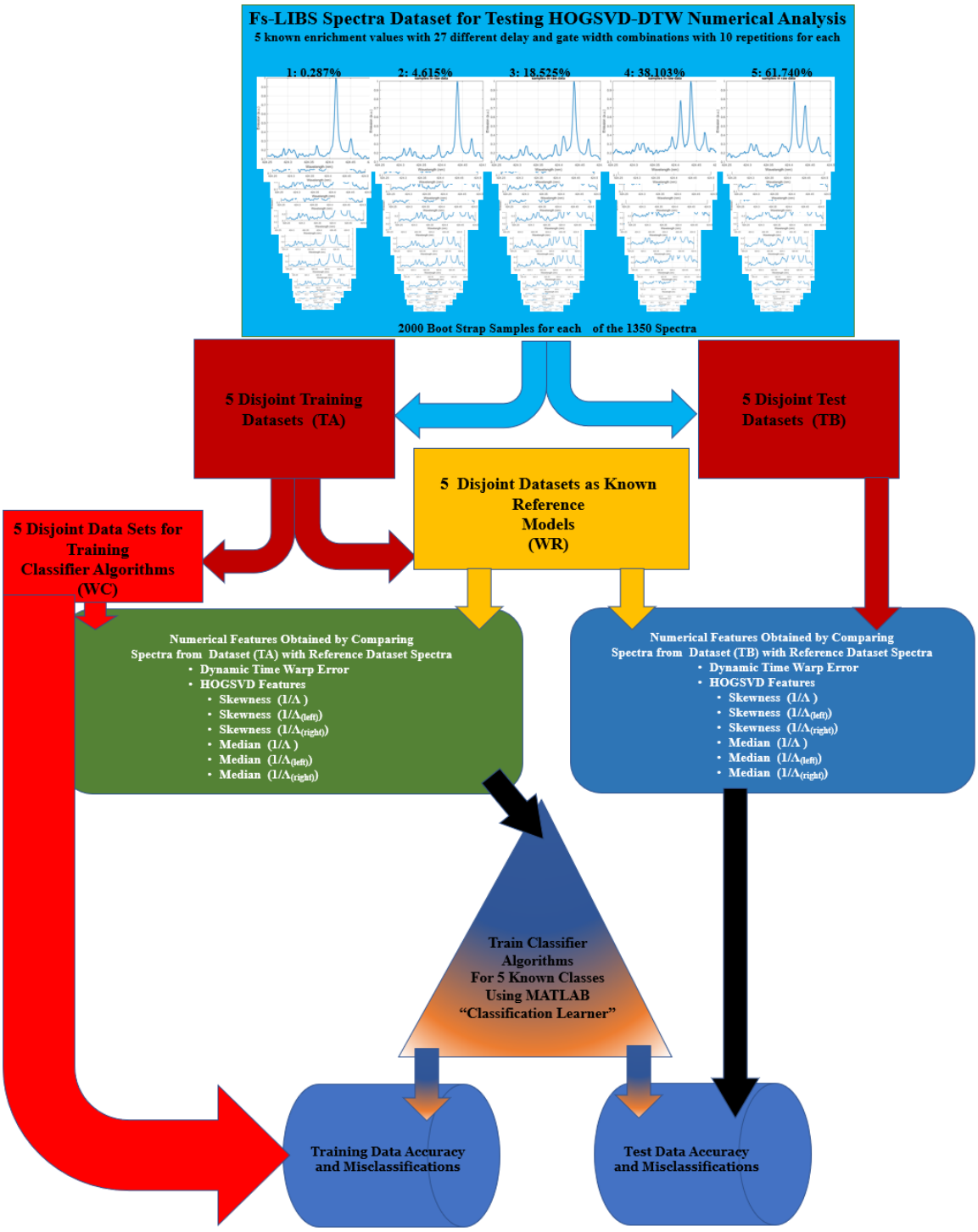


Figure 4.19. Diagram of the Assay Classification Experiment using HOGSVD-DTW features about unknown-assay spectra to make a determination about the assay most closely matching in the training data.

The algorithm also requires the DTW Error where candidate spectrum **WC** is optimally aligned with reference spectrum **WR** for the same class to establish within-class variation. Variations between different samples in the same class cause this within-class DTW Error to be bigger than 0. Second, HOGSVD (**WC, $\mathbf{WR_i}$**) compares a candidate matrix **WC** with a reference matrix **$\mathbf{WR_i}$ for** class *i=1,2,3,4,5.* The class is equated to assay:

- 1 – 0.287%
- 2 – 4.615%
- 3 – 18.525%
- 4 – 38.103%
- 5 – 61.740%

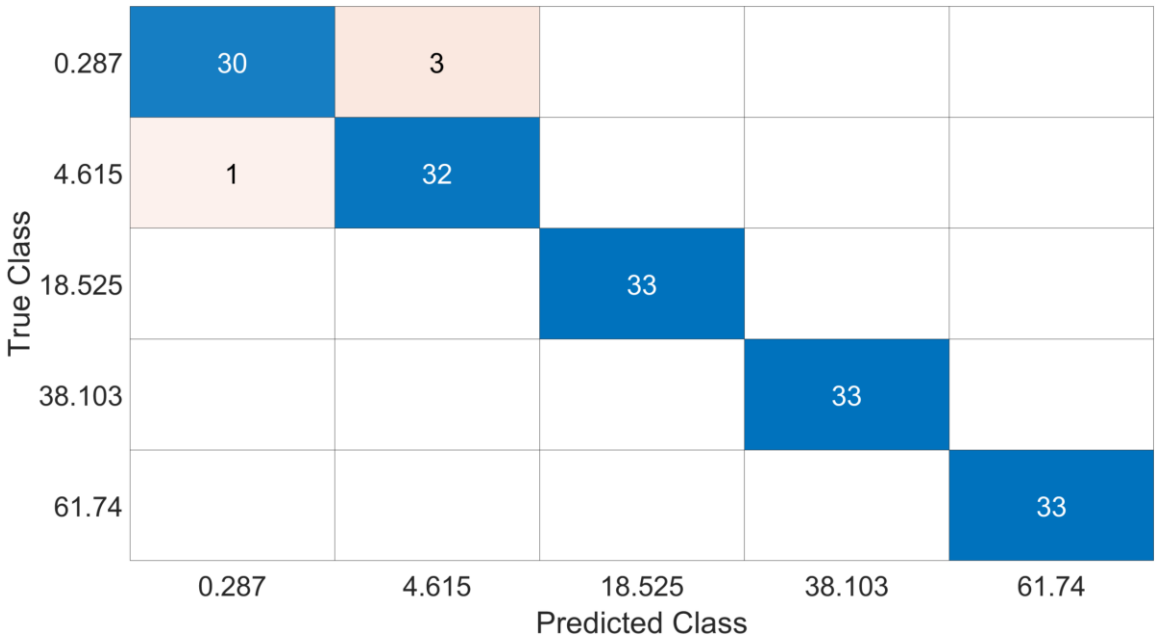
Numerical features of the distribution of the HOGSVD eigenvalues for **WC** compared to the references **$\mathbf{WR_i}$** are used in training the classification algorithm. This, similarly to DTW, includes samples **WC** for a class compared to disjoint samples **WR** for the same class, and thereby gives a reference eigenvalue distribution representing the within-class variation. The training dataset must be partitioned into disjoint samples **WC** and **$\mathbf{WR_i}$** to compute these reference eigenvalues Λ.

ClassificationLearner is used to run a suite of numerical algorithms using **TA** as training data to compute parameters for each candidate algorithm. The classification algorithm with the lowest misclassification rate on **TA** is adopted, and the dataset **TB** is analyzed with the algorithm for comparison of confusion matrices and miscalculation rates. To further test the approach, the roles of **TA** and **TB** are swapped and the evaluation is repeated. An example of the confusion matrix for a model trained and tested in the manner illustrated in Fig. 4.19 is shown in Fig. 4.20.

Numerical Features of Spectra Based on HOGSVD and DTW

The features that are used when testing the performance of HOGSVD-DTW or DTW by itself are not spectra. They are numerical features obtained by computing HOGSVD and DTW on samples of spectra. Both DTW and HOGSVD require a reference spectrum **WR** to which to compare a candidate spectrum **WC**. DTW aligns **WC** with **WR** by shifting datapoints in **WC** and/or **WR** locally by small amounts to minimize the overall error while preserving the left-to-right ordering of all the datapoints [100]. The numerical value of the DTW Error is computed for **WC** aligned with **$\mathbf{WR_i}$** where **$\mathbf{WR_i}$** is one of the five references (or training data) for the five classes *i=1,2,3,4,5*.

Confusion Matrix for Classification Algorithm Applied to Training Data



Confusion Matrix for Classification Algorithm Applied to Test Data

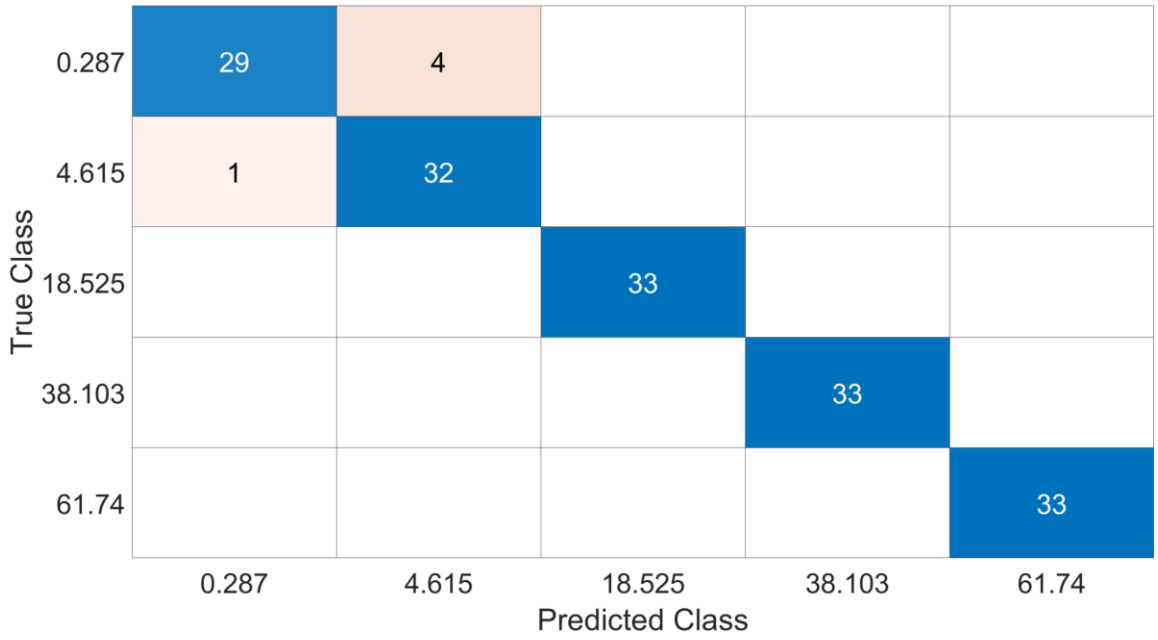


Figure 4.20. Confusion Matrices for MATLAB *ClassificationLearner* algorithm classifying HOGSVD-DTW features about unknown spectra to the assay class they most closely match.

The generic properties of the eigenvalues computed by HOGSVD (**WC, WR$_i$**) for bootstrapped samples of **WC** and **WR$_i$** give additional numerical features**.** As previously discussed, the eigenvalues λ are never less than 1, so that 1/λ is in the range 0 to 1. Further, values of λ (and 1/λ) close to 1 identify vector directions that are common to the two matrices, meaning that the oriented energy ratios are close to 1. If **WC = WR$_i$**, then all the eigenvalues are equal to 1. If **WC** and **WR$_i$** are totally dissimilar when scanned from left to right, then every eigenvalue is bigger than 1.

In other words, large values of λ (and corresponding small values of 1/λ close to 0) identify vector directions that are not common to the two matrices but instead distinguish or isolate one matrix from the other because one oriented energy exceeds the other oriented energy. The closer 1/λ is to 0, the more the oriented energies are out of balance and the more the associated vector direction distinguishes one matrix from the other. In summary, **WC** is numerically similar to **WR** if there are many values 1/λ close to 1, and vice versa, **WC** is numerically not similar to **WR** if there are many values 1/λ close to 0.

The DTW-error comes directly from the optimal alignment of the spectra. The HOGSVD features are extracted from the 1/ Λ plots, which are defined empirically by considering the known mathematical characteristics of the HOGSVD eigenvalues. The results of using the five numerical features from HOGSVD and DTW are shown in Table 4.15. The numeric features are:

- Dynamic Time Warp Error
- HOGSVD Features from 1/Λ
    - Skewness (1/Λ)
    - Skewness (1/Λ$_{(right)}$)
    - Median (1/Λ)
    - Median (1/Λ$_{(left)}$)

Classification experiments can be run using DTW-error alone, without including the HOGSVD features in the classification algorithm. However, as shown in Table 4.15, the accuracy improves when HOGSVD features are included. The lower misclassification rates and improved accuracy when applied to the same dataset imply that there is structural information in the HOGSVD features not present in the DTW-error alone.

Additionally, it is noteworthy that the majority of misclassifications in the testing completed to produce Table 4.15 occur in the 0.287% and 4.615% samples where the spectral differences between the two are minimized and, of course, the assay difference between 0.287% and 4.615% is roughly a quarter the difference between the other samples.

Table 4.15. HOGSVD-DTW Classification Experiment Results

Features Used in the Classification Algorithm	Test Data Bounded / Unbounded by Training Data	Average Accuracy of the Classification Algorithm	Average Misclassification Counts	Accuracy Lost Relative to Spectral Data
Spectra	Bounded	98.5%	2.5	
HOGSVD-DTW	Bounded	95.15%	8	3.35%
DTW only	Bounded	92.1%	13	6.4%
Spectra	Unbounded	91.1%	28	
HOGSVD-DTW	Unbounded	88.68%	36.75	2.43%
DTW only	Unbounded	82.13%	57.5	8.98%

Applying HOGSVD-DTW Numerical Values in Estimating Assay for Unknown Samples

The complexity of applying an MVNLSF assay measurement technique motivates additional research into the alternatives offered by advanced numerical algorithms. If samples are obtained with unknown assays not necessarily equal to one of the five samples for which data is available in this research, then the problem is more challenging than classification into one of five known classes. Initial results are reported here for using the HOGSVD-DTW numerical values in training an assay estimation algorithm for an unknown sample.

There are numerous numerical algorithms for interpolation, extrapolation, and estimation of unknown values from an observed sample of numerical data. MATLAB has many, and all of them require training datasets to tune their internal parameter values (or predictor variables) for the application. In practice, the number of input variables (or numerical features) in the training data should be small due to algorithm complexity and potential numerical instabilities [128]. After training, the input sample is called the query point for which the unknown value (or response variable) must be estimated [128].

A state-of-the-art method is *Multivariate Adaptive Regression Splines* for adaptive modelling of multi-dimensional data by linear or cubic splines [129]. The method is implemented in a downloadable toolbox for MATLAB called *ARESLab* (Adaptive Regression Splines) [128]. The toolbox includes functions (1) **aresbuild** to build a splines regression model from training data and (2) **arespredict** to predict the unknown (response) value for a query point using the trained ARES model [128].

The first test toward true unknown assay measurement is a demonstration of the effectiveness of the ARES algorithm for what is essentially still classification of a sample into one of the assay values in the training data, comparable to the experiments using MATLAB *ClassificationLearner* and run on the identical datasets. The training and test data have samples of HOGSVD-DTW feature vectors from all five assays, and the predicted or response variable is an assay. For feature vectors using all the numeric features listed in Fig. 4.19:

- The ARES model is built by **aresbuild** using training data vectors with known assays
- The training data and disjoint test data are input sample by sample using **arespredict** which returns the predicted value as an assay.

The assay prediction performance is shown in Fig. 4.21 using the HOGSVD-DTW features described in the assay classification experiment.

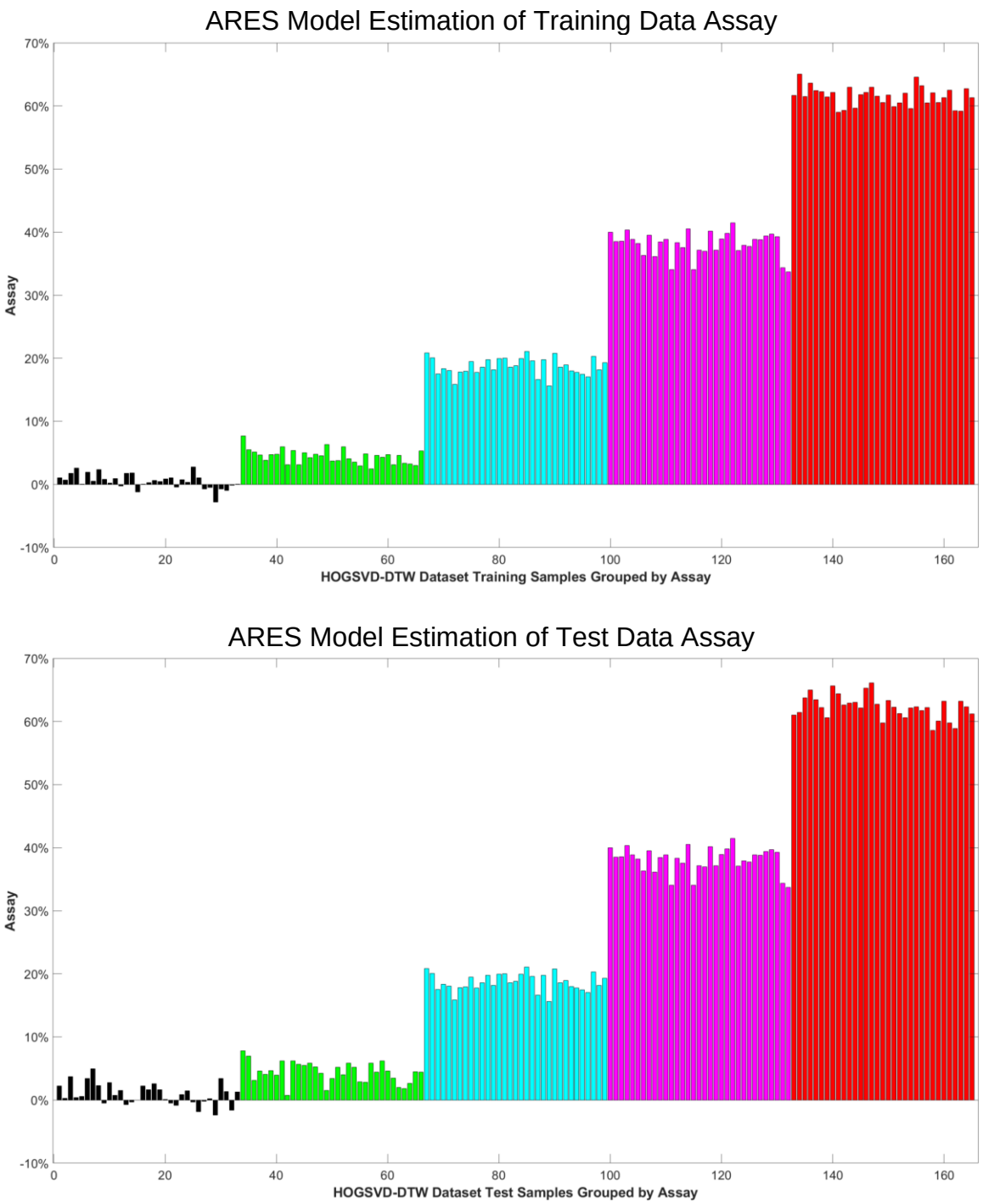


Figure 4.21. Assay estimations using an ARES model which includes training data for all the assays tested.

It should be emphasized that the algorithms in MATLAB *ClassificationLearner* do not predict a response variable value. They assign a candidate sample its “best class label’’ by their respective numerical criteria. By contrast, ARES builds a numerical model of the training data that predicts a “best numerical value’’ for an input query point by its optimal spline-fitting criteria [128]. That predicted number does not have to be one of the training data assays.

To study the potential of the ARES method for estimating unknown assay values, an ARES model must be built from data with known but incomplete assay values using **aresbuild** and tested with data with additional known assays using **arespredict**. Predicting an assay which can be any real number requires much more information-rich splines than estimating an assay class based on training data. The results shown in Fig. 4.22 are an encouraging proof-of-concept, but performance at an acceptable applications level is future work.

Fig. 4.22 compares the performance of the ARES model built with the HOGSVD-DTW features on the left-hand side with an ARES model built with the spectral data from the HOGSVD-DTW dataset on the right-hand side. In the first comparison at the top of Fig. 4.22, the 4.615% spectra were missing from the training data. Note that the HOGSVD-DTW feature model does a better job of predicting assay for the 4.615% samples, but the missing 4.615% training data has had an impact on the HOGSVD-DTW model’s ability to predict the 0.287% sample assay correctly. The middle row of graphs in Fig. 4.22 shows the results of both models lacking the 38.103% sample spectral training data. In this case the HOGSVD-DTW model does a poorer job of predicting the missing samples assay than the model based on the spectral data, but the HOGSVD-DTW model has quite accurate and consistent results for the 61.740% sample measurements, whereas the spectral-data-based model has greater variability for the 61.740% sample measurements even though these spectra were included in the training data. The bottom row of plots in Fig. 4.22 is quite interesting in that the HOGSVD-DTW is able to do a fair job estimating the assay for incoming 61.740% samples even though they were not included in the training data and, in fact, are an extrapolation of the training data. The spectra-based model has significant difficulty extrapolating measurements for the incoming 61.740% samples.

HOGSVD for Identification of Candidate Isotopic Pairs

Key to determining MVNLSF-calculated assay of a UF_6 based on a collected spectrum is knowledge of the isotopic shifts that can be observed and measured. This use of HOGSVD has not been demonstrated in the literature, so a goal of this research became attempting to obtain information about the importance of individual wavelengths in discriminating one assay spectrum from another.

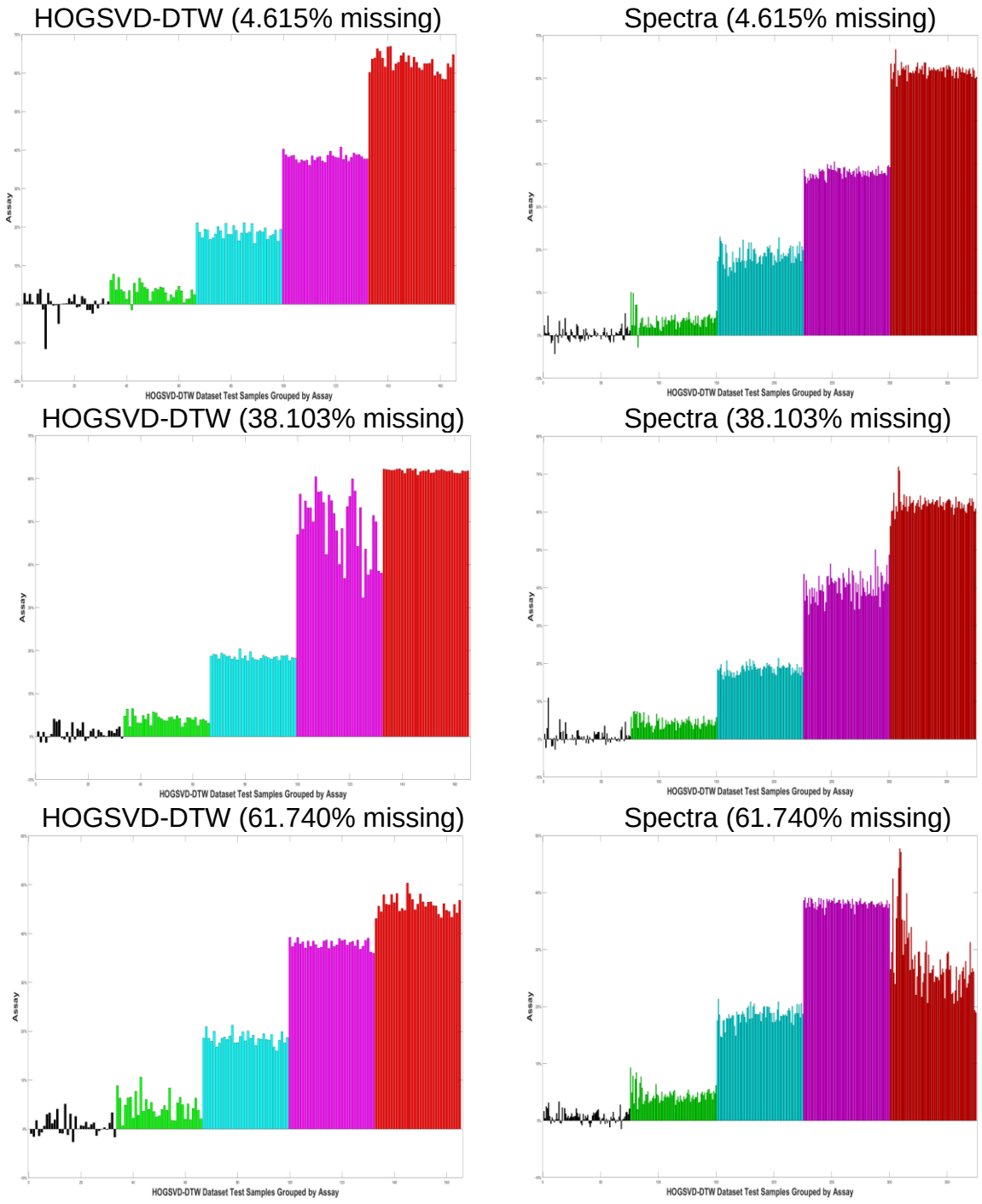


Figure 4.22. Results of ARES models estimating assays based on training data that does not include the full range of assays in the test data.

The importance of the wavelengths for distinguishing one spectrum from another can be used as a guide to aid identification of candidate isotopic shifts which might benefit a MVNLSF-type approach to assay measurement. HOGSVD can provide this information. In the application of HOGSVD to digital processing of fs-LIBS spectra, each column x_k of the shared X matrix (see (5), (6), and (7)) computed by HOGSVD ($A_1, A_2, \dots, A_n$) is characterized by its significance or relative information content for matrix A_i relative to matrix A_j by the generalized singular value shown in (14).

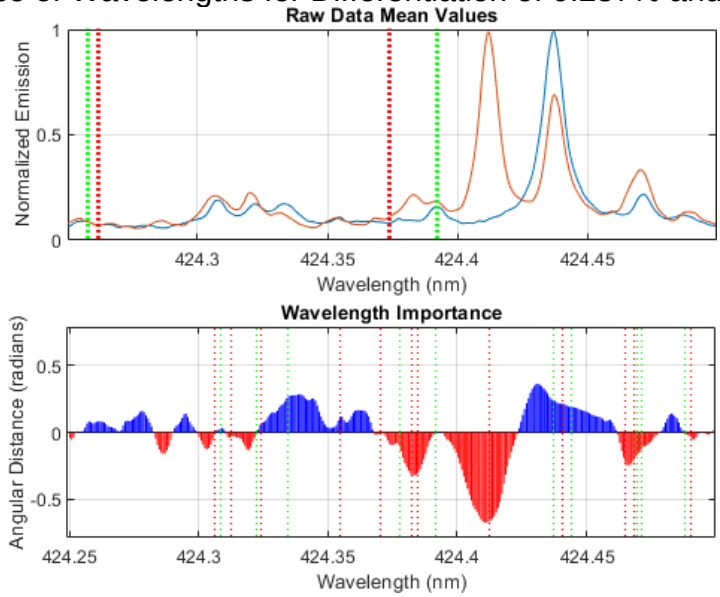
$$gs_{ijk} = \frac{s_{ik}}{s_{jk}} \tag{14}$$

Once the generalized singular value is squared, gs_{ijk}^2 is the oriented energy ratio for A_i relative to A_j when projected in vector direction x_k^{-1} in the inverse matrix X^{-1} [97, 130]. This decomposition also quantifies the importance of the columns, which are our wavelengths, in the data matrices in these vector projection directions [130].

There are some important properties of HOGSVD that are leveraged in this importance-of-wavelength application. The generalized singular value $gs_{ijk} = 1$ identifies a vector direction index *k* of equal significance to the data matrices A_i and A_j [97, 130]. Additionally, an extreme (largest or smallest) value of the generalized singular value gs_{ijk} identifies the index *k* of a vector direction that maximizes or minimizes the oriented energy ratio [97, 130]. Further, it has been proven in the literature developing HOGSVD that these extreme directions are optimal and cannot be improved further [97, 130]. In the importance-of-wavelength application, this means that the wavelengths that have relatively high importance in a vector direction index *k* which attains the maximum generalized singular value gs_{ijk} contain the most information which distinguishes spectrum A_i from A_j. Conversely, wavelengths in a vector direction index *k* for which $gs_{ijk} = 1$ do not distinguish the two spectra when projected in direction x_k^{-1}.

This information is visualized in Fig. 4.23. The charts labeled Wavelength Importance are created by the generalized singular values gs_{ijk} in HOGSVD which are used to identify two of the HOGSVD-computed vector directions from the inverse shared matrix X^{-1}: the direction most favorable to the blue data (the highest oriented energy ratio blue/red) and the most favorable to the red data (the highest oriented energy ratio red/blue). The blue bar plot is the 339 biggest numerical values in the first vector plotted as positives and the red bar plot is the 339 biggest in the other vector plotted as negatives. Here 339 happens to be the number of data points that define these two spectra, but any number up to the number of data points can be used based on whatever level of discrimination between the two spectra is desired. These bar plots effectively illustrate the wavelengths importance in distinguishing one spectrum from another.

Importance of Wavelengths for Differentiation of 0.287% and 61.740%



Importance of Wavelengths for Differentiation of 4.615%and 61.740%

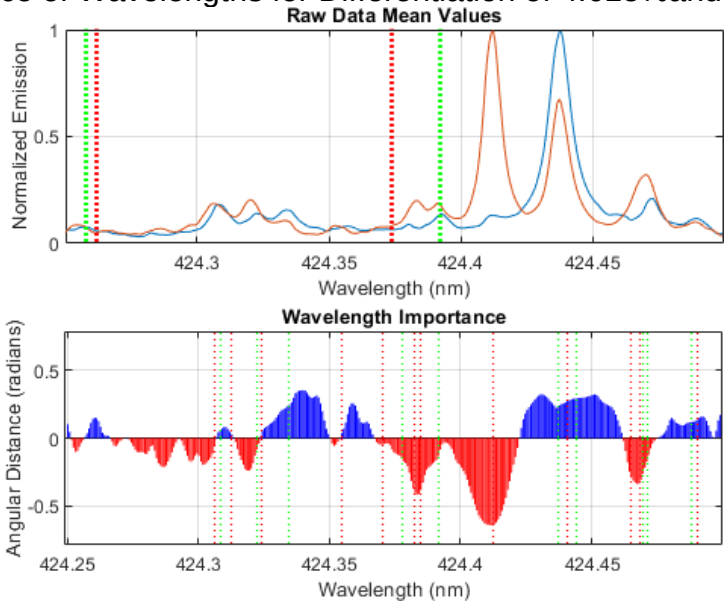


Figure 4.23. Importance-of-Wavelengths in differentiating spectra of different assay

There was a hope that the fs-LIBS process would yield some access to additional isotopic pairs that are not discernable in the plasmas produced by other lasers. Hundreds of charts similar to Fig. 4.23 were generated comparing fs-LIBS spectra. These charts could be quickly scrolled through while looking for areas where the red and blue bar plots indicated that the wavelengths in a region were useful in distinguishing the two spectra from one another and also areas where there were not already emission lines identified as part of the 12-pair MVNLSF approach [67]. The 12 isotopic pairs are shown in the Wavelength Importance graphs with thin red and green stem plots. The red corresponds to lines associated with ^{235}U and the green stem plot lines are associated with ^{238}U in Fig. 4.23. In the charts labeled “Raw Data Mean Values”, Fig. 4.23 shows the average value for each wavelength in the spectrum. The values are averages of the 2000 bootstrap-created spectra which fill out the datapoints in the matrices ($A_1, A_2, \dots, A_n$). The thicker stem plot lines in the graphs of raw data mean values are wavelengths that displayed recurring importance in many spectra for distinguishing one assay sample from another. The wavelengths identified were then compared against the spectral emission line database described in Chapter 3 looking for an isotopic shift that could be used to better fit the identified regions of distinguishing wavelengths.

Additional Isotopic Pairs for fs-LIBS

The additional isotopic shifts identified, using HOGSVD, as candidates for improving the assay prediction capabilities of fs-LIBS are from a 1959 United Kingdom Atomic Energy Authority report authored by E.W.T. Richards and M.D. Crew using a 21-foot spectrograph and measuring uranium optical emissions created using an interrupted AC arc and microwave discharge tubes.

Fig. 4.24 shows the resulting spectral fits associated with the most accurate MVNLSF 14 isotopic pair (MVNLSF-14) assay measurements in the rightmost column of graphs. Recall that this practice of selecting the most accurate assay measurement only applies to spectral fits and not the data reporting. The rows of graphs in Fig. 4.24 correspond to the sample chambers which experienced little precipitate formation: 0.287%, 4.615%, 18.525%, and 61.740% from top to bottom. The leftmost column of graphs shows the contribution to the spectral fitting from the 424.262 (^{235}U) – 424.258 (^{238}U) isotopic pair.

The Lorentzian Parameter reported above each graph refers to the A_i values from (10) which represent the areas of the spectral peaks. The center column of graphs in Fig. 4.24 is the contribution to the spectral fitting from the 424.374 (^{235}U) – 424.392 (^{238}U) isotopic pair. The blue stem plots present in both the left and center columns of graphs represent the edge of the *dr* range over which that isotopic pair will make a contribution to resulting spectral fit.

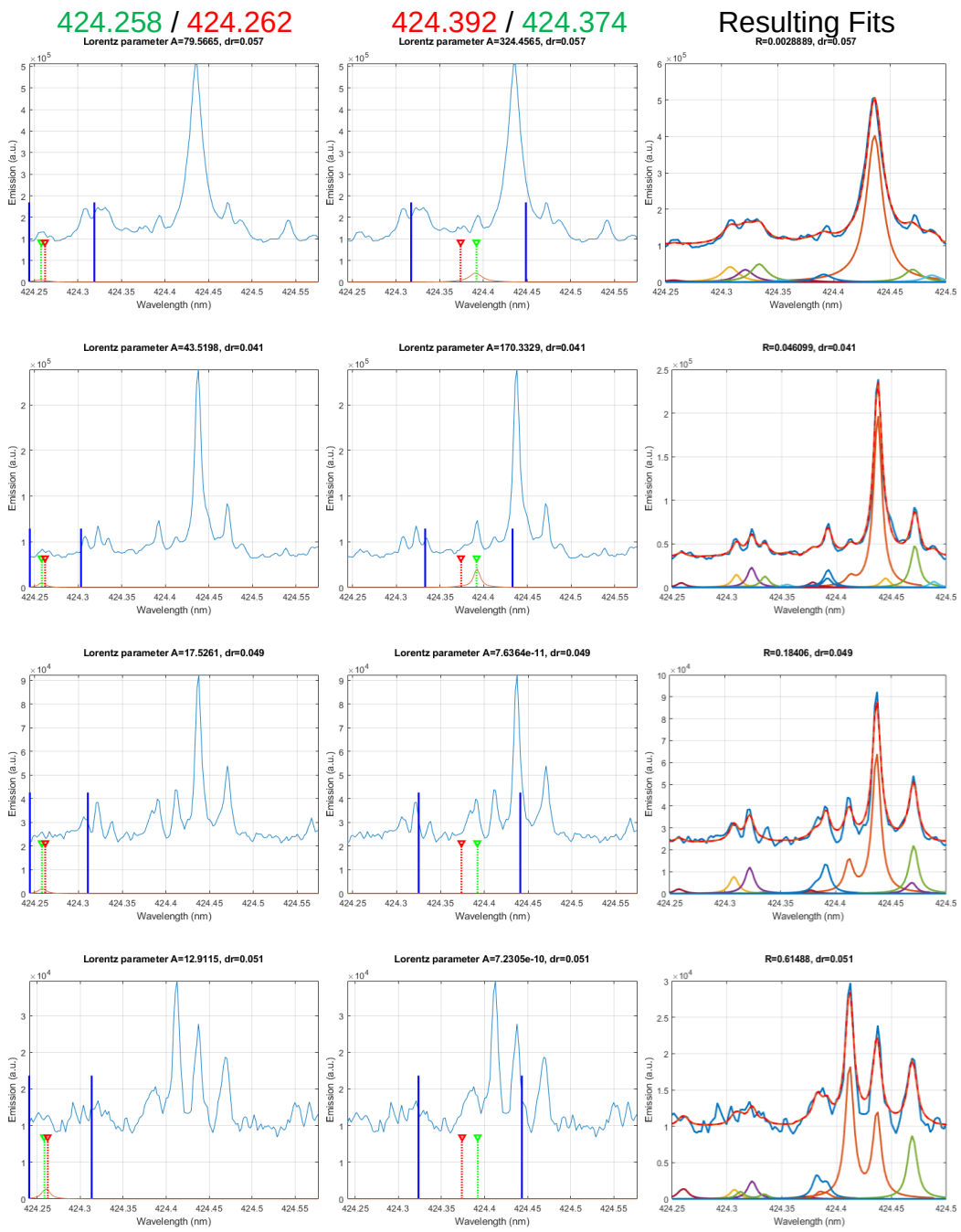


Figure 4.24. Improved SNR Kinetic Series Fits using Additional Isotopic Shifts

In Fig 4.24, as before, the red stem plots correspond to the ^{235}U isotopic pair emission and the green ones are the ^{238}U emission. Note that for both the 18.525% and 61.740% samples the MVNLSF-14 fitting algorithm is assigning A_i values of essentially 0. This occurs when the data that Lorentzian is attempting to fit does not agree with the expectation established by the dominant isotopic 424.4122 (^{235}U) – 424.4372 (^{238}U) shift. It is also important to note that as the SNR degrades, as in the case of the 18.525% and 61.740% samples, it is more likely that a less prominent isotopic shift will be zeroed out by the MVNLSF-14 fitting algorithm.

It is difficult when looking at only the most accurate spectra for any given test configuration to know whether the additional isotopic pairs provide additional value. To assess whether the MVNLSF-14 fitting algorithm enhanced the assay measurement capability of the fs-LIBS system, it was necessary to re-analyze all the collected spectra and re-analyze the assay measurement performance.

To summarize this data, the average assay measurement from every captured spectrum for each sample in each testing configuration was recorded and the error from the ORNL-reported assay measurement was calculated. The square root of the sum of the squares for each of these errors was calculated for each test configuration.

These summary values for both the 12 isotopic pair MVNLSF approach and the MVNLSF-14 algorithm are shown in Fig. 4.25. In all but two instances the error is reduced by use of MVNLSF-14. The results for LPLP Investigation 2 and HPLP Survey 1, show nearly identical reported errors with the 12 isotopic pair having a very slightly lower value.

The errors associated with the HPHP test configurations in Fig. 4.25 are relatively large in contrast to the reported accuracies thus far where HPHP data is the most accurate. Recall that the HPHP test configuration produced a brighter and more persistent plasma than the tests conducted at low pressure. To explore the potential value of emissions very late in the plasma life, up to four times as many spectra were collected in the HPHP testing configuration than in the LPLP and HPLP configurations. Many of these spectra were too late in the plasma emission to reach the SNR levels needed for accurate measurement.

The presence of the large number of spectra late in the plasma life is the cause of the apparent increase in the error magnitudes shown in Fig. 4.25 in the HPHP test configuration. It is also important to note that some of the largest differences in error magnitude occur in the HPHP investigation comparison of MVNLSF-12 versus MVNLSF-14. This is not necessarily surprising since the HPHP testing configuration produced spectral clarity that likely afforded the MVNLSF-14 fitting algorithm better opportunity to benefit from the two additional isotopic shifts.

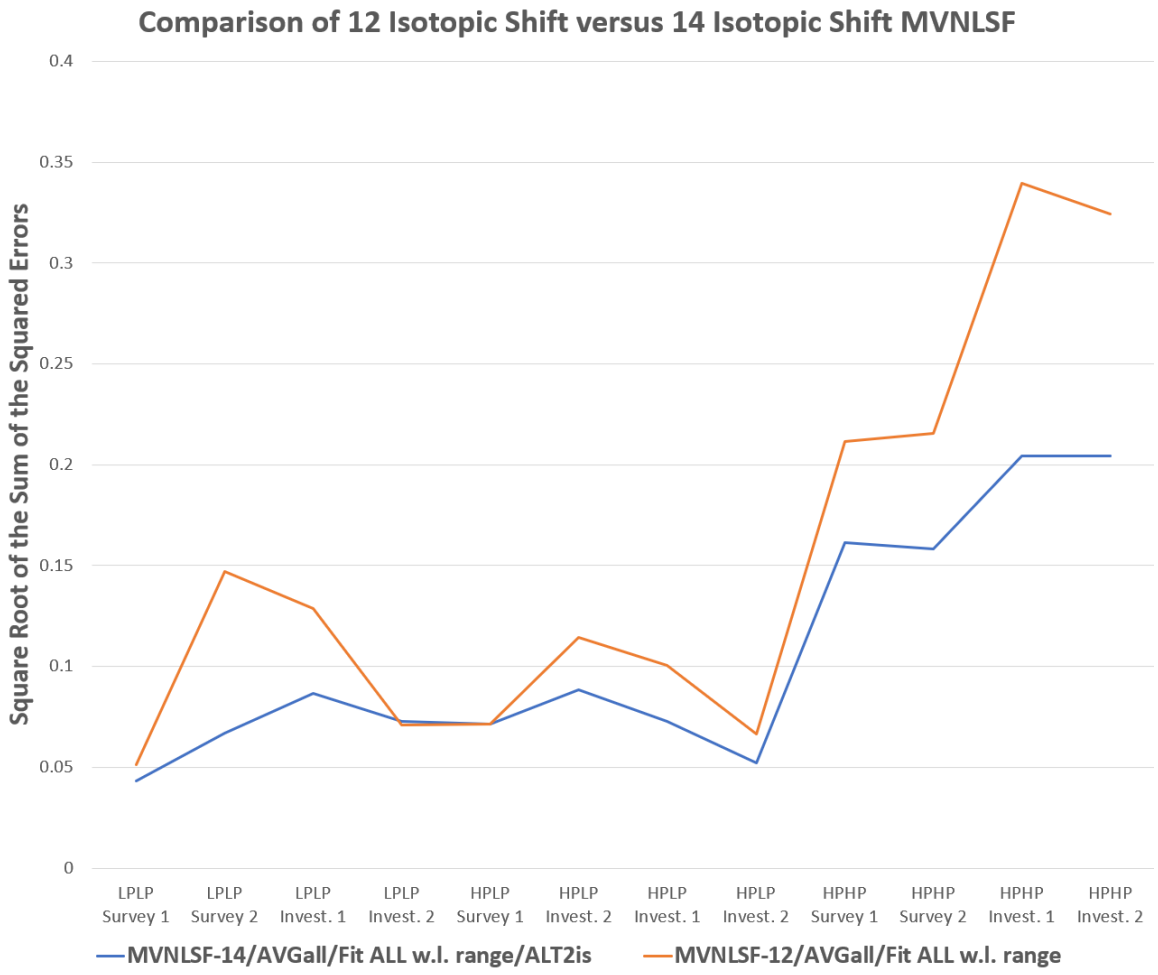


Figure 4.25. Graph comparing the error magnitude for assay measurement using the original 12-pair MVNLSF algorithm and the 14-pair MVNLSF (MVNLSF-14) measurement approach, which adds the 2 isotopic pairs identified as having benefit for fs-LIBS measurement in this research. The error magnitude data is charted as the square root of the sum of the squared errors for each sample assay measured in each testing configuration.

Reexamination of Spectra with Emphasis on SD

The focus of the fs-LIBS testing effort to this point has been targeted at the parameters that yield the closest average assay measurement from a five spectra group to the actual assay of the sample being tested. This begs the question of how much accuracy would be given up if the metric were to focus on the fs-LIBS parameters that yield the lowest standard deviation. The collected data and analysis results were reexamined for the HPHP Survey (lowest average error magnitude), the HPHP investigation (lowest average SD, RMSE, and MAE), and the Kinetic Series (greatest SNR). The tables and results that report the delay and gate width combinations which yielded the lowest SD will be noted with (SD). The reexamination also will identify the optimal delay and gate width settings if accuracy and precision were equally important. To accomplish this task, an additional factor was calculated for the results of each delay and gate width combination involved in the reexamination of the data. The factor is the obtained by multiplying the standard deviation of the assay predictions from each of the five spectra collected at every delay and gate width combination by the cumulative error for that delay and gate width at each *dr* between *dr*=0.030 and *dr*=0.1. The tables and results that report the delay and gate width combinations which yielded the lowest factors will be noted with (Combo).

The 0.287% sample was not included in this reexamination because the standard deviation is artificially high for all the delay and gate widths that yield estimated assay of 0% ^{235}U. Eliminating all the delay and gate widths reporting average assays of 0% ^{235}U left only delay and gate widths yielding significant over-estimation of assay. This fact would have skewed the results of the re-examination and made comparison back to the assay-focused test results uninformative. Therefore, this re-examination will substitute the 38.103% assay sample for the 0.287% sample. The 38.103% sample was tested an equal number of times as were each of the others in the data used for this reexamination.

The original HPHP Surveys yielded the most accurate average assay measurements of any of the test configurations. The delay and gate width span that produced these results tightened slightly and shifted slightly later in the plasma timeline, as shown in Table 4.16. Table 4.17 illustrates that shifting to a focus of lowest SD increases the average error by 1.1% but yields a 1.5% improvement in the SD. The results from the approach of optimizing the Combo factor are shown in Table 4.18. Table 4.18 reports further tightening of the span of best performing delay and gate width combination and continues the trend toward being slightly later in the plasma emission timeline. Refer to Table 4.17 to see that the combination approach increases the average error by only 0.45%, or less than half the jump seen when optimizing the SD, while still achieving a 1.31% reduction in the SD from the average assay-focused results.

Table 4.16. HPHP Survey data with delay and gate width based on (SD)

ORNL Report. Enrich.	**4.615%**		**18.525%**		**38.103%**		**61.740%**	
Delay and Gate Width (ns)	1208-333	1208-333	783-283	2033-408	1208-333	1208-333	1733-308	2358-433
MVNLSF Calc'd Enrich.	4.35%	3.93%	21.7%	19.6%	38.3%	38.7%	62.6%	65.2%
Error from ORNL Report. Enrich.	-0.27 %	-0.69 %	3.15 %	1.10 %	0.16 %	0.64 %	0.86 %	3.48 %
Increase in Error	0.08%	0.51%	2.82%	0.95%	0.00%	0.00%	0.85%	3.45%
Standard Dev.	0.35%	0.54%	0.93%	0.77%	0.81%	0.93%	1.06%	1.47%
Standard Dev. Reduct.	1.12%	1.09%	2.52%	1.47%	0.00%	0.00%	1.69%	4.48%
Relative Standard Dev.	8.1%	13.7%	4.3%	1.2%	2.1%	2.4%	1.7%	2.3%
RMSE	0.58%	0.87%	3.26%	3.55%	0.75%	1.06%	1.28%	2.34%
Mean Absolute Error	0.51%	0.76%	3.15%	3.48%	0.55%	0.93%	0.89%	1.93%

Table 4.17. HPHP Survey Summary Results for (SD), (Combo), and the original HPHP

Testing Configuration	**HPHP (SD)**	**HPHP (Combo)**	**HPHP**
Average Error from ORNL Reported Enrichment	1.29%	0.66%	0.15%
Average Increase in Error	1.1%	0.45%	
Average Standard Deviation	0.86%	1.10%	2.30%
Average Standard Deviation Reduction	1.5%	1.31%	
Average Relative Standard Deviation	4.5%	6.11%	67.8%
Average RMSE	1.71%	1.25%	2.12%
Average Mean Absolute Error	1.52%	1.01%	1.86%

Table 4.18. HPHP Survey data with delay and gate width based on (Combo) Factor

ORNL Report. Enrich.	**4.615%**		**18.525%**		**38.103%**		**61.740%**	
Delay and Gate Width (ns)	1208-333	1208-333	2358-433	2708-458	1208-333	1208-333	1733-308	1733-383
MVNLSF Calc'd Enrich.	4.35%	3.93%	17.3%	17.8%	38.3%	38.7%	62.6%	62.4%
Error from ORNL Report. Enrich.	-0.27 %	-0.69 %	-1.26 %	-0.76 %	0.16 %	0.64 %	0.86 %	0.65 %
Increase in Error	0.08%	0.51%	0.94%	0.60%	0.00%	0.00%	0.85%	0.62%
Standard Dev.	0.35%	0.54%	1.54%	1.56%	0.81%	0.93%	1.06%	1.98%
Standard Dev. Reduct.	1.12%	1.09%	1.91%	0.68%	0.00%	0.00%	1.69%	3.98%
Relative Standard Dev.	8.1%	13.7%	8.9%	8.8%	2.1%	2.4%	1.7%	3.2%
RMSE	0.58%	0.87%	1.91%	1.70%	0.75%	1.06%	1.28%	1.89%
Mean Absolute Error	0.51%	0.76%	1.57%	1.38%	0.55%	0.93%	0.89%	1.51%

The original HPHP Investigations produced the lowest average SD of any of the original test configurations. The optimal SD results produce a 0.6% improvement in the average SD, but there is also a 1.01% increase in the average error reflected in Table 4.19. As was the case in the HPHP Survey reexamination, there is a slight trend later in the plasma emission timeline associated with improved SD results shown in Table 4.20. The Combo factor optimal results, see Table 4.21, occur at delay and gate width combinations very similar to the original HPHP Investigation optimal average assay values. Referring to Table 4.19, the Combo factor results only increase the error by 0.03% over the original HPHP investigation, but are able to improve the SD by 0.23% on average.

The Kinetic Series collected in the HPHP laser power and sample chamber pressure configuration benefitted from several steps to improve the SNR. The reexamination focusing on optimization of SD produced a significant shift forward in the plasma emission timeline for the best performing delay and gate width combinations as shown in Table 4.22. This trend was contrary to that observed in the survey and investigation reexamination. In the original Kinetic Series findings focused on the most accurate average assay, the results for all samples except 0.287% had delays of 1445 ns and greater. The longest delay in the SD optimal results was 970 ns. The summary results shown in Table 4.23 report that the increase in the average error for measuring assay was 1.45%, but the reduction in the average SD was 2.09% better than the original Kinetic Series results. The Combo factor optimized results, shown in Table 4.24 are the same as the original ones for the 4.615% and 18.525% samples. The 61.740% sample produces the optimal results at a 445 ns delay and 150 ns gate width. This result is one frame earlier in the kinetic series than the optimal from the SD reexamination. However, both the SD and Combo factor reexamination produce delay and gate widths much earlier in the plasma life than the original 61.740% Kinetic Series result of a 2020 ns delay and a 325 ns gate width.

Potential Contributors to SD Results

There was a plasma emission variability that should be mentioned to provide a more complete picture of a phenomenon that occurred during the HPHP testing configuration. The plasma emission was observed to vary with a period of about 2 cycles per second. The average exposure during the HPHP data collection was 4 seconds. The peak and valley of the emission variation are shown in Fig. 4.26. The pictures on the left are zoomed-in screen captures from a video of the oscilloscope output. The oscilloscope was responding to the pulsations in the plasma intensity. The blue line decaying to the right is the output from the photodetector. Note that in the upper oscilloscope screen capture, the blue line terminates at essentially the same level as the constant green signal in the lower right of the screen capture.

Table 4.19. HPHP Investigation Summary Results for (SD), (Combo), and the original HPHP Investigation results

Testing Configuration	**HPHP (SD)**	**HPHP (Combo)**	**HPHP**
Average Error from ORNL Reported Enrichment	1.36%	0.38%	0.28%
Average Increase in Error	1.01%	0.03%	
Average Standard Deviation	0.85%	1.20%	0.90%
Average Standard Deviation Reduction	0.6%	0.23%	
Average Relative Standard Deviation	5.4%	6.71%	62.1%
Average RMSE	1.65%	1.21%	0.92%
Average Mean Absolute Error	1.51%	1.04%	0.78%

Table 4.20. HPHP Investigation data with delay and gate width based on (SD)

ORNL Report. Enrich.	**4.615%**		**18.525%**		**38.103%**		**61.740%**	
Delay and Gate Width (ns)	938-1033	938-1033	1238-1348	1033-1133	1583-1708	683-763	1583-1708	848-938
MVNLSF Calc'd Enrich.	5.05%	4.77%	20.0%	21.2%	39.0%	39.2%	62.3%	65.2%
Error from ORNL Report. Enrich.	0.43%	0.16%	1.51%	2.72%	0.93%	1.12%	0.60%	3.43%
Increase in Error	0.26%	0.00%	1.46%	2.41%	0.69%	0.56%	0.00%	2.73%
Standard Dev.	0.72%	0.61%	0.68%	1.04%	0.86%	0.91%	0.93%	1.07%
Standard Dev. Reduct.	0.35%	0.00%	0.08%	0.75%	1.50%	1.72%	0.00%	0.21%
Relative Standard Dev.	14.3%	12.7%	3.4%	4.9%	2.2%	2.3%	1.5%	1.6%
RMSE	0.81%	0.67%	1.63%	2.88%	1.21%	1.39%	1.03%	3.56%
Mean Absolute Error	0.70%	0.57%	1.51%	2.72%	1.15%	1.19%	0.81%	3.43%

Table 4.21. HPHP Investigation data with delay and gate width based on (Combo) Factor

ORNL Report. Enrich.	**4.615%**		**18.525%**		**38.103%**		**61.740%**	
Delay and Gate Width (ns)	938-1033	938-1033	1708-1838	1708-1838	1708-1838	1133-1238	1583-1708	1348-1463
MVNLSF Calc'd Enrich.	5.05%	4.77%	18.6%	18.2%	37.9%	37.5%	62.3%	62.4%
Error from ORNL Report. Enrich.	0.43 %	0.16 %	0.05 %	-0.31 %	-0.24 %	-0.58 %	0.60 %	0.70 %
Increase in Error	0.26%	0.00%	0.00%	0.00%	0.00%	0.01%	0.00%	0.00%
Standard Dev.	0.72%	0.61%	0.76%	1.79%	2.36%	1.16%	0.93%	1.28%
Standard Dev. Reduct.	0.35%	0.00%	0.00%	0.00%	0.00%	1.47%	0.00%	0.00%
Relative Standard Dev.	14.3%	12.7%	4.1%	9.8%	6.2%	3.1%	1.5%	2.1%
RMSE	0.81%	0.67%	0.82%	1.69%	2.13%	1.19%	1.03%	1.35%
Mean Absolute Error	0.70%	0.57%	0.70%	1.50%	1.80%	1.06%	0.81%	1.15%

Table 4.22. HPHP Kinetic Series Improved SNR data with delay and gate width based on (SD)

ORNL Reported Enrich.	**4.615%**	**18.525%**	**38.103%**	**61.740%**
Delay and Gate Width (ns)	445-150	970-225	770-200	595-175
MVNLSF Calc'd Enrich.	3.31%	21.3%	39.7%	63.7%
Error from ORNL Reported Enrich.	-1.31%	2.76%	1.62%	2.00%
Increase in Error	1.08%	2.66%	0.56%	1.52%
Standard Deviation	0.34%	0.94%	1.34%	1.70%
Standard Deviation Reduction	1.31%	1.18%	2.38%	3.47%
Relative Standard Deviation	10.27%	4.43%	3.37%	2.66%
RMSE	1.34%	2.91%	2.03%	2.53%
Mean Absolute Error	1.31%	2.76%	1.69%	2.08%

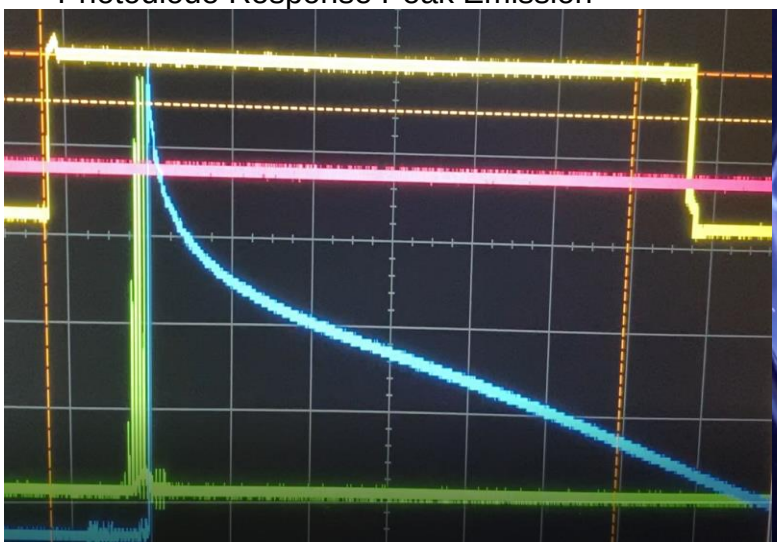
Table 4.23. HPHP Kinetic Series Improved SNR Summary Results for (SD), (Combo), and the original HPHP Kinetic Series Improved SNR results

Testing Configuration	**HPHP Kinetic Series (SD)**	**HPHP Kinetic Series (Combo)**	**HPHP Kinetic Series**
Average Error from ORNL Reported Enrichment	1.92%	0.80%	0.22%
Average Increase in Error	1.45%	0.33%	
Average Standard Deviation	1.08%	1.76%	2.40%
Average Standard Deviation Reduction	2.09%	1.41%	
Average Relative Standard Deviation	5.19%	12.98%	62.3%
Average RMSE	2.20%	1.89%	2.16%
Average Mean Absolute Error	1.96%	1.45%	1.72%

Table 4.24. HPHP Kinetic Series Improved SNR data with delay and gate width based on (Combo) factor

ORNL Reported Enrich.	**4.615%**	**18.525%**	**38.103%**	**61.740%**
Delay and Gate Width (ns)	1445-275	2020-325	770-200	445-150
MVNLSF Calc'd Enrich.	4.84%	18.6%	39.7%	63.0%
Error from ORNL Reported Enrich.	0.23%	0.10%	1.62%	1.24%
Increase in Error	0.00%	0.00%	0.56%	0.76%
Standard Deviation	1.65%	2.12%	1.34%	1.91%
Standard Deviation Reduction	0.00%	0.00%	2.38%	3.26%
Relative Standard Deviation	34.09%	11.41%	3.37%	3.03%
RMSE	1.50%	1.91%	2.03%	2.12%
Mean Absolute Error	1.15%	1.53%	1.69%	1.44%

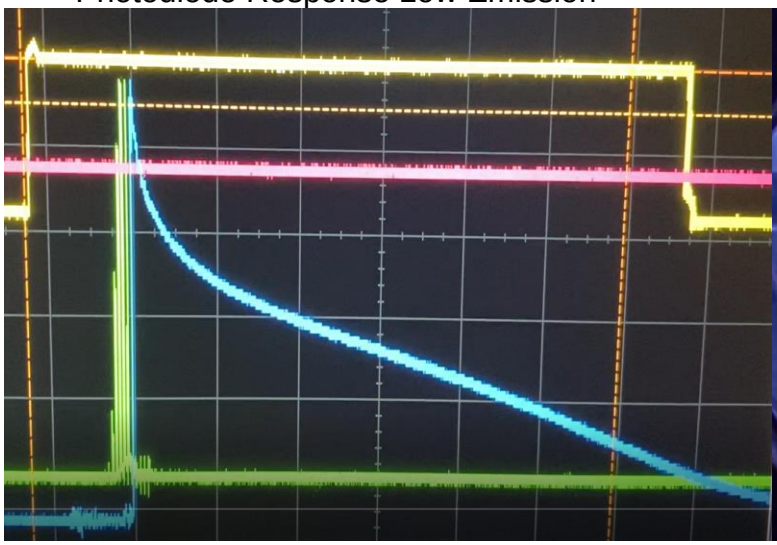
Photodiode Response Peak Emission



Peak Brightness



Photodiode Response Low Emission



Least Brightness



Figure 4.26. Sinusoidally Varying Plasma Emission Intensity at ~ 2 Hz

To the right of the oscilloscope screen capture is another screen capture of the plasma emission at its peak intensity. The lower oscilloscope screen capture now shows that the decaying blue line signal from the photodetector terminates below the constant green signal in the lower right-hand corner of the screen capture. The screen capture of the plasma in the lower right shows the emission corresponding to this reduced intensity.

The pressure within the sample chambers remained approximately constant during these periods of variable emission intensity. According to the laboratory's Ophir power meter the laser power output was not varying. A potential cause for this plasma emission variation was documented by Heins and Guo when they reported plasma instability when testing a similar Ti:sapphire laser, (68 fs pulse at 800 nm and up to 1kH repetition rate) to the one used in this research, at high repetition rates [82]. They attribute the instability to electrons that are able to persist for several milliseconds which can be pushed away from the location of their creation by plasma expansion and then introduce varying amount of plasma defocus [82]. These electrons are prone to interact with the emission "pedestal" that always precedes a femtosecond pulse [82, 131]. The details of the instability observed by Heins and Guo differs from this research, but the root cause that they propose highlights the impact that recombination rate of the interrogated material and the residual electron can have on subsequent pulses when they arrive every 1 µs as was the case in this research [82]. Heins and Guo reported stability beyond 30 µs between pulses which would indicate a repetition rate of about 30 Hz [82].

The collection of multiple spectra and exposure times which were on average eight times longer than the period of the plasma emission variations are expected to minimize the impact on the captured spectra and results. However, given the SDs were slightly higher than comparable nanosecond LIBS research, this phenomenon was important to mention as it may have had some effect that went undetected during this research. A possible example could have been an unpredictable interrelation between the self-absorption known to exist in the region of the 424.37 nm ^{235}U emission [27].

Self-absorption can occur when emitted photons travel through the portion of the plasma separating them from the surrounding environment [27]. The emitted photons could encounter a neutral atom or atomic ion of the same species but in an electronic state capable of absorbing the photon [27]. The extent of the self-absorption is driven, in part, by the absorption path length [27]. As can be seen in Fig. 4.26 the brighter plasma appears larger than the dim plasma, leading to the potential for varying absorption path length.

Chapter Five

Conclusions

This dissertation reports research that enhances the state-of-the-art in assay measurement using Laser-Induced Breakdown Spectroscopy. This work has been accomplished with the support of the Nuclear Science and Security Consortium's funding of the majority of the needed hardware and with the willingness of Oak Ridge National Laboratory to provide the needed UF_6 samples. The niche into which this research fits has similarly been targeted to coordinate with and support the research and development already taking place in national laboratories. The research is also deemed important and worthwhile by Centrus Energy which contributed facilities, personnel time, expert consultants, and other capabilities required to execute the research.

Application of fs-LIBS to UF_6 Assay Measurement

One of the contributions of this research is that to-date this appears to be the broadest range of UF_6 assays interrogated for research and publication purposes. Additionally, this research provides insight into the performance parameters needed to successfully complete fs-LIBS measurements, which are quite different from previously reported nanosecond LIBS parameters. Through the course of this research several additional findings and contributions were achieved dealing with the optimum delay and gate width for fs-LIBS assay measurement as well as additional isotopic shifts which contribute to fs-LIBS assay measurement accuracy. This research was conducted over a period in excess of six months, thereby demonstrating that the fs-LIBS system is capable of collecting spectra useful for assay measurement for an extended period of time. Since the results of the primary testing configurations were repeated an average seven days after the first test, there can be confidence that system repeatability has been initially demonstrated by this research.

Optimum Laser Power and UF_6 Sample Pressure

The LPLP testing configuration yielded worse assay determination performance when the captured spectra were evaluated with MVNLSF for both the survey and investigation delay and gate width testing campaigns. This knowledge is valuable because it highlights a challenge that future researchers will need to overcome in obtaining sufficient SNR from fs-LIBS plasmas. The poor LPLP results do not close the door on potential future benefits from conducting fs-LIBS at these reduced pressures and powers, but highlight the need for additional work toward obtaining enough signal at these reduced power and pressure conditions to fully

answer whether there is an observable reduction of spectral clutter similar to that reported during LISA-UE research and whether there is a benefit to fs-LIBS research [80]. The conclusion from the results obtained from this research is that LPLP fs-LIBS yields too poor an SNR to fully assess fs-LIBS capability in this region.

The HPHP laser power and sample chamber pressure yielded the most accurate average assay results during the HPHP Surveys and the lowest standard deviation during the HPHP Investigations. The average assay measurement error achieved during the HPHP survey and investigation, 0.15% and 0.28% respectively, compares favorably to the current nanosecond LIBS technology LISA-UE where the average error reported was 0.33% for samples of 0.72%, 4.675%, and 9.157% UF_6 [23]. The fs-LIBS assay measurement standard deviations are of larger magnitude than those reported by the LISA-UE researchers who reported an average standard deviation of 0.21% [23]. The average standard deviation of the HPHP investigation was 0.90%. It is important to remember that the results from fs-LIBS research were taken in the spectral region around the 424.437 and 424.412 nm isotopic pair. Thus self-absorption, known to exist in this spectral region, may have played an amplified role in widening the standard deviations of the fs-LIBS measurement due to the plasma instabilities reported in this research [23, 24, 27]. Although the goal of leveraging the femtosecond laser to improve the accuracy of LIBS-based assay measurements was not achieved, there is a potential benefit of the fs-LIBS system which should be considered for future research targeted at continuous online measurements at GCEP. The fs-LIBS measurements were taken at a pressure of ~60 Torr, as opposed to the 15 Torr pressure with which the LISA-UE research has been conducted [23]. A pressure of 60 Torr is closer to the pressures likely to be seen at a GCEP [119]. The results from the HPHP testing configuration provide clear indication of the benefit of ample laser power and increased sample chamber pressure when making fs-LIBS assay measurements. Given these results, future fs-LIBS research in a spectral region lacking self-absorption may surpass current LIBS-based assay measurement accuracy.

Impact of Precipitate Buildup

The precipitate buildup which befell the 38.103% sample provided the opportunity to investigate and report on the ability of the fs-LIBS system to deal with the types of buildup or holdup which might occur in an actual GCEP. The fs-LIBS system's less intense plasma did present challenges to obtaining sufficient SNR for a high confidence assay measurement, but in the HPHP testing configuration, successful measurements were, nevertheless, collected in spite of the precipitate formation on the sample chamber's collection window.

Additional Assay Measurement Contributions

The plasma emission valuation reported in this research is a first-of-a-kind attempt to understand the value of the temporal emissions which emanate from plasmas produced for the purpose of measuring UF_6 assay. This valuation was developed in an attempt to understand the differing optimal delay and gate width which were being reported for the various UF_6 samples interrogated in this research. Ultimately no clear driver for the differences in the optimal delay and gate width settings was verified, but the accuracy of the plasma temporal valuation approach itself was confirmed through the execution of a kinetic series experiment which resulted in optimum delay and gate widths that aligned closely with the plasma emission valuation reporting.

The *dr* fitting window approach to minimize the impact of spectral clutter during the application of fitting algorithms slightly outperformed the traditional approach of fitting the entire spectral window. However, the performance is similar enough to the traditional approach of fitting the entire spectral window of interest, that the *dr* fitting window approach should be considered a tool to employ when spectral clutter is suspected of impacting the measurements being attempted.

The identification and implementation of a MVNLSF algorithm which utilized two additional isotopic shifts and improved assay measurement accuracy provides additional information to the state of the art for assay measurement in two ways. First, one of the isotopic shifts fell within the range of the original 12 isotopic shifts proposed by Song et. al, so the usefulness of the 424.374 (^{235}U) – 424.392 (^{238}U) isotopic pair to fs-LIBS indicates that this is one of the subtle differences between nanosecond and femtosecond LIBS allowing for detection and beneficial utilization of this isotopic shift [67]. Second, the benefit of an isotopic shift, from the 424.262 (^{235}U) – 424.258 (^{238}U) isotopic pair, indicates that the precision calibration approach described in this research, when applied to each spectrum, is able to help researchers avoid areas of Stark shift and Stark broadening while providing calibration accuracies that allow utilization of isotopic shifts outside the 424.3 to 424.5 nm range.

Advanced Numerical Analysis Techniques Demonstrated

The identification of two additional isotopic shifts was accomplished through utilization of an advanced numerical technique applying HOGSVD. This technique appears to be a novel application allowing the researcher to assign an importance to each wavelength in terms of discriminating one spectrum from another. When applied to spectra of different assay UF_6 samples this is an efficient way to draw a researcher's attention to wavelengths which discriminate the two spectra from one another. These areas of discrimination focus a

researcher's search for additional isotopic shifts which could be valuable to MVNLSF-type assay measurement efforts. Additionally, this presentation of wavelength importance allows a researcher to quickly scan through many spectra to determine the prevalence of the potential isotopic shift across a large dataset.

Advanced numerical techniques were also tested in novel applications related to the classification of unknown assays being analyzed by models using only HOGSVD-DTW features to make assessment, through classification, of which assays from the training data the unknown most likely belonged with. The application of advanced numerical techniques was extended to include the estimation of assay with complete models including training data for each of the assays being measured. Finally, a proof-of-concept demonstrated distinct advantages to using HOGSVD-DTW features to make an assessment of the assay of an unknown sample based on training data that does not include the assay of the sample being measured. This proof-of-concept was executed alongside a competing model relying on the spectral data itself to underscore the utility of HOGSVD-DTW features for making assay assessments without any need for detailed isotopic shift information.

The advanced numerical techniques applied during this research are extremely encouraging when viewed from the perspective of the assay measurement accuracy that they provide in comparison to the relatively minimal knowledge a user needs of the specific isotopic shifts that differentiate the assays of UF_6 being measured. A user relying on HOGSVD-DTW to make an assessment of assay only needs to know the region of the spectrum where groups of isotopic shifts are clustered without the need for precise identification and fitting required by MVNLSF techniques. Additionally, the advanced numerical techniques demonstrated in this research can be applied to nanosecond laser-produced spectra.

Future Work

As discussed throughout this dissertation, this work has focused on the underlying methods and approaches that support eventual deployment of an online UF_6 measurement capability. Additional research is required specifically aimed at continuing the progression toward online measurements. Focus areas include the impact of contaminants frequently found in GCEPs. The apparent recombination of UF_6 that occurs in the sample chambers may be a result of the purity of the samples that have been investigated thus far. Contaminants in a GCEP may reduce the efficiency of the recombination to UF_6, resulting in formation of a contaminant that is detrimental to the enrichment process or to the product purity. The observed precipitate formation in the 38.103% sample used

in this research places emphasis on the need to understand these processes more fully through future work.

Future work is also needed to explore the effect of reduced repetition rate on fs-LIBS assay measurement precision and accuracy. Testing should be conducted to determine whether the plasma stability observed by Heins and Guo, who reported stability beyond 30 μs between pulses, also occurs when applied to UF_6 plasmas [82]. If the behavior observed by Heins and Guo does extend to UF_6 plasmas and the plasma stability has a positive effect on assay measurement, then additional testing is needed to determine the optimum tradeoff between exposure time and accuracy/precision [82].

Exploration of additional femtosecond laser pulses to re-excite femtosecond plasmas is an area worthy of additional investigative work. As discussed in Chapter 2, one of the potential benefits of femtosecond lasers is the ability to deliver a subsequent femtosecond pulse to an already formed plasma to explore the impacts on the plasma emission. In fact, additional research in this area could potentially overcome the challenges of the dimmer, less persistent femtosecond plasma.

The potential of the advanced numerical techniques in this research warrants future investigation into the numerical features that will continue to enhance the ability of these features both to assess incoming numerical information about spectra to assign a class of enrichment and to make an estimation of the exact enrichment of the unknown. Additional extension of advanced SVD approaches is warranted to enhance the ability to determine assay across wider ranges of laser power, sample pressure, plasma temporal emission, peak broadening, and sample contamination than were tested in this work.

It is important to increase the granularity of the testing to determine the optimum pressure for conducting fs-LIBS. This work essentially used two pressures. There is likely some pressure between the LPLP testing configuration and the HPHP testing configuration that yields an optimum balance of signal intensity and minimized spectral clutter.

Finally, although the fs-LIBS technique does appear less impacted by self-absorption bias than nanosecond LIBS, additional research is needed focusing fs-LBIS research on the 421.3 nm spectral region to avoid the resonance emissions and self-absorption as the LISA-UE researchers have done since this research effort began [23, 24, 27]. Given the results obtained through fs-LIBS at the 424.4 nm spectral region, there is a significant possibility that the fs-LIBS assay measurement capability has potential benefits in the 421.3 nm region as well as the potential for additional isotopic shifts that were not identifiable and usable with nanosecond induced LIBS processes.

fs-LIBS Conclusion

This research has presented a wide range of information which may be difficult to aggregate into a best-approach for conducting future assay measurements using fs-LIBS in the 424.4 nm spectral region. This was made even more difficult to parse based on the discovery of different optimum delay and gate width settings based on the sample assays. The best approach for a practitioner planning a measurement of an unknown assay using the processes demonstrated in this research for the greatest accuracy and precision is to do the following:

- The spectrometer should be centered on 424.4 nm and the ICCD settings should be those described for the improved SNR kinetic series testing employing a 2X gain setting and a reduced A/D conversion rate of 1 MHz.
- The HPHP testing configuration should be employed.
    - The samples should be maintained at approximately 60 Torr which corresponds to the thermoelectric cooler remaining off in this research's laboratory arrangement.
    - The laser power should be set to 100% with minimal redirection of the laser beam before the focusing lens.
- The exposure time should be determined based on achieving a peak single-pixel-emission intensity measurement of 30,000 counts in the 424.4 nm spectral region on an image representation of the ICCD output as described in the exposure section of Chapter 3.
- The delay and gate width should be in accordance with the HPHP investigation testing series because the lengthened gate-widths were determined to be the most probable reason that the HPHP investigation precision and accuracy results remained superior to the results from the improved SNR kinetic series testing.
- The specific delay and gate width most likely to produce a high-quality measurement of an unknown assay's spectrum is 848 ns and 938 ns respectively based on being the best balance between each of the best performing delay and gate width combinations and occurring late enough to avoid the greatest Stark width and Stark shift impacts.
- At least 5 spectra should be captured and they should be analyzed using the MVNLSF approach including the use of the two additional isotopic shifts as described in this research.

Employing the steps described above aggregates the findings in this research to produce the most accurate and precise assay measurement possible using fs-LIBS focused on the 424.4 nm spectral region.

List of References

[1] A. M. Shaw, R. N. Zare, C. V. Bennett, and B. H. Kolner, “Bounce-by-bounce cavity ring-down spectroscopy: Femtosecond temporal imaging,” *Chemphyschem,* vol. 2, no. 2, pp. 118-+, Feb, 2001.

[2] A. G. Berezin, S. L. Malyugin, A. I. Nadezhdinskii, D. Y. Namestnikov, Y. Y. Ponurovskii, D. B. Stavrovskii, Y. P. Shapovalov, I. E. Vyazov, V. Y. Zaslavskii, Y. G. Selivanov, N. M. Gorshunov, G. Y. Grigoriev, and S. S. Nabiev, “UF6 enrichment measurements using TDLS techniques,” *Spectrochimica Acta Part a-Molecular and Biomolecular Spectroscopy,* vol. 66, no. 4-5, pp. 796-802, Apr, 2007.

[3] G. Chan, J. Valentine, and R. Russo, "Scoping study to expedite development of a field deployable and portable instrument for UF6 enrichment assay " U. S. D. o. Energy, ed., Lawrence Berkeley National Laboratory 2017.

[4] A. S. f. T. a. M. A. International, "Standard Test Method for Isotopic Analysis of Uranium Hexafluoride by Double Standard Single-Collector Gas Mass Spectrometer Method," *C1742-17*, ASTM - International, 2017.

[5] A. S. f. T. a. M. A. International, "Standard Specification for Uranium Hexafluoride Enriched to Less Than 5 % ^{235}U," *C996-15*, ASTM - International, 2015.

[6] A. S. f. T. a. M. A. International, "Standard Test Method for Isotopic Analysis of Uranium Hexafluoride by Double-Standard Multi-Collector Gas Mass Spectrometer," *C4129-99*, ASTM - International, 2014.

[7] A. M. Shephard, “Process Attribute Monitoring Approach to Gaseous Centrifuge Enrichment Plant Safeguards,” Nuclear Engineering, University of Tennessee, University of Tennessee, 2016.

[8] D. A. Vermillion, “Improving Predictive Capabilities of Classical Cascade Theory for Nonproliferation Analysis ”, Nuclear Engineering, University of Tennessee, Knoxville, University of Tennessee, Knoxville, 2017.

[9] I. A. E. AGENCY, *IAEA Safeguards Glossary*, Vienna: INTERNATIONAL ATOMIC ENERGY AGENCY, 2003.

[10] G. C.-Y. Chan, J. D. Valentine, and R. E. Russo, “Towards novel field-deployable instrumentation for UF6 enrichment assay – an overview of existing and emerging technologies,” *ESARDA BULLETIN*, no. 54, pp. 31 - 43, June 2017, 2017.

[11] S. Richter, H. Kuhn, J. Truyens, M. Kraiem, and Y. Aregbe, “Uranium hexafluoride (UF6) gas source mass spectrometry for certification of reference materials and nuclear safeguard measurements at IRMM,” *Journal of Analytical Atomic Spectrometry,* vol. 28, no. 4, pp. 536-548, 2013.

[12] K. J. Mathew, and A. Haoszbek, “Comparison of mass spectrometric methods (TE, MTE and conventional) for uranium isotope ratio measurements,” *Journal of Radioanalytical and Nuclear Chemistry,* vol. 307, no. 3, pp. 1681-1687, Mar, 2016.

[13] M. Krachler, R. Alvarez-Sarandes, and S. Van Winckel, “Challenges in the quality assurance of elemental and isotopic analyses in the nuclear domain benefitting from high resolution ICP-OES and sector field ICP-MS,” *Journal of Radioanalytical and Nuclear Chemistry,* vol. 304, no. 3, pp. 1201-1209, Jun, 2015.
[14] M. Krachler, and P. Carbol, “Validation of isotopic analysis of depleted, natural and enriched uranium using high resolution ICP-OES,” *Journal of Analytical Atomic Spectrometry,* vol. 26, no. 2, pp. 293-299, 2011.
[15] M. Krachler, Z. Varga, A. Nicholl, M. Wallenius, and K. Mayer, “Spatial distribution of uranium isotopes in solid nuclear materials using laser ablation multi-collector ICP-MS,” *Microchemical Journal,* vol. 140, pp. 24-30, Jul, 2018.
[16] M. Krachler, and D. H. Wegen, “Promises and pitfalls in the reliable determination of U-233 using high resolution ICP-OES,” *Journal of Analytical Atomic Spectrometry,* vol. 27, no. 2, pp. 335-339, 2012.
[17] K. Zhao, M. Peńkin, C. Norman, S. D. Balsley, K. Mayer, P. Peerani, C. Pietri, S. Tapodi, Y. Tsutaki, M. Boella, G. Renha, and E. Kuhn, *International Target Values 2010 for measurement uncertainties in safeguarding nuclear materials*, 2010.
[18] A. Berlizov, A. Schachinger, K. Roetsch, N. Erdmann, H. Schorle, M. Vargas, J. Zsigrai, A. Kulko, M. Keselica, F. Caillou, V. Unsal, and A. Walczak-Typke, “Feedback from operational experience of on-site deployment of bias defect analysis with COMPUCEA,” *Journal of Radioanalytical and Nuclear Chemistry,* vol. 307, no. 3, pp. 1901-1909, Mar, 2016.
[19] F. R. Doucet, G. Lithgow, R. Kosierb, P. Bouchard, and M. Sabsabi, “Determination of isotope ratios using Laser-Induced Breakdown Spectroscopy in ambient air at atmospheric pressure for nuclear forensics,” *Journal of Analytical Atomic Spectrometry,* vol. 26, no. 3, pp. 536-541, 2011.
[20] L. E. Smith, A. R. Lebrun, and Ieee, "Design, Modeling and Viability Analysis of an Online Uranium Enrichment Monitor," *2011 Ieee Nuclear Science Symposium and Medical Imaging Conference*, IEEE Nuclear Science Symposium Conference Record, pp. 1030-1037, New York: Ieee, 2011.
[21] J. March-Leuba, J. Garner, J. Younkin, and D. W. Simmons, "On Line Enrichment Monitor (OLEM) UF6 Tests for 1.5” Sch40 SS Pipe Revision 1 " D. o. E. (DOE), ed., Oak Ridge National Laboratory 2016.
[22] P. L. Kerr, D. A. Close, W. S. Johnson, R. M. Kandarian, C. E. Moss, and C. D. Romero, "IAEA Verification Experiment at the Portsmouth Gaseous Diffusion Plant: Report on the Cascade Header Enrichment Monitor," 1999.
[23] G. C. Y. Chan, X. L. Mao, L. R. Martin, L. D. Trowbridge, and R. E. Russo, “Direct uranium enrichment assay in gaseous uranium hexafluoride with

laser induced breakdown spectroscopy," *Journal of Radioanalytical and Nuclear Chemistry*, pp. 13, 2022.
[24] G. Chan, K. Peruski, and L. Martin, "LASER-INDUCED SPECTROCHEMICAL ASSAY FOR URANIUM ENRICHMENT (LISA-UE)."
[25] M. B. Shattan, "Portable Laser-Induced Breakdown Spectroscopy for Nuclear Forensics Applications ", Nuclear Engineering, University of Tennessee, Knoxville University of Tennessee, Knoxville 2018.
[26] K. M. Peruski, T. A. Davis, G. C. Y. Chan, X. Mao, L. Trowbridge, and L. R. Martin, "Cell design for laser-induced breakdown spectroscopy measurements on reactive gas samples," *Journal of Fluorine Chemistry,* vol. 255-256, pp. 109951, 2022/03/01/, 2022.
[27] G. C. Y. Chan, L. R. Martin, L. D. Trowbridge, Z. Zhu, X. Mao, and R. E. Russo, "Analytical characterization of laser induced plasmas towards uranium isotopic analysis in gaseous uranium hexafluoride," *Spectrochimica acta. Part B: Atomic spectroscopy,* vol. 176, pp. 106036, 2021.
[28] I. A. E. AGENCY, "International Target Values 2010 for Measurement Uncertainties in Safeguarding Nuclear Materials," INTERNATIONAL ATOMIC ENERGY AGENCY (IAEA), 2010.
[29] N. Bohr, "The Spectra of Helium and Hydrogen," *Nature,* vol. 92, no. 2295, pp. 231-232, 1913/10/01, 1913.
[30] C. C. Kiess, C. J. Humphreys, and D. D. Laun, "PRELIMINARY DESCRIPTION AND ANALYSIS OF THE 1ST SPECTRUM OF URANIUM," *Journal of Research of the National Bureau of Standards,* vol. 37, no. 1, pp. 57-+, 1946, 1946.
[31] D. D. Smith, and L. E. Burkhart, *MASS ANALYSIS OF URANIUM ISOTOPES BY EMISSION SPECTROSCOPY,* Y-226 United States NTIS Y-12 English, ; Carbide and Carbon Chemicals Corp. Y-12 Plant, Oak Ridge, Tenn., 1948.
[32] L. E. Burkhart, G. Stukenbroeker, and S. Adams, "ISOTOPE SHIFTS IN URANIUM SPECTRA," *Physical Review,* vol. 75, no. 1, pp. 83-85, 1949.
[33] D. A. Cremers, and L. J. Radziemski, *Handbook of Laser-Induced Breakdown Spectroscopy*, Second ed.: John Wiley & Sons, Ltd, 2013.
[34] Y. Kamali, J. F. Daigle, F. Theberge, M. Chateauneuf, A. Azarm, Y. Chen, C. Marceau, S. C. Lessard, F. Lessard, G. Roy, J. Dubois, and S. L. Chin, "Remote sensing of trace methane using mobile ferntosecond laser system of T&T Lab," *Optics Communications,* vol. 282, no. 10, pp. 2062-2065, May 15, 2009.
[35] H. L. Xu, Y. Kamali, C. Marceau, P. T. Simard, W. Liu, J. Bernhardt, G. Mejean, P. Mathieu, G. Roy, J. R. Simard, and S. L. Chin, "Simultaneous detection and identification of multigas pollutants using filament-induced nonlinear spectroscopy," *Applied Physics Letters,* vol. 90, no. 10, Mar 5, 2007.

[36] D. D. Smith, J. R. McNally, G. L. Stukenbroeker, U. S. A. E. Commission, Carbide, and C. Carbon Chemicals, *New data on isotope shifts in uranium spectra U^{236} and U*, Oak Ridge, Tennessee: U.S. Atomic Energy Commission, Technical Information Service, 1951.
[37] D. D. Smith, *ISOTOPE SPECTRUM SHIFT DATA ON URANIUM SPECTRUM LINES,* AECD-3481; ORNL-1412 Country unknown/Code not available ORNL English, ; Oak Ridge National Lab., 1952.
[38] A. R. Striganov, and L. A. Korostyleva, "INVESTIGATION OF THE ISOTOPE EFFECT IN THE URANIUM SPECTRUM," *Soviet Physics Jetp-Ussr,* vol. 2, no. 2, pp. 277-289, 1956, 1956.
[39] E. W. T. Richards, and M. D. Crew, *THE URANIUM SPECTRUM BETWEEN 3500 A AND 5500 A WITH ASSOCIATED ISOTOPIC SHIFTS,* AERE-R-2941 United Kingdom BIS DTIE English, ; United Kingdom Atomic Energy Authority. Research Group. Atomic Energy Research Establishment, Harwell, Berks, England, 1959.
[40] Z. Hainski, and G. Rossi, "ISOTOPIC ANALYSIS OF URANIUM BY AN OPTICAL SPECTRAL METHOD .I. DETERMINATION OF U235 IN NATURAL AND DEPLETED URANIUM WITH DC ARC EXCITATION AND PHOTOGRAPHIC RECORDING," *Energia Nucleare,* vol. 12, no. 6, pp. 306-&, 1965, 1965.
[41] G. Rossi, and M. Mol, "Isotopic analysis of uranium by an optical spectral method-III. Determination of U235/U238 ratios with a hollow-cathode source and a direct-reading attachment," *Spectrochimica Acta Part B: Atomic Spectroscopy,* vol. 24, no. 7, pp. 389-390,E1-E2,391-398, 1969.
[42] G. Rossi, "Isotopic analysis of uranium by an optical spectral method-IV. Study of the suitability of some uranium lines for the absolute determination of isotopic ratios," *Spectrochimica Acta Part B: Atomic Spectroscopy,* vol. 26, no. 5, pp. 271-278, 1971.
[43] S. Gerstenkorn, P. Luc, and F. Tomkins, "RELATIVE ISOTOPIC SHIFTS AND QUADRUPOLAR INTRINSIC MOMENTS OF PLUTONIUM ISOTOPES," *Physica Scripta,* vol. 32, no. 3, pp. 195-200, 1985, 1985.
[44] W. H. King, "Isotope shifts in atomic spectra," New York : Plenum Press, 1984.
[45] P. Fichet, P. Mauchien, and C. Moulin, "Determination of impurities in uranium and plutonium dioxides by laser-induced breakdown spectroscopy," *Applied Spectroscopy,* vol. 53, no. 9, pp. 1111-1117, Sep, 1999.
[46] B. T. Fisher, H. A. Johnsen, S. G. Buckley, and D. W. Hahn, "Temporal gating for the optimization of laser-induced breakdown spectroscopy detection and analysis of toxic metals," *Applied Spectroscopy,* vol. 55, no. 10, pp. 1312-1319, Oct, 2001.
[47] F. Ferioli, P. V. Puzinauskas, and S. G. Buckley, "Laser-induced breakdown spectroscopy for on-line engine equivalence ratio

measurements," *Applied Spectroscopy,* vol. 57, no. 9, pp. 1183-1189, Sep, 2003.
[48] J. E. Carranza, E. Gibb, B. W. Smith, D. W. Hahn, and J. D. Winefordner, "Comparison of nonintensified and intensified CCD detectors for laser-induced breakdown spectroscopy," *Applied Optics,* vol. 42, no. 30, pp. 6016-6021, Oct, 2003.
[49] S. Yalcin, Y. Y. Tsui, and R. Fedosejevs, "Pressure dependence of emission intensity in femtosecond laser-induced breakdown spectroscopy," *Journal of Analytical Atomic Spectrometry,* vol. 19, no. 10, pp. 1295-1301, 2004, 2004.
[50] A. A. Ghazi, S. Qamar, and M. A. Atta, "URANIUM SPECTRA IN THE ICP," *Spectrochimica Acta Part B-Atomic Spectroscopy,* vol. 49, no. 5, pp. 527-531, May, 1994.
[51] D. P. Baldwin, D. S. Zamzow, and A. P. D'Silva, "High-Resolution Spectroscopy Using an Acousto-Optic Tunable Filter and a Fiber-Optic Fabry-Perot Interferometer," *Applied Spectroscopy,* vol. 50, no. 4, pp. 498-503, 1996.
[52] L. St-Onge, M. Sabsabi, and P. Cielo, "Analysis of solids using laser-induced plasma spectroscopy in double-pulse mode," *Spectrochimica Acta Part B-Atomic Spectroscopy,* vol. 53, no. 3, pp. 407-415, Mar 30, 1998.
[53] R. E. Neuhauser, B. Ferstl, C. Haisch, U. Panne, and R. Niessner, "Design of a low-cost detection system for laser-induced plasma spectroscopy," *Review of Scientific Instruments,* vol. 70, no. 9, pp. 3519-3522, Sep, 1999.
[54] V. Margetic, A. Pakulev, A. Stockhaus, M. Bolshov, K. Niemax, and R. Hergenroder, "A comparison of nanosecond and femtosecond laser-induced plasma spectroscopy of brass samples," *Spectrochimica Acta Part B-Atomic Spectroscopy,* vol. 55, no. 11, pp. 1771-1785, Nov 1, 2000.
[55] R. E. Russo, A. A. Bol'Shakov, X. Mao, C. P. McKay, D. L. Perry, and O. Sorkhabi, "Laser ablation molecular isotopic spectrometry," *Spectrochimica Acta - Part B Atomic Spectroscopy,* vol. 66, no. 2, pp. 99-104, 2011.
[56] X. L. Mao, A. A. Bol'shakov, D. L. Perry, O. Sorkhabi, and R. E. Russo, "Laser Ablation Molecular Isotopic Spectrometry: Parameter influence on boron isotope measurements," *Spectrochimica Acta Part B-Atomic Spectroscopy,* vol. 66, no. 8, pp. 604-609, Aug, 2011.
[57] X. L. Mao, A. A. Bol'shakov, I. Choi, C. P. McKay, D. L. Perry, O. Sorkhabi, and R. E. Russo, "Laser Ablation Molecular Isotopic Spectrometry: Strontium and its isotopes," *Spectrochimica Acta Part B-Atomic Spectroscopy,* vol. 66, no. 11-12, pp. 767-775, Nov-Dec, 2011.
[58] A. Sarkar, X. Mao, G. C. Y. Chan, and R. E. Russo, "Laser ablation molecular isotopic spectrometry of water for1D2/1H1ratio analysis,"

Spectrochimica Acta - Part B Atomic Spectroscopy, vol. 88, pp. 46-53, 2013.

[59] A. A. Bol'shakov, X. Mao, D. L. Perry, and R. E. Russo, “Laser Ablation Molecular Isotopic Spectrometry for Rare Isotopes of the Light Elements,” *Spectroscopy,* vol. 29, no. 6, pp. 30-+, Jun, 2014.

[60] X. L. Mao, G. C. Y. Chan, V. Zorba, and R. E. Russo, “Reduction of spectral interferences and noise effects in laser ablation molecular isotopic spectrometry with partial least square regression - a computer simulation study,” *Spectrochimica Acta Part B-Atomic Spectroscopy,* vol. 122, pp. 75-84, Aug, 2016.

[61] K. C. Hartig, I. Ghebregziabher, and I. Jovanovic, “Standoff Detection of Uranium and its Isotopes by Femtosecond Filament Laser Ablation Molecular Isotopic Spectrometry,” *Scientific Reports,* vol. 7, pp. 9, Mar, 2017.

[62] J. B. Sirven, B. Bousquet, L. Canioni, and L. Sarger, “Time-resolved and time-integrated single-shot laser-induced plasma experiments using nanosecond and femtosecond laser pulses,” *Spectrochimica Acta Part B-Atomic Spectroscopy,* vol. 59, no. 7, pp. 1033-1039, Jul 30, 2004.

[63] S. S. Harilal, J. R. Freeman, P. Diwakar, and A. Hassanein, "Comparison of nanosecond and femtosecond LIBS."

[64] J. Scaffidi, W. Pearman, J. C. Carter, and S. M. Angel, “Observations in collinear femtosecond-nanosecond dual-pulse laser-induced breakdown spectroscopy,” *Applied Spectroscopy,* vol. 60, no. 1, pp. 65-71, Jan, 2006.

[65] V. N. Lednev, M. Y. Grishin, P. A. Sdvizhenskii, R. D. Asyutin, R. S. Tretyakov, A. Y. Stavertiy, and S. M. Pershin, “Sample temperature effect on laser ablation and analytical capabilities of laser induced breakdown spectroscopy,” *Journal of Analytical Atomic Spectrometry,* vol. 34, no. 3, pp. 607-615, 2019.

[66] W. Pietsch, A. Petit, and A. Briand, “Isotope ratio determination of uranium by optical emission spectroscopy on a laser-produced plasma - basic investigations and analytical results,” *Spectrochimica Acta Part B-Atomic Spectroscopy,* vol. 53, no. 5, pp. 751-761, May, 1998.

[67] J. J. Song, G. C. Y. Chan, X. L. Mao, J. D. Woodward, R. W. Smithwick, T. G. Schaaff, A. C. Stowe, C. D. Harris, R. E. Zheng, V. Zorba, and R. E. Russo, “Multivariate nonlinear spectral fitting for uranium isotopic analysis with laser-induced breakdown spectroscopy,” *Spectrochimica Acta Part B-Atomic Spectroscopy,* vol. 150, pp. 67-76, Dec, 2018.

[68] N. A. Zubova, I. S. Anisimova, M. Y. Kaygorodov, Y. S. Kozhedub, A. V. Malyshev, V. M. Shabaev, Tupitsyn, II, G. Plunien, C. Brandau, and T. Stohlker, “Isotope shifts of the 1s(2)2s2p(J)-1s(2)2s(2) transition energies in Be-like thorium and uranium,” *Journal of Physics B-Atomic Molecular and Optical Physics,* vol. 52, no. 18, pp. 5, Sep, 2019.

[69] G. C. Y. Chan, I. Choi, X. L. Mao, V. Zorba, O. P. Lam, D. K. Shuh, and R. E. Russo, “Isotopic determination of uranium in soil by laser induced

breakdown spectroscopy," *Spectrochimica Acta Part B-Atomic Spectroscopy,* vol. 122, pp. 31-39, Aug, 2016.
[70] X. L. Mao, G. C. Y. Chan, I. Choi, V. Zorba, and R. E. Russo, "Combination of atomic lines and molecular bands for uranium optical isotopic analysis in laser induced plasma spectrometry," *Journal of Radioanalytical and Nuclear Chemistry,* vol. 312, no. 1, pp. 121-131, Apr, 2017.
[71] C. M. Davies, H. H. Telle, and A. W. Williams, "Remote in situ analytical spectroscopy and its applications in the nuclear industry," *Fresenius Journal of Analytical Chemistry,* vol. 355, no. 7-8, pp. 895-899, Aug, 1996.
[72] R. E. Russo, X. Mao, J. J. Gonzalez, and J. Yoo, "Femtosecond vs. Nanosecond laser pulse duration for laser ablation chemical analysis," *Spectroscopy (Santa Monica),* vol. 28, no. 1, 2013.
[73] J. Koch, S. Schlamp, T. Rosgen, D. Fliegel, and D. Gunther, "Visualization of aerosol particles generated by near infrared nano- and femtosecond laser ablation," *Spectrochimica Acta Part B-Atomic Spectroscopy,* vol. 62, no. 1, pp. 20-29, Jan, 2007.
[74] L. A. Emmert, R. C. Chinni, D. A. Cremers, C. R. Jones, and W. Rudolph, "Comparative study of femtosecond and nanosecond laser-induced breakdown spectroscopy of depleted uranium," *Applied Optics,* vol. 50, no. 3, pp. 313-317, Jan 20, 2011.
[75] B. W. Smith, A. Quentmeier, M. Bolshov, and K. Niemax, "Measurement of uranium isotope ratios in solid samples using laser ablation and diode laser-excited atomic fluorescence spectrometry," *Spectrochimica Acta Part B-Atomic Spectroscopy,* vol. 54, no. 6, pp. 943-958, Jun 14, 1999.
[76] T. A. Labutin, V. N. Lednev, A. A. Ilyin, and A. M. Popov, "Femtosecond laser-induced breakdown spectroscopy," *Journal of Analytical Atomic Spectrometry,* vol. 31, no. 1, pp. 90-118, 2016.
[77] V. I. Babushok, F. C. DeLucia, Jr., J. L. Gottfried, C. A. Munson, and A. W. Miziolek, "Double pulse laser ablation and plasma: Laser induced breakdown spectroscopy signal enhancement," *Spectrochimica Acta Part B-Atomic Spectroscopy,* vol. 61, no. 9, pp. 999-1014, Sep, 2006.
[78] S. S. Mao, F. Quere, S. Guizard, X. Mao, R. E. Russo, G. Petite, and P. Martin, "Dynamics of femtosecond laser interactions with dielectrics," *Applied Physics a-Materials Science & Processing,* vol. 79, no. 7, pp. 1695-1709, Nov, 2004.
[79] P. S. Hsu, A. K. Patnaik, A. J. Stolt, J. Estevadeordal, S. Roy, and J. R. Gord, "Femtosecond-laser-induced plasma spectroscopy for high-pressure gas sensing: Enhanced stability of spectroscopic signal," *Applied Physics Letters,* vol. 113, no. 21, pp. 4, Nov, 2018.
[80] G. C. Y. Chan, "Technical Training at Lawrence Berkeley National Laboratory," B. Jordan, ed., 2019.
[81] Y. Cao, X. L. Liu, W. D. Xian, S. H. Sun, M. Z. Sun, P. J. Ding, Y. C. Shi, Z. Y. Liu, and B. T. Hu, "Characterization of Femtosecond Laser-Induced

Plasma under Low Pressure in Argon," *Chinese Physics Letters,* vol. 32, no. 3, Mar, 2015.
[82] A. M. Heins, and C. L. Guo, "High stability breakdown of noble gases with femtosecond laser pulses," *Optics Letters,* vol. 37, no. 4, pp. 599-601, Feb, 2012.
[83] I. Choi, G. C. Y. Chan, X. L. Mao, D. L. Perry, and R. E. Russo, "Line Selection and Parameter Optimization for Trace Analysis of Uranium in Glass Matrices by Laser-Induced Breakdown Spectroscopy (LIBS)," *Applied Spectroscopy,* vol. 67, no. 11, pp. 1275-1284, Nov, 2013.
[84] R. C. Chinni, D. A. Cremers, L. J. Radziemski, M. Bostian, and C. Navarro-Northrup, "Detection of Uranium Using Laser-Induced Breakdown Spectroscopy," *Applied Spectroscopy,* vol. 63, no. 11, pp. 1238-1250, Nov, 2009.
[85] G. C. Y. Chan, X. L. Mao, I. Choi, A. Sarkar, O. P. Lam, D. K. Shuh, and R. E. Russo, "Multiple emission line analysis for improved isotopic determination of uranium - a computer simulation study," *Spectrochimica Acta Part B-Atomic Spectroscopy,* vol. 89, pp. 40-49, Nov, 2013.
[86] A. Safi, B. Campanella, E. Grifoni, S. Legnaioli, G. Lorenzetti, S. Pagnotta, F. Poggialini, L. Ripoll-Seguer, M. Hidalgo, and V. Palleschi, "Multivariate calibration in Laser-Induced Breakdown Spectroscopy quantitative analysis: The dangers of a 'black box' approach and how to avoid them," *Spectrochimica Acta Part B-Atomic Spectroscopy,* vol. 144, pp. 46-54, Jun, 2018.
[87] J. Blaise, and L. J. Radziemski, "ENERGY-LEVELS OF NEUTRAL ATOMIC URANIUM (UI)," *Journal of the Optical Society of America,* vol. 66, no. 7, pp. 644-659, 1976.
[88] J. Blaise, J. F. Wyart, J. Verges, R. Engleman, B. A. Palmer, and L. J. Radziemski, "ENERGY-LEVELS AND ISOTOPE SHIFTS FOR SINGLY IONIZED URANIUM (U-II)," *Journal of the Optical Society of America B-Optical Physics,* vol. 11, no. 10, pp. 1897-1929, Oct, 1994.
[89] A. J. Effenberger, Jr., and J. R. Scott, "Effect of Atmospheric Conditions on LIBS Spectra," *Sensors,* vol. 10, no. 5, pp. 4907-4925, May, 2010.
[90] A. S. Mangsor, Z. H. Rizvi, K. Chaudhary, M. S. Aziz, and Iop, "Classification of alloys using laser induced breakdown spectroscopy with principle component analysis," *International Laser Technology and Optics Symposium*, Journal of Physics Conference Series, Bristol: Iop Publishing Ltd, 2018.
[91] H. Y. Kong, L. X. Sun, J. T. Hu, Y. Xin, and Z. B. Cong, "Selection of Spectral Data for Classification of Steels Using Laser-Induced Breakdown Spectroscopy," *Plasma Science & Technology,* vol. 17, no. 11, pp. 964-970, Nov, 2015.
[92] M. Thomason, "Finding Geometric Structure in Multiple Matrices Simultaneously: From SVD to GSVD to HOGSVD," EECS, University of Tennessee, 2018.

[93] J. Vandewalle, L. De Lathauwer, and P. Comon, "The generalized higher order singular value decomposition and the oriented signal-to-signal ratios of pairs of signal tensors and their use in signal processing."
[94] S. Romppanen, H. Hakkanen, and S. Kaski, “Singular value decomposition approach to the yttrium occurrence in mineral maps of rare earth element ores using laser-induced breakdown spectroscopy,” *Spectrochimica Acta Part B-Atomic Spectroscopy,* vol. 134, pp. 69-74, Aug, 2017.
[95] C. F. Vanloan, “GENERALIZING SINGULAR VALUE DECOMPOSITION,” *Siam Journal on Numerical Analysis,* vol. 13, no. 1, pp. 76-83, 1976.
[96] L. De Lathauwer, B. De Moor, and J. Vandewalle, “A multilinear singular value decomposition,” *Siam Journal on Matrix Analysis and Applications,* vol. 21, no. 4, pp. 1253-1278, May, 2000.
[97] S. P. Ponnapalli, M. A. Saunders, C. F. Van Loan, and O. Alter, “A Higher-Order Generalized Singular Value Decomposition for Comparison of Global mRNA Expression from Multiple Organisms,” *Plos One,* vol. 6, no. 12, pp. 11, Dec, 2011.
[98] G. H. Golub, and C. F. Van Loan, *Matrix computations*: JHU press, 2013.
[99] I. Kempf, P. J. Goulart, and S. R. Duncan, "A Higher-Order Generalized Singular Value Decomposition for Rank Deficient Matrices," *arXiv*, 2021].
[100] F. Petitjean, A. Ketterlin, and P. Gancarski, “A global averaging method for dynamic time warping, with applications to clustering,” *Pattern Recognition,* vol. 44, no. 3, pp. 678-693, Mar, 2011.
[101] L. R. Martin, L. D. Trowbridge, J. M. Richards, and G. A. Fugate, "Design and Application of an Online Reactive Gas Cell for Safeguards Measurements of UF6."
[102] P. K. Morgan, J. R. Scott, and I. Jovanovic, “Hybrid interferometric/dispersive atomic spectroscopy of laser-induced uranium plasma,” *Spectrochimica Acta Part B-Atomic Spectroscopy,* vol. 116, pp. 58-62, Feb, 2016.
[103] P. Ko, K. C. Hartig, J. P. McNutt, R. B. D. Schur, T. W. Jacomb-Hood, and I. Jovanovic, “Adaptive femtosecond laser-induced breakdown spectroscopy of uranium,” *Review of Scientific Instruments,* vol. 84, no. 1, pp. 6, Jan, 2013.
[104] M. B. Shattan, D. J. Miller, M. T. Cook, A. C. Stowe, J. D. Auxier, C. Parigger, and H. L. Hall, “Detection of uranyl fluoride and sand surface contamination on metal substrates by hand-held laser-induced breakdown spectroscopy,” *Applied Optics,* vol. 56, no. 36, pp. 9868-9875, Dec, 2017.
[105] D. A. Hooper, “Development of a Prognostic Method for the Production of Undeclared Enriched Uranium,” Nuclear Engineering, University of Tennessee, University of Tennessee, 2011.
[106] J. J. Henkel, “Development of a Safeguards Monitoring System for Special Nuclear Facilities,” Nucelar Engineering, University of Tennessee, University of Tennessee, 2011.

[107] A. Rimshaw, *Field Service Report - Solstice Ace S/N 2007*, University of Tennessee, Knoxville Tennessee, 2019.
[108] C. A. Smith, M. A. Martinez, D. K. Veirs, and D. A. Cremers, “Pu-239/Pu-240 isotope ratios determined using high resolution emission spectroscopy in a laser-induced plasma,” *Spectrochimica Acta Part B-Atomic Spectroscopy,* vol. 57, no. 5, pp. 929-937, May, 2002.
[109] I. V. Hertel, and C.-P. Schulz, *Atoms, Molecules and Optical Physics 1: Atoms and Spectroscopy*, 2015 ed., Berlin, Heidelberg: Springer Berlin Heidelberg, 2015.
[110] N. ILAGAN, *M-Series Instrument Performance Report,* 0282-0220-1250M, HORIBA Scientific, 2020.
[111] T. O'Haver, "peakfit.m ", 2021.
[112] C. J. Sansonetti, M. L. Salit, and J. Reader, “Wavelengths of spectral lines in mercury pencil lamps,” *Applied Optics,* vol. 35, no. 1, pp. 74-77, Jan, 1996.
[113] C. Energy, *The UF6 Manual: Good Handling Practices for Uranium Hexafluoride, USEC-651*, 10 ed., Bethesda, MD, 2017.
[114] R. Engleman, and B. A. Palmer, “PRECISION ISOTOPE SHIFTS FOR THE HEAVY-ELEMENTS .1. NEUTRAL URANIUM IN THE VISIBLE AND NEAR-INFRARED,” *Journal of the Optical Society of America,* vol. 70, no. 3, pp. 308-317, 1980, 1980.
[115] B. A. Palmer, R. A. Keller, and R. Engleman, Jr., *Atlas of uranium emission intensities in a hollow cathode discharge*, United States, 1980.
[116] R. Payling, and P. Larkins, *Optical Emission Lines of the Elements*, Great Britain: John Wiley & Sons, 2000.
[117] R. L. Kurucz, and B. Bell, "Atomic Spectral Line Database from CD-ROM 23 of R. L. Kurucz," Smithsonian Astrophysical Observatory, 1995.
[118] M. Thomason, "PeakfitTAX.m," B. S. Jordan, ed., 2021.
[119] A. Glaser, “Characteristics of the gas centrifuge for uranium enrichment and their relevance for nuclear weapon proliferation,” *Science and Global Security,* vol. 16, no. 1-2, pp. 1-25, 2008.
[120] A. M. El Sherbini, T. M. El Sherbini, H. Hegazy, G. Cristoforetti, S. Legnaioli, V. Palleschi, L. Pardini, A. Salvetti, and E. Tognoni, “Evaluation of self-absorption coefficients of aluminum emission lines in laser-induced breakdown spectroscopy measurements,” *Spectrochimica Acta Part B-Atomic Spectroscopy,* vol. 60, no. 12, pp. 1573-1579, Dec, 2005.
[121] V. Rai, and S. Thakur, “Physics of plasma in laser-induced breakdown spectroscopy,” *Laser-induced breakdown spectroscopy*, pp. 83-111, 2007.
[122] F. N. Fritsch, and R. E. Carlson, “MONOTONE PIECEWISE CUBIC INTERPOLATION,” *Siam Journal on Numerical Analysis,* vol. 17, no. 2, pp. 238-246, 1980.
[123] G. C. Y. Chan, L. R. Martin, and K. Peruski, "Discussion of Lens Fogging," B. Jordan, ed., Jordan, B., 2021.

[124] B. Efron, “1977 RIETZ LECTURE - BOOTSTRAP METHODS - ANOTHER LOOK AT THE JACKKNIFE,” *Annals of Statistics,* vol. 7, no. 1, pp. 1-26, 1979.
[125] E. Képeš, P. Porízka, and J. Kaiser, “On the application of bootstrapping to laser-induced breakdown spectroscopy data,” *Journal of Analytical Atomic Spectrometry,* vol. 34, no. 12, pp. 2411-2419, 2019.
[126] J. Friedman, T. Hastie, and R. Tibshirani, *The Elements of Statistical Learning Data Mining, Inference, and Prediction*, New York, NY: Springer-Verlag New York, 2009.
[127] P. Buhlmann, “Bootstraps for time series,” *Statistical Science,* vol. 17, no. 1, pp. 52-72, Feb, 2002.
[128] G. Jekabsons, "ARESLab: Adaptive Regression Splines toolbox for Matlab/Octave,," 2016.
[129] J. H. Friedman, “MULTIVARIATE ADAPTIVE REGRESSION SPLINES,” *Annals of Statistics,* vol. 19, no. 1, pp. 1-67, Mar, 1991.
[130] M. Thomason, "Numerical Importance of Individual Wavelengths in HOGSVD," B. Jordan, ed., 2022, p. 1.
[131] M. M. Murnane, H. C. Kapteyn, and R. W. Falcone, “HIGH-DENSITY PLASMAS PRODUCED BY ULTRAFAST LASER-PULSES,” *Physical Review Letters,* vol. 62, no. 2, pp. 155-158, Jan, 1989.

Vita

Ben Jordan is an experienced technical leader with over 20 years of experience with Manufacturing, Engineering, Operations Management, Research and Design, and Entrepreneurship. Mr. Jordan began his career in the tier 1 automotive manufacturing industry in the late 1990's. Mr. Jordan valued his time in automotive manufacturing and learned many manufacturing engineering skills as well as gaining personnel leadership tools.

Mr. Jordan began his nuclear energy career in 2003 with USEC, Inc. upon graduating from the University of Tennessee where he earned a Master of Mechanical Engineering and a Master of Business Administration. During his nuclear career Mr. Jordan has welcomed steadily increasing technical, leadership, and business responsibility. In his first leadership role Mr. Jordan led the manufacturing organization that built and delivered the necessary hardware to allow the first US technology uranium enrichment centrifuge to be operated in over 20 years. Mr. Jordan's next technical leadership opportunity allowed him to serve as authorized design authority for the American Centrifuge machines as the Design Engineering and Analysis Manager for USEC's American Centrifuge Program.

Mr. Jordan's most challenging role has been as the Facility Operations Manager where he was responsible USEC's K-1600 Demonstration Facility. In this role Mr. Jordan was responsible for the demonstration and testing of prototype centrifuge machines. His team consisted of 100 employees ranging from engineers to laborers. The facility and personnel that Mr. Jordan led operated 24/7 under a DOE auditable safety analysis for UF_6 testing operations. The K-1600 Demonstration Facility performed high consequence testing of centrifuge machines and was in itself quite complex including UF_6 process gas feed and withdrawal systems, process gas piping and valving, a range of high vacuum systems, tempered water systems and backups, tiered redundant compressed air and electrical generation systems, mass spectrometry equipment, as well as high speed data acquisition and control systems. Mr. Jordan's leadership and technical background was well-suited for this role. It was in this role where Mr. Jordan first observed the impact of the reliance on mass spectrometry equipment for assay measurement.

Mr. Jordan had obtained knowledge and exposure to the business considerations and relationships affecting Centrus (formerly USEC) and this segued into his current role as the Business Development Manager for Centrus Technical Solutions in Oak Ridge TN. The business development role permitted Mr. Jordan to leverage the industry experience he had gained, with his business and entrepreneurial background to look for new opportunities for Centrus to explore.

In addition, this role provided the opportunity for Mr. Jordan to pursue a nuclear engineering PhD.

Since 2017, with the full support of Centrus and his family, Mr. Jordan has been researching faster and less costly means of measuring the assay of UF_6. He currently lives in Powell Tennessee with his wife Jen and their two children. In his free time, Mr. Jordan is active in his children's hobbies and scouting activities, as well as a private pilot, realtor, landlord, inventor, and farmer.